N75-78190

~~CONFIDENTIAL~~

C71 1113 A

N75 78190

UB

NASA CR-1904

NASA CONTRACTOR REPORT

UB NASA CR-1904

CLASSIFICATION CHANGE
To UNCLASSIFIED
By authority of NASA TD TN-466
Changed by D. L. Weckhase Date 2/26/75
Classified Document Master Control Station, NASA
Scientific and Technical Information Facility

~~NOFORN~~

DOWNGRADED TO Unclassified
BY AUTHORITY OF NASA CLASSIFICATION
CHANGE NOTICES NO. 234 DATED 29 Feb 82
ITEM NO. 45

DIRECT-CONNECT TESTS OF A HYDROGEN-FUELED SUPERSONIC COMBUSTOR

by F. S. Billig, R. C. Orth, and J. A. Funk

Prepared by
APPLIED PHYSICS LABORATORY
THE JOHNS HOPKINS UNIVERSITY
Silver Spring, Md. 20910
for Langley Research Center

~~CLASSIFIED BY IT DD 254 (10) NASW-2431~~
~~SUBJECT TO GENERAL DECLASSIFICATION~~
~~SCHEDULE OF EXECUTIVE ORDER 11652.~~
~~AUTOMATICALLY DOWNGRADED AT~~
~~TWO-YEAR INTERVALS.~~
~~DECLASSIFIED ON DECEMBER 31 1977~~

NATIONAL AERONAUTICS AND SPACE ADMINISTRATION • WASHINGTON, D. C. • AUGUST 1971

~~CONFIDENTIAL~~

94

~~CONFIDENTIAL~~ C71 1113

1. Report No.
NASA CR-1904

2. Government Accession No.

3. Recipient's Catalog No.

4. Title and Subtitle
DIRECT-CONNECT TESTS OF A HYDROGEN-FUELED SUPERSONIC COMBUSTOR (U)

5. Report Date
August 1971

6. Performing Organization Code

7. Author(s)
F. S. Billig, R. C. Orth, and J. A. Funk

8. Performing Organization Report No.

9. Performing Organization Name and Address
Applied Physics Laboratory
The Johns Hopkins University
8621 Georgia Avenue
Silver Spring, Maryland 20910

10. Work Unit No.

11. Contract or Grant No.
NOw 62-0604-C

12. Sponsoring Agency Name and Address
National Aeronautics and Space Administration
Washington, D.C. 20546

13. Type of Report and Period Covered
Contractor Report

14. Sponsoring Agency Code

15. Supplementary Notes

16. Abstract

(U) Results from direct-connect tests of hydrogen-fueled supersonic combustors are presented. The tests were made using arc-heated air at combustor inlet Mach numbers of 2.8-3.2. A variety of axisymmetric combustor geometries were investigated with fuel injection from either a number of discrete holes oriented normal to the air stream or from a circumferential slot oriented partially downstream. The effects of inlet temperature of the fuel and air, combustor wall temperature, combustor length, combustor area ratio and combustor shape were studied. Performance comparisons and test evaluations are based on calorimetrically determined combustion efficiencies, pressure, temperature and heat flux measurements along the combustor walls and instream measurements of pressure and gas composition in the combustor exit plane. A theoretical model of the supersonic combustion process which includes a pre-combustion shock-compression is used to explain the character of the observed pressure distributions and to assess the effects of the measured heat transfer rates, deduced wall shear and combustor geometry on performance.

17. Key Words (Suggested by Author(s))
Supersonic Combustion
Ramjets
Hydrogen
Testing

18. Distribution Statement
~~Confidential~~ Available to U.S. Government Agencies and Their Contractors Only

19. Security Classif. (of this report)
~~Confidential - Group 4~~

20. Security Classif. (of this page)
Unclassified

21. No. of Pages
91

22. Price

~~GROUP 4 Downgraded at 3 year intervals; declassified after 12 years.~~

~~This material contains information affecting the national defense of the United States within the meaning of the espionage laws, Title 18, U.S.C., Secs. 793 and 794, the transmission or revelation of which in any manner to an unauthorized person is prohibited by law.~~

~~CONFIDENTIAL~~

DIRECT-CONNECT TESTS OF A HYDROGEN-FUELED SUPERSONIC COMBUSTOR (U)

By F. S. Billig R. C. Orth and J. A. Funk

Applied Physics Laboratory, The Johns Hopkins University
Silver Spring, Maryland

SUMMARY

(C) Direct-connect tests of hydrogen-fueled supersonic combustors were made using arc-heated air at combustor inlet Mach numbers of 2.8-3.2. With stagnation temperatures of 1730 to 3050°K (3115 to 5490°R) and stagnation pressures near 3.1 MN/m^2 (450 psia), the tests simulated flight Mach numbers of 6.2 to 8.3 at altitudes of 18 to 37 Km (60,000 to 120,000 ft). A variety of combustor geometries made up of cylindrical sections, 2.4×10^{-2} rad (1.4°)-half-angle cone frustums, and in some cases with a rearward-facing step (sudden expansion) immediately behind the injector station, were tested. Flush-wall fuel injectors were of two types: a ring of equally spaced holes normal (1.57 rad (90°)) to the air flow, and a continuous slot at a 0.835 rad (45°) downstream angle.

(C) Results in a 0.51 m (20-in)-long conical combustor showed that combustion efficiency (η_c) is consistently higher with the discrete-hole injectors than with the continuous slot injector. To achieve a given combustion efficiency goal via autoignition, the slot injector would require much higher flight Mach numbers (i.e., combustor inlet temperatures); conversely, the hole-type injector would permit lower take-over Mach numbers for a scramjet-typically Mach 4 versus Mach 8.

(C) Gas samples from the combustor exit plane showed that fuel distribution is the principal factor causing poor efficiency with a slot injector - the mixture is too rich near that wall, and far too lean near the combustor centerline. Increasing the combustor wall temperature by coating the inside surface of the water-cooled wall with zirconia increased η_c by 3% to 8% for the slot injector, however.

(C) In a scramjet it is important to isolate the air inlet from combustor-induced pressure disturbances. Tests showed that either a constant-area section ahead of the injector or a step immediately downstream of it would provide the isolation. The step causes some loss in η_c (e.g., 2% at a fuel-air equivalence ratio ER of 0.5, or 6% at ER = 0.8) when compared to a step-free configuration of similar length (0.737 vs 0.686 m (29 vs 27 in.)) respectively. Combustor length has a direct effect on η_c; increasing the length from 0.686 m to 0.889 m (27 in. to 35 in.) in the step-free designs resulted in an increase in η_c of 2%-4%, whereas when the length of the step combustor was reduced from 0.737 m to 0.381 m (29 in. to 15 in.) η_c dropped from 89% at ER = 0.5 and 74% at ER = 0.8 to near 70% at all ER's tested.

(U) In conjunction with the combustor tests a theoretical model for heat addition in supersonic flow was developed. On the basis of comparisons of predicted pressure distributions and experimental results from these tests and others in the cited literature it has been concluded that the pseudo-one-dimensional model consisting of pre-combustion shock followed by an exponentially decaying pressure yields an excellent descriptive approximation of the complex process. The theory is unique in this general field of study in that it yields an a priori definition of the strength of the pre-combustion shock and the downstream pressure field and all other properties at any station in the flow. Moreover, with the theory it is possible to test the sensitivity of measured properties, e.g., the combustion wall-pressure distribution, to changes in η_c to establish whether a particular measurement is inherently capable of resolving η_c. From these results it has been concluded that calorimetry is the best if not the only practical means of obtaining an accurate measure of the overall η_c.

NOMENCLATURE

A	area m^2
C_D	discharge coefficient
$\bar{C}_f$	skin friction coefficient $\equiv 2\, \bar{\tau}_w / \rho_{ci} u_{ci}^2$
d	fuel injection port diameter (Fig. 2), m
E	arc voltage, V
ER	equivalence ratio = f/f_s
ER_{eff}	effective equivalence ratio = $\eta_c ER$
f	fuel-air weight ratio
f_s	stoichiometric fuel-air ratio based on standard air composition given in Eq. (1)
g	gravity acceleration constant 9.804 m/s^2 (32.164 ft/sec^2)
h	specific enthalpy J/kg
Δh	defined in Eq. (14)
ΣH_p	defined in Eq. (9)
ΔH_f	lower heating value of hydrogen = 119.8MJ/kg (51,570 Btu/lb)
I	arc current, A
M	Mach number
p	pressure N/m^2
P	partial pressure N/m^2
q	heat transfer per unit area J/m^2s; moles of H_2 burned, Eq. (4a)
Q	bulk heat transfer rate J/s

ΣQ_w	defined in Eq. (9)
r	moles of H_2 fuel; recovery factor, Eq. (18)
s	fuel injection slot width (Fig. 2), m
T	temperature, ^oK
u	velocity m/s
x	moles of NO, Eq. (1a)
w	moles of monatomic oxygen, Eq. (1a)
$\dot{w}$	weight flow rate kg/s
z	moles of NO_2 that form N_2O_4 in gas sampling bottle, Eq. (1c)
α	conical combustor half-angle (Fig. 11) rad
β	fuel injection angle (Figs. 2, 11) rad
γ	ratio of specific heats
ϵ	Crocco pressure-area exponent
η_c	combustion efficiency
ξ	defined by Eq. (2)
ρ	density kg/m^3
τ	shear stress N/m^2

Subscripts:

a	air, conditions ahead of fuel injector (Fig. 11)
b	downstream section of control volume (Fig. 11)
b'	end of separation zone (Fig. 11)
ce	combustor exit
ci	combustor inlet
d	calorimeter quench water
f	fuel
0	free stream flight conditions
r	recovery condition
s	conditions downstream of combustor shock (Fig. 11)
t	total conditions
w	combustor wall

Superscripts:

-	average
/	conditions following a normal shock
*	conditions at sonic point

DIRECT-CONNECT TESTS OF A HYDROGEN-FUELED SUPERSONIC COMBUSTOR (U)

F. S. Billig, R. C. Orth, J. A. Funk

INTRODUCTION

(U) During the past seven years a research program has been under way at the Applied Physics Laboratory to determine the expected performance of the combustor and nozzle for hypersonic ramjets with supersonic combustion of hydrogen in the flight Mach number range from 5 to at least 10. The injection and combustion characteristics of gaseous hydrogen have been investigated in direct-connect testing apparatus using various injector and combustor geometries. Experimental results and data analysis techniques from the early tests at a combustor inlet Mach number M_{ci} of 2.8, using arc-heated air, were described in Ref. 1. Studies of the ignition of hydrogen in the presence of a platinum catalyst in a Mach 1.62 free-jet and in an M_{ci} = 1.98, direct-connect combustor are reported in Ref. 2. This report presents the results from the more recent tests at M_{ci} = 2.8-3.2 and describes the continually improving instrumentation and data analysis techniques. Some of the same apparatus has been used to study the combustion characteristics of reactive liquid fuels in programs sponsored by the Ordnance Systems Command of the United States Navy and for the United States Air Force Aero Propulsion Laboratory (Refs. 3-4). Similar work in direct-connect testing of supersonic combustors has been done at other laboratories (Refs. 5-11) but in distinct contrast to the test described herein, combustion efficiencies were not obtained directly.

(U) Tables and figures which summarize the results from all of the tests together with particular basic data plots pertinent to the discussion are included in the main body of the text. The remaining basic data plots, viz. longitudinal wall static pressure distributions and radial distributions of pitot pressure and gas composition in the combustor exit plane are included in the Appendix without further discussion.

EXPERIMENTAL APPARATUS

(U) The experimental apparatus used in these tests is schematically illustrated in Fig. 1. Metered cold air, heated in a direct-current arc to approximately 2780-3060°K (5000-5500°R) is discharged into a mixing chamber. Cold secondary air is added to obtain the desired total temperature, which varied from 1470 to 3030°K (2650 to 5460°R) in these tests. The total pressure is typically 2.75-3.31 MN/m^2 (400-480 psia), and the air weight flow is approximately 1.45 kg/s (3.2 lb/sec). Total pressure in the mixing chamber was measured directly and total temperature was deduced from the metered airflow rates, the measured total pressure and the effective cross-sectional area of the throat of the supersonic nozzle using a suitable continuity relationship (Ref. 12). The effective area of the nozzle was obtained from calibrations with unheated air ($C_D \approx 0.95$) and the continuity relationship

($T_t = f\ (\dot{w}_a/p_tC_DA^*)$) was obtained from calculations of isentropic-pseudo-equilibrium expansions. Pseudo-equilibrium as used herein is defined as a flow in which the concentration of NO is held constant and all other species are present in their equilibrium concentration. The method by which the level of NO present is determined for a given testing condition is discussed below. Initially, tests were made using a 0.15 rad (8.5°)-half-angle conical nozzle having a nominal exit Mach number of 2.9. More recently a Mach 3.2 contoured nozzle has been used. Typical static conditions at the combustor inlet are $p_{ci} = 0.5$ to 1.0×10^5 N/m^2 (0.5-1 atm), T_{ci} = 660-1330°K (1200-2400°R).

(U) The combustor comprises an assembly of cylindrical and/or diverging conical sections which can be interchanged to obtain the desired injector arrangement and combustor geometry. Gaseous hydrogen is supplied to the injector from storage tanks, metered with sonic orifices and heated to 290 to 1030°K (520°R to 1860°R) in a 9.8 m (32-ft)-long Nickel 200 tube. The 1.27×10^{-2}m (0.5-in.)-i.d., 0.95×10^{-2}m (0.375-in.)-thick tube is resistance-heated to 1370°K (2460°R) and is designed to provide up to 0.032 kg/m^2 (0.07 lb/sec) of hydrogen at 6.9MN/m^2 (1000 psia), 1280°K (2300°R) for a duration of 20 secs. For most of the tests the duration is between 30 and 45 sec, covering 1 to 3 ER settings and a "cold point" (heated air but no fuel flow). Approximately 12 seconds are allotted for each fuel setting in order to obtain steady-state conditions in the exhaust calorimeter. An electronic sequencer is pre-programmed to establish required testing conditions, set the fuel flow rates, adjust the water flow rates to the calorimeter and regulate the gas sampling system.

(U) The various combustor sections contain numerous surface static pressure taps and thermocouples. All sections are water-cooled, and flow rates and temperature rises are metered to obtain bulk heat transfer rates. Some sections also contain 3.18×10^{-2}m (0.125-in.)-diam. disk type local wall surface calorimeters. Radial distributions of properties in the combustor exit plane are determined from pitot and cone-static pressures and gas samples obtained with multi-point rakes. Analysis of the gas samples provides a measure of the local fuel/air ratio and local combustion efficiency by the method described in the next section. Immediately downstream of the combustor exit, metered water is sprayed into the stream to quench the reaction rapidly. The bulk heat release and overall combustion efficiency are obtained by making a calorimetric balance on the exhaust gases using temperature measurements from a twelve-point thermocouple rake in the exit of the calorimeter together with all of the wall coolant rates. Water flow to the calorimeter was controlled to yield exit temperatures between 550 and 830°K (1000° and 1500°R) and to keep the wall temperatures to 440-550°K (800°-1000°R) to guarantee that the reactions were effectively quenched. The absolute accuracy of the calorimetric method of deducing η_c is checked for each run during the period of established air flow conditions but without fuel flow (cold point). The enthalpy of the air stream at the combustor exit deduced from the calorimeter is compared with the enthalpy of the air at the combustor inlet deduced from continuity and the measured heat losses to the combustor walls. This agreement is generally within $\pm$ 5%. With burning, the combustion efficiency determination is based on the difference in total heat release between the burning point and the cold point. Thus, it is possible that by removing that portion of the error associated with the "cold point" reading the accuracy of the η_c determination is within $\pm$ 5%. This appears to be the case when data repeatability and consistancy are examined, i.e. η_c determinations for different runs in which conditions are closely matched, agree to within $\pm$ 1-2%.

(U) Figure 2 shows sectional views of the fuel injector rings. The discrete circular hole injectors are depicted in views a and b and have total injection areas of 4.3×10^{-5} and $4.1 \times 10^{-5} m^2$ (0.067 and 0.064 in.^{2}), respectively (cross sectional area normal to hydrogen flow axis). The circumferential slot injectors c and d have nominal injection areas of 5.0×10^{-5} and $19.4 \times 10^{-5} m^2$ (0.066 and 0.30 in.^{2}) respectively. With these injectors difficulty was experienced in maintaining dimensional stability of the slot width when the fuel was heated. Thus, to deduce the slot area for any given test it is necessary to solve the continuity equation using the metered fuel weight flow, the measured total temperature and pressure and a discharge coefficient of 0.70. Pressure taps and midstream thermocouples are located in each injector.

(U) Figure 3 shows schematic illustrations of the various combustor configurations. The model stations in meters are referenced to the centerline of the injector with positive values for downstream locations. Positions of the aforementioned disk calorimeters and the ring calorimeters are indicated. The ring calorimeters are short cylindrical sections used to obtain circumferentially averaged heat fluxes in local regions of the flow. The overall combustor exit/combustor inlet cross-sectional area ratios are: 2.64 for configuration A; 2.59 for configuration B; 2.00 for configurations C, E, F, and G; and 1.93 for configuration D and 1.43 for configurations H and I. The total surface areas of the combustors downstream of the injector station are: 0.133 m^2 (206 in.^{2}) for A; 0.263 m^2 (408 in.^{2}) for B; 0.163 m^2 (252 in.^{2}) for C; 0.158 m^2 (245 in.^{2}) for D; 0.222 m^2 (344 in.^{2}) for E; 0.175 m^2 (272 in.^{2}) for F; 0.200 m^2 (310 in.^{2}) for G and 0.097 m^2 (151 in.^{2}) for H and I.

AIR COMPOSITION AND ANALYSIS OF GAS SAMPLES

(U) The gas samples that are withdrawn from the 7 probes located in the combustor exit plane into stainless steel bottles are analyzed by gas chromatography. To reduce the data, certain assumptions for the formulation of the species present in the bottle must be made. To develop these arguments it is necessary to define the composition of the gas entering the combustor. Referring to Figure 1, the air that passes through the nozzle isolating the arc chamber from the mixing chamber is a mixture of gases, some of which have passed through the arc column and some of which have not. The gases which have passed through the arc column are highly ionized, but they are partially cooled by the cooler air that did not pass through the arc column. The result is a mixture that, by the time it reaches the entrance of the isolation nozzle, probably contains only a small fraction of excited species but a significant amount (x moles) of NO and a lesser amount (w moles) of O. In passing through the supersonic nozzle to the test section, the small amount of O combines with some of the NO forming w moles of NO_2. In the absence of combustion, the remaining NO (x - w moles) would pass through the combustor relatively unaffected because the residence time in the combustor would be too short for the $NO + \frac{1}{2} O_2 \rightarrow NO_2$ reaction to take place. However, during the long stay time in the gas sample storage bottles the NO would probably react with excess O_2 forming NO_2 and N_2O_4 in equilibrium proportions.

(U) This chemistry can be presented by the following molar equations:

$$20.950\ O_2 + 78.088\ N_2 + 0.962\ A \rightarrow$$

(standard air)

$$\xi + w\ O + x\ NO + \left(20.950 - \frac{x}{2} - \frac{w}{2}\right) O_2 \rightarrow \tag{1a}$$

(gas entering isolation nozzle for $T < 3720^{\circ}K$ ($6700^{\circ}R$))

$$\xi + (x - w)\ NO + w\ NO_2 + \left(20.950 - \frac{x}{2} - \frac{w}{2}\right) O_2 \rightarrow \tag{1b}$$

(gas at test section)

$$\xi + (20.950 - x)\ O_2 + (x - z)\ NO_2 + \frac{z}{2}\ (N_2O_4) \tag{1c}$$

(gas in sample bottle)

where

$$\xi \equiv \left(78.088 - \frac{x}{2}\right) N_2 + 0.962\ A \tag{2}$$

(U) It will be shown later that determination of x is sufficient (without having to define w) to define the combustion efficiency η_c, and equivalence ratio ER. Thus, either from a calibration run without combustion or from samples drawn during the "cold point" of the test, x can be obtained simply from the ratio of the partial pressures of N_2 and O_2, viz:

$$P_{O_2}/P_{N_2} = (20.950 - x)/(78.088 - 0.5\ x) \tag{3}$$

Figure 4 shows the radial variation of x, which is equivalent to the O_2 deficiency in the sample bottle (1c), for runs made at various air total enthalpy (h_{t_a}) levels at the mixing chamber exit. (This enthalpy is the reference point used to define conditions in the supersonic combustion experiments.) The mean values (area-weighted mean mole %) of x from these curves are cross-plotted against h_{t_a} in Fig. 5. If the chemistry represented by Eqs. 1a-1c is correct, these values of x are numerically equal to the mole percentages of NO in Eq. (1a), after arc-heating but before the $NO + O \rightarrow NO_2$ reaction takes place. It is seen that these points do group well around the theoretical curve for chemical equilibrium entering the isolation nozzle. Figure 5 also shows curves corresponding to chemical equilibrium at the mixing chamber entrance, the mixing chamber exit, and the throat of the supersonic nozzle. The curve for the mixing chamber exit was obtained from the equilibrium composition of air at an enthalpy level 0.465MJ/kg (200 Btu/lb) higher than the mixing chamber exit. Similarly, the isolation nozzle entrance conditions are for an enthalpy level 0.74 MJ/kg (320 Btu/lb) higher than the mixing chamber exit. The enthalpy changes are equal to the measured heat loss to the walls in the respective sections. The lowest curve is based on the static conditions in the throat including wall heat losses in this section, thus the lower enthalpy and NO concentration. The close correspondence of the data points with the curve for equilibrium conditions at the entrance to the isolation nozzle suggests that this condition would be reasonable to use for making calculations of η_c and ER whenever measurements without combustion are not available. Moreover, since the NO concentration is closely matched, it is reasonable to assume that the value of w could be found from the corresponding value for the O concentration at the same equilibrium conditions. Although w is not needed in the subsequent evaluation of η_c and ER, it would be required for more rigorous kinetic calculations used to describe the combustion process.

(U) With combustion, assuming that r moles of hydrogen are added in the combustor, the composition of the combustion products withdrawn from the stream into sampling bottles can be represented by one of the following three plausible formulations [using Eq. (2)]:

$$\xi + \left(20.95 - \frac{x}{2} - \frac{w}{2}\right) O_2 + (x-w)\ NO + w\ NO_2 + r\ H_2$$

$$\rightarrow \xi + x\ HNO_3 + \left(q - \frac{x}{2}\right) H_2O + \left(20.95 - \frac{5}{4}x - \frac{q}{2}\right) O_2 + (r-q)\ H_2 \qquad (4a)$$

or (4b)

$$\rightarrow \xi + (20.95 - x - q)\ O_2 + (x - z - 2q)\ NO_2 + \frac{z}{2} N_2O_4 + 2q\ HNO_3 + (r-q)\ H_2$$

or

$$\rightarrow \xi + (x-z)\ NO_2 + \frac{z}{2}\ N_2O_4 + q\ H_2 + \left(20.95 - x - \frac{q}{2}\right) O_2 + (r-q)\ H_2. \qquad (4c)$$

(U) The more likely formulations, (4a) and (4b), are based on the hydrolysis of NO and NO_2 to HNO_3 via the intermediate species HNO_2. Formulation (4b) is for low ER, where the water formed in the combustion process is insufficient to hydrolyze the NO and NO_2 completely; (4c) assumes complete oxidation of NO to $NO_2 \rightleftarrows N_2O_4$, with no reaction with the hydrogen-containing species. In all cases

$$\eta_c = q/r, \qquad (5)$$

and

$$ER = [2.016/28.995\ (0.02917)]\ r/100 = 0.0238\ r, \qquad (6)$$

where r and q are obtained from the partial pressures of the samples with combustion; i.e., (3a-3c) yield, respectively,

$$P_{O_2}/P_{N_2} = \left(20.950 - \frac{5}{4} - \frac{q}{2}\right) / \left(78.088 - \frac{x}{2}\right) \qquad (7a)$$

$$P_{O_2}/P_{N_2} = (20.950 - x - q) / \left(78.088 - \frac{x}{2}\right) \qquad (7b)$$

$$P_{O_2}/P_{N_2} = \left(20.950 - x - \frac{q}{2}\right. / \left(78.088 - \frac{x}{2}\right) \qquad (7c)$$

and, for all formulations,

$$P_{H_2}/P_{N_2} = (r - q) / \left(78.088 - \frac{x}{2}\right) \qquad (8)$$

With respect to the kinetic effects it is impossible to discriminate between reactions that take place in the combustor and those that take place in the deceleration and quenching of the sample. To minimize the probe effects the probes are designed with sharp lips and a 12 to 1 internal area expansion. In this way, there is no stand-off shock (Ref. 13*) and the flow is aerodynamically expanded prior to the wall cooling to effect a rapid quench. Local combustion efficiencies, defined above as the ratio of reacted/injected hydrogen, include both kinetic effects and mixing inefficiency. Presumably, during the relatively long period that gas is flowing into the sampling bottle, alternate slugs of reaction products and unreacted fuel are entering the probe due to the turbulence in the flow.

(U) It should also be noted that with oxides of nitrogen present in the combustion products the definition of η_c precluded the possibility of $\eta_c = 1.00$ above an ER of approximately 0.8 or 0.9. For example, for $h_{t_a} = 2.56$ MJ/kg (1100 Btu/lb) from Fig. 5, the oxygen concentration is 0.2095 - 0.032 = 0.1775, so the maximum ER at which η_c could be unity is 0.1775/0.2095 = 0.847.

(U) The samples are passed through a desiccant prior to entry into the chromatograph to remove H_2O and the aqueous solution of HNO_3. In the chromatograph special procedures were taken to balance the flows precisely to obtain the desired accuracies of $\pm$ 1.0% (Ref.14). The signal from the thermal conductivity cells is integrated electrically to obtain the "peak area" to obtain the partial pressure of each species. Summing of partial pressures and comparison with the measured total pressure provides a check on the accuracy.

EXPERIMENTAL RESULTS

(U) Table I summarizes the testing conditions, combustor and injector configurations and the calorimetrically determined combustion efficiencies for all of the tests. These bulk combustion efficiencies are based on the use of

---

*The Republic Aviation Corp. built and tested a probe patterned after the APL design (Ref. 3). Schlieren photographs showed that the flow was attached, with no stand-off shock.

the following equation:

$$\eta_c = \frac{\Sigma Q_w + \Sigma H_p - \dot{w}_a h_{t_a} - \dot{w}_f h_{t_f} - \dot{w}_d h_{t_d}}{\dot{w}_f \Delta H_f} \qquad (9)$$

ΣQ_w is the total heat transfer rate to all of the walls of the apparatus beginning with the injector and ending with the calorimeter exit

$\dot{w}_a h_{t_a}$, $\dot{w}_f h_{t_f}$ and $\dot{w}_d h_{t_d}$ are the total enthalpies of the incoming air, hydrogen and quench water, respectively

ΔH_f is the lower heating value of hydrogen = 119.8MJ/kg (51,570 Btu/lb)

ΣH_p is that fraction of the sensible heat contained in the gas passing through the calorimeter if it would be cooled from the calorimeter exit temperature to a reference temperature of 0^oK but not including the latent heats (enthalpies throughout the report are based on 0^oK reference temperature, e.g., for air at $1 \times 10^5 N/M^2$ (1 atm) and 278^oK (500^oR) h = 0.278MJ/kg (119.6 Btu/lb)). The gas is assumed to consist of products of combustion of the hydrogen-"air" reaction at $ER_{eff} = ER \cdot \eta_c$, plus unreacted fuel in the amount $(1-\eta_c)$ ER, plus the quench water (steam) added in the calorimeter. The "air" composition is given by Eq. (1b) and thus contains w moles of NO_2 and x-w moles of NO. The value of x is obtained from the top curve of Fig. 5 for a total enthalpy corresponding to h_{t_a} for the test conditions. The value of w is obtained from the equilibrium composition of air having a mole fraction of NO equal to x and a total pressure matching p_{t_a} the test conditions; thus, a higher enthalpy (i.e., $\sim$ the enthalpy at the isolation nozzle entrance). These amounts of NO and NO_2 are treated as inert species in the chemical "equilibrium" calculations made to determine the composition of the hydrogen-"air" products. In this calculation the method of Ref. 15 is used to compute the "equilibrium" composition at conditions corresponding to the calorimeter exit temperature and pressure. Since this temperature is controlled to $600\text{-}900^oK$ by adjusting the quench water, and the pressure is $\sim .05 MN/m^2$ the concentration of radicals is inconsequential. Note that the solution is iterative in that Equation (9) is implicit in η_c, and it appears that the determination of η_c is indeed rigorous. However, in practice it has been found that neglecting the presence of the presumed "frozen" species NO and NO_2 and the unburned hydrogen has a very small effect on the resulting η_c. Therefore, in most cases the simpler calculation is performed and a small correction (0-2%) based on a few of the more rigorous calculations is made, if required.

(U) Tests 78 through 88 were made with the conical nozzle and were intended to show the effect of air and fuel stagnation temperatures on η_c for both discrete-hole and wall-slot injectors. Static pressure traces for these runs are difficult to interpret in the region of the injector due to compression caused by the change in flow direction and from the 0.15 rad (8.5^o)-half-angle nozzle to the 0.026 rad (1.5°)-half-angle combustor. All subsequent runs were made with a contoured nozzle designed to operate at M_{ci} = 3.2 and T_t = 2500°K (4500°R). Runs 89-110 were made to determine the effects of combustor wall temperature on η_c for various fuel temperatures and different combustor lengths with slot and discrete-hole injection. Pressure distributions along the combustor wall and across the combustor exit plane for these runs verified the existence of the oblique-shock, exponentially decreasing pressure process postulated in Ref. 16. In runs 112-127 the combustor geometry, particularly in the region of the injector, was varied to investigate means of isolating the pre-combustion shock from the inlet air nozzle and effects on combustor wall heat transfer. The accuracy of the gas-sampling measurements reached an acceptable point by Run 83, and the ring and disk calorimeters were first used in Run 112.

(C) Combustion efficiencies for Runs 78-88 are presented in Fig. 6. The solid symbols and curves are for the 2.3 x 10^{-4}m (9-mil)-slot injector, and the open symbols and dashed curves are for the discrete-hole injector. The curves are drawn through points having about the same air static temperature. Fuel static temperatures vary from 628°K to 701°K (1130°R to 1262°R) except for Run 82. Considering the close grouping of data from Runs 82 and 83, fuel temperature in this range for these geometries is apparently a second-order effect. The first-order effects are injector, geometry, ER, and air temperature. Combustion efficiency is markedly higher for hole injection and increases with increasing T_{ci} and decreasing ER for both injectors. In Fig. 7 the same data have been replotted vs T_{ci} with bounds on ER for each injector. If it is assumed that the η_c values are only weakly dependent on M_{ci}, then these results can be correlated to various flight conditions. For this comparison, the simulated flight condition is based on the tested air temperature T_{ci}, assuming that in a flight engine the combustor inlet Mach number is equal to $M_0/3$. Thus, true simulation only occurs for T_{ci} = 1330°K (2400°R) and M_0 = 8.7 (M_{ci} = 2.9). With this hypothesis, the non-linear M_0 scale can be constructed as shown. Based on a minimum acceptable η_c of 70%, the operating limits for the slot injector are M_0 = 6.3, T_{ci} = 1060°K (1900°R) at ER = 0.2 and M_0 = 8.1, T_{ci} = 1280°K (2300°R) at ER = 0.8. With hole injection they are M_0 = 3.5, T_{ci} = 560°K (1000°R) at ER = 0.4 and M_0 = 4.7, T_{ci} = 860°K(1550°R) at ER = 1.0. Thus, for combustors relying on autoignition, discrete-hole injection could be used at considerably lower flight Mach numbers.

(C) Typical results of the gas sampling-measurements from the runs with discrete-hole injection are shown in Fig. 8. In this figure the NO concentration is based on the average value obtained from Figure 5 for the air total enthalpy of 2.41MJ/kg (1035 Btu/lb).because samples from the corresponding "cold point", Run 83-3 were not available. In some of the other specie distribution plots included in the Appendix the local NO concentration deduced from the "cold point" measurement is used. These cases can be readily distinguished since the mole fraction of NO varies with radius as contrasted to the constant value shown in Fig. 8. The deduced radial distribution of ER shows a maximum at about 0.0406m (1.6 inches) from the wall and very little hydrogen on the centerline. The shape of the ER curve is similar to that observed in experiments on flat plates with no combustion (Ref. 17). Although it is necessary to multiply ER by the radial variation of mass flux to obtain the precise distribution of fuel and in turn the total hydrogen mass, the area-averaged value of ER is in close agreement with the overall metered ER. Available data for the other runs in this series of tests are included in the Appendix, together with the pressure distributions. The latter are not compared with results of the shock-combustion theoretical model (Ref. 16) because of the ambiguity that arises with the wall turning of the conical flow at the combustor entrance.

(C) Runs 96-110 were made with a 0.61m (24-in.)-long conical combustor to determine the effect on combustion efficiency of: (a) combustor wall temperature (b) fuel temperature, and (c) fuel injector design. Since gas-side heat transfer coefficients to the combustor wall are high, and the wall temperature on the water-cooled side cannot exceed the boiling point of water by more than a few degrees, the hot wall temperature T_w is governed primarily by the gas-side transfer coefficient and the wall conductance. Adjustment of the coolant flow has very little effect on T_w. In order to produce a change in T_w, 7.62×10^{-4}m (0.030 inch) of zirconium oxide and 7.62×10^{-5}m (0.003 inch) of Nichrome bonding were added to the 1.6×10^{-3}m (0.063-inch)-thick stainless steel wall. Wall temperature increases of $> 700^{\circ}$K could be obtained at the highest gas-side heating rate. The gas-side heat-transfer rate increases with increasing ER_{eff}, is higher for discrete-hole injection than for slot injection, and increases with increasing T_f. Thus, T_w varies significantly as indicated in Fig. 9 which summarizes the η_c data for these tests. The curves are labeled "hot" for the coated combustor and "cold" for the bare metal design. The uncoated combustor was not run with hole injection. The air total temperature was intended to be constant, but small changes in arc operation resulted in a range of conditions from 2130°K (3840°R) (h_{t_a} = 2.46MJ/kg (1059 Btu/lb)) to 2360°K (4250°R)(h_{t_a} = 2.76MJ/kg (1188 Btu/lb)). This corresponds to a $\pm$ 53°K (95°R) variation in T_{ci} about the average value of 860°K (1540°R) (h_{t_a} = 2.61MJ/kg (1123 Btu/lb)). The η_c values for the data shown in Fig. 9 could be affected by this variation, but having only a limited number of test points to establish the required adjustment, none was made.

(C) Figure 9 shows that with circumferential slot injection η_c increases from 3% to 8% for the hotter combustor walls. Wall temperature effects with hole injection would probably be smaller, since the important transport processes are taking place in a region farther from the wall. Combustion efficiencies for the discrete-hole injector are consistently higher than with the slot injector and are less sensitive to changes in T_f. Increasing fuel temperature produces significantly higher η_c with slot injection. In other studies (Ref. 18) it has been shown that in the absence of combustion, increasing fuel temperature enhances the mixing of parallel air and fuel streams;

these tests suggest that the same result occurs when combustion is present. With hole injection the effect of fuel temperature is small. There appears to be a slight rise of 2% in η_c for 440 to 500°K (800-900°R) rise in T_f, but the differences noted are of the same order as the absolute accuracy of the η_c measurements.

(C) The ER distributions shown in Fig. 10c deduced from the species mole fractions shown in Figs. 10a and b for Runs 106-23 and 108-33 indicate that fuel distribution is the principal factor giving rise to the higher η_c with hole injection. With slot injection a large region of flow near the wall has local ER > 1, whereas with hole injection no regions of ER > 1 are present. In both cases the concentration of hydrogen near the combustor centerline is low, indicating that for conical combustors with dimensions of the order tested, some type of instream injection is needed if flatter profiles are desired.

THEORETICAL ANALYSIS AND HEAT TRANSFER INPUTS

(U) During the time that these runs were being made a theoretical analysis of the processes that take place in a supersonic combustor was being developed. In the analysis the combustion process is depicted as one of three types depicted in Fig. 11, depending on the relative amount of heat addition. Case (a) is a shock-free, continuous, one-dimensional, heat addition process. The control boundary consists of the inlet and exit surfaces (at stations a and b) and the combustor wall. Fuel is injected at an incidence angle β just downstream of station a. The forces on the control boundary are due to the combined effects of pressure and shear, and heat can be transferred across the boundaries adjacent to the wall. In case (b) the combustion is preceded by a normal shock which lies within the control boundary. As in case (a), the location of station b is arbitrary, with no violation of the one-dimensional restrictions. In case (c) the combustion is preceded by an oblique compression wave, and a separated zone is required to complete the flow picture. In this case the one-dimensional analysis can not be valid unless station b is located downstream of the reattachment point b'. Discontinuities in the combustor area (e.g., a step change in area at station a) are permitted upstream of station b'. The integral forms of the appropriate conservation equations are:

Mass

$$g\ \rho_a u_a A_a + \dot{w}_f = g\ \rho_b u_b A_b \tag{10}$$

Momentum (Axial)

$$p_a A_a + \int_a^b p_w \sin\alpha\ dA_w - p_b A_b - \int_a^b \tau_w \cos\alpha\ dA_w =$$

$$\rho_b u_b^2 A_b - \rho_a u_a^2 A_a - \rho_f u_f^2 A_f \cos\beta = 0 \tag{11}$$

Energy

$$h_a + \frac{u_a^2}{2} + f\left(h_f + \frac{u_f^2}{2}\right) = (1 + f)\left(h_b + \frac{u_b^2}{2}\right) + \frac{1}{\dot{w}_a}\int_a^b q_w \, dA_w \qquad (12)$$

(U) To obtain solutions to these equations it is necessary to have both an appropriate equation of state, viz.,

$$p_b = p_b(\rho_b, h_b) \qquad (13)$$

and expressions for the wall distributions of pressure, shear and heat transfer. For a state relationship, pseudo-equilibrium between unreacted fuel and products of combustion in thermodynamic equilibrium at the local temperature and pressure is assumed. The integral terms for the skin friction and heat transfer in Eqs. (11) and (12) for these types of flows can be obtained by rigorous solutions of the boundary layer equations (e.g., Ref. 19) if the initial conditions are defined or average values can be obtained from data correlations if available. The latter was chosen for the analysis herein. Bulk heat transfer rates Q_w from the tests with injection from discrete holes (Runs 108, 110 and 114-127) are summarized in Fig. 12. The average heat transfer rate per unit surface area Q_w/A_w is normalized by the inlet mass flux $\dot{w}_a/A_{ci}$ and the average gas-wall enthalpy difference defined as:

$$\Delta h \equiv h_{t_a} + f h_{t_f} + 0.5\, f \eta_c \cdot \Delta H_f - \bar{h}_w \qquad (14)$$

where h_{t_a} and h_{t_f} are the total enthalpies of the incoming air and fuel respectively, and $\bar{h}_w$ is the enthalpy of air at the average wall temperature. The factor of 0.5 multiplying the heat release parameter $f \cdot \eta_c \cdot \Delta H_f$ is intended to yield an average for the overall combustor. Certain license has been taken in drawing the correlating curve, the attempt being to minimize the rms of the scatter and to provide agreement with results (not shown here) from tests with liquid fuels in the same combustors (Ref. 20). The normalizing parameter adequately accounts for the effects of wall temperature considering the overall grouping of the zirconia coated wall data with the remaining data. Computed gas side surface temperatures varied from 880°K (1580°R) for $ER \cdot \eta_c = 0$ to 1930°K (3480°R) for $ER \cdot \eta_c = 0.61$ for the coated wall, whereas an uncoated wall having the same heat transfer at the corresponding $ER \cdot \eta_c$ would have had temperatures of 390°K (700°R) and 700°K (1260°R) respectively. The range of variation of $\dot{w}_a$ (1.37-1.42 kg/s (3.01 - 3.14 lb/sec)) and h_{t_a} (2.30 to 2.65 MJ/kg (990-1141 Btu/lb)) for the data is limited, so it is somewhat presumptuous to assume the general utility of the normalizing parameters until tests with broader variations in these quantities are made. With slot injection the $\bar{Q}/A_w$ values are apparently quite dependent on the properties of the film of hydrogen, i.e., the fuel temperature, flow rate and the combustor geometry, and no simple correlating parameter was found.

(U) Assuming that the Reynolds analogy is valid for flow with exothermic reactions, it is possible to relate the heat transfer parameter to a shearing stress parameter C_f. To obtain the deduced shearing stress using Reynolds analogy, certain simplifying assumptions are necessary. The analogy is expressed:

$$\frac{\bar{Q}/A_w}{(\bar{h}_r - \bar{h}_w)} = \frac{\bar{\tau}_w \cdot g}{\bar{u}} \tag{15}$$

where $\bar{\tau}_w$ is the integrated shearing stress acting on the wall area $= \frac{1}{A_w}\int \tau_w dA_w$ and $\bar{h}_r$ is the average value of the recovery enthalpy of the gas. The average velocity $\bar{u}$ can be taken as u_{ci}, since the decelerating effects due to the precombustion shock and heat addition are about cancelled by the accelerating effects due to combustor divergence as shown in Ref. 19. Defining the shear parameter as:

$$\bar{C}_f = \frac{2\bar{\tau}_w}{\rho_{ci} u_{ci}^2} \tag{16}$$

and noting that $\dot{w}_a = g\rho_{ci} u_{ci} A_{ci}$ results in

$$\frac{\bar{C}_f}{2} = \left[(\bar{Q}/A_w) / \frac{\dot{w}_a \, \Delta h}{A_{ci}} \right] \frac{\Delta h}{\bar{h}_r - \bar{h}_w} \tag{17}$$

where the bracketed term is the heat flux parameter defined above and Δh is given in Eq. 14. Whereas, the simple definition of the average total enthalpy as the arithmetic mean of the combustor inlet and exit enthalpies was suitable when used to normalize the heat transfer data, a more appropriate representation is needed when defining $\bar{h}_r$ in order to obtain reasonable values of $\bar{C}_f$.

(U) To be consistent with the usual definition of recovery enthalpy $\bar{h}_r \equiv C_1 \bar{h}_t$ where

$$C_1 = \frac{1 + \bar{r}\left(\frac{\bar{\gamma} - 1}{2}\right)\bar{M}^2}{1 + \left(\frac{\bar{\gamma} - 1}{2}\right)\bar{M}^2} \approx 0.93 \tag{18}$$

for $\bar{M} \approx M_{ci} = 3.2$, $\bar{r} \approx (\text{Prandtl No.})^{\frac{1}{3}} \approx 0.9$. The average total enthalpy is defined as:

$$\bar{h}_t \equiv h_{t_a} + fh_{t_f} + C_2 \, f \cdot \eta_c \cdot \Delta H_f \tag{19}$$

(U) An estimate for C_2 can be obtained from Ref. 19 which presents the deduced longitudinal variation of total enthalpy for a test made in combustor configuration E. In this test, the enthalpy rose to nearly the exit enthalpy within the cylindrical section, and a value of $C_2 = 0.9$ is reasonable, and was assumed representative of all the data. Whether or not the local heat transfer is governed by the bulk enthalpy at a given location is not known. Due to the nonuniform distribution of fuel, local hot (or cold) zones located near the wall could result in higher (or lower) h_r than would correspond to bulk values.

(U) Figure 13 shows the $\bar{C}_f$ values for an example case with $T_{t_a} = 2030^{\circ}K$ ($3660^{\circ}R$); $T_{t_f} = 440^{\circ}K$ ($800^{\circ}R$) and $p_{t_a} = 3.17\ MN/m^2$ (460 psia) which is typical of the testing conditions. The mass flux at the combustor inlet for these conditions is $364\ kg/m^2s$ ($74.5\ lb/sec\ ft.^2$). To obtain the gas enthalpy at the average wall temperature, it was assumed that the walls were the same as in the uncoated combustors, i.e. $1.6 \times 10^{-3}m$ (0.0625 in.) thick type 310 stainless steel and the coolant side temperature was $310^{\circ}K$ ($560^{\circ}R$). Solving the heat conduction equation for $\bar{Q}/A_w$ yields $\bar{T}_w$ and in turn $\bar{h}_w$, but it should be noted that the resulting $\bar{C}_f$ is only weakly dependent on $\bar{h}_w$, i.e. a $330^{\circ}K$ ($600^{\circ}R$) change in $\bar{T}_w$ results in only a 1% change in $\bar{C}_f$. Even though the particular values of $\bar{C}_f$ are unique for the particular example chosen, the characteristic of increasing $\bar{C}_f$ with increasing heat release is presumably characteristic of supersonic combustors. Moreover, values of 0.002 for the local skin friction coefficient are quite reasonable for turbulent flows entering the combustor in a typical engine.

(U) In order to obtain solutions to Eqs. (9-12) it is necessary to formulate the wall pressure force which is taken to be

$$p_w A^{\epsilon/(\epsilon-1)} = \text{constant} = \frac{p_s}{p_a} p_a (A_a)^{\epsilon/(\epsilon-1)} \qquad (20)$$

(where ϵ is an arbitrary constant $-\infty \leq \epsilon \leq \infty$ (Ref. 21))

$$\int_a^b p_w \sin\alpha \, dA_w = (1-\epsilon)\left(p_b A_b - \frac{p_s}{p_a} p_a A_a\right) \qquad (21)$$

where p_s is the pressure immediately downstream of the precompression shock. Solutions for these equations, with certain restrictions discussed later, can be obtained for combinations of combustor area ratios, fuel flow rates, and shock compression ratios (p_s/p_a) using a high speed computer.

(U) The salient features of this analysis are more easily discussed for the simple case of a calorically perfect gas with $\tau_w = q_w = 0$. With these restrictions the following property relationships can be expressed explicitly in terms of γ, M_b (the exit Mach number) and p_s/p_a.

$$\frac{p_b}{p_a} = \left[\frac{(1 + \gamma M_a^2) - (1-\epsilon)\, p_s/p_a}{\epsilon + \gamma M_b^2}\right]^{\epsilon}\left(\frac{p_s}{p_a}\right)^{1-\epsilon} \tag{22}$$

$$\frac{A_b}{A_a} = \left[\frac{\frac{p_a}{p_s}(1 + \gamma M_a^2) - (1-\epsilon)}{\epsilon + \gamma M_b^2}\right]^{1-\epsilon} \tag{23}$$

$$\frac{T_{t_b}}{T_{t_a}} = \left[\frac{2 + (\gamma-1)M_b^2}{2 + (\gamma-1)M_a^2}\right]\left(\frac{M_b}{M_a}\right)^2\left[\frac{(1 + \gamma M_a^2) - (1-\epsilon)\frac{p_s}{p_a}}{\epsilon + \gamma M_b^2}\right]^2 \tag{24}$$

(U) Relationships for the particular cases of $\epsilon = \pm\infty$ and $\epsilon = -\gamma M_b^2$ are readily obtained using the same procedure as in Ref. 21. Solutions for various stagnation temperature ratios in a given area ratio combustor are generally desired, but since no explicit relationship ($T_{t_b}/T_{t_a} = f(A_b/A_a, M_a, \gamma, p_s/p_a)$) can be obtained, Eqs. (23) and (24) are solved simultaneously using standard iterative procedures.

(U) Results for a particular set of initial conditions, $M_a = 3.2$ and $\gamma = 1.4$, for a combustor having an area ratio of 2 and $\tau_w = q_w = 0$ are shown in Fig. 14. Sets of T_{t_b}/T_{t_a} curves are given for selected values of the pressure ratio across the shock in the combustor inlet. For clarity, only three sets of curves are shown: for no shock, for an oblique shock with $p_s/p_a = 2.9$, and for a normal shock with $p_s/p_a = 11.78$. Similar sets of curves could be generated for other values for $1 < p_s/p_a < 11.78$. However, solutions for $9.71 < p_s/p_a < 11.78$ may not be meaningful, because they belong to the family of strong rather than weak oblique shocks. Each set is bounded above by the stagnation temperature ratio which results in a sonic exit limit, $M_b = 1.0$. The lower bound corresponds to an entropy limit, which, in effect, means that solutions from the ϵ = constant family having the same initial conditions, but a lower T_{t_b}/T_{t_a} would require a negative entropy change. The value of ϵ corresponding to the limiting condition is obtained from the implicit relationship:

$$\frac{\bar{\epsilon}}{\bar{\epsilon} + \gamma(1-\bar{\epsilon})} = \frac{\frac{p_a}{p_s}\left(\frac{1}{\gamma} + M_a^2\right) - \left(\frac{1-\bar{\epsilon}}{\gamma}\right)}{\left(A_b/A_a\right)^{1/(1-\bar{\epsilon})}} - \frac{\bar{\epsilon}}{\gamma} \tag{25}$$

Note that

$$\bar{\varepsilon} = \gamma\, \bar{M}_b^{\,2}/[1+(\gamma-1)\bar{M}_b^{\,2}] \qquad (26)$$

and

$$0 \leq \bar{\varepsilon} \leq \gamma/(\gamma-1) \qquad (27)$$

These two constraints result in ranges of possible T_{t_b}/T_{t_a} that increase with increasing p_s/p_a. However, for any total temperature ratio between unity (no heat release) and the maximum possible value corresponding to a normal shock with $M_b = 1.0$, there are an infinite number of possible solutions that lie within the prescribed p_s/p_a bounds.

(U) At this point the desirability of predicting the most probable of the permissible solutions for given initial conditions becomes apparent. Based on considerable experimental evidence it can be argued that the most probable solutions are those having the lowest p_b/p_a ratios for a given T_{t_b}/T_{t_a} ratio, _if_ the required p_s/p_a is sufficient to separate the boundary layer in the combustor entrance. If the p_s/p_a required to obtain the minimum p_b/p_a is lower than the separation pressure ratio, then the injection- and combustion-induced disturbances generated in the combustor inlet are effectively dissipated, and the resulting process effectively corresponds to $p_s/p_a = 1.0$. In order that the most probable pressure-area distributions be of use for comparison with experimental results, heat transfer and shear as defined by the curves shown in Figs. 12 and 13, are included in real-gas calculations using nominal experimental values for the combustor inlet conditions.

(U) For the results shown in Fig. 15 the inlet conditions are $M_{ci} = 3.25$, $T_{ci} = 752^{\circ}K$ ($1354^{\circ}R$) and $p_{ci} = 5.11 \times 10^4 N/m^2$ (7.46 psia) which correspond to total conditions of $h_{t_a} = 2.32 MJ/kg$ (1000 Btu/lb)($T_{t_a} = 2037^{\circ}K$ ($3667^{\circ}R$)) and $p_{t_a} = 3.15 MN/m^2$ (460 psia). The combustor exit to inlet area ratio is 2.0 and the wall-surface to inlet-area ratio $A_w/A_{ci} = 42.8$. The fuel temperature is $670^{\circ}K$ ($1200^{\circ}R$) and uncoated walls and coolant conditions assumed in the $\bar{C}_f$ determination were used. The pressure-area distributions are shown in Fig. 15. For $ER_{eff} < 0.213$, the value of p_s/p_{ci} satisfying Equation 24 is less than 2.9, the approximate value required to separate a turbulent boundary layer at M_{ci} = 3.25 (Ref. 22), thus no precombustion shock is present. For $0.213 \leq ER_{eff} \leq 1.0$, combustion is preceded by an oblique shock, which varies in strength from $p_s/p_{ci} = 2.9$ to 10.62.

(U) Shown in Fig. 16 are results for theoretical calculations for cases in which the input conditions have been perturbed to cover the range of inlet air enthalpies and geometric variations tested. All cases are for $ER_{eff} = 0.5$ with shear and heat transfer defined as before. Figure 16a shows the effect of change of the enthalpy of the incoming air. Changes of plus or minus 0.137MJ/kg (200 But/lb) in h_{t_a} result in changes in p_s/p_{ci} of 4.61 and 7.34, respectively, about the value of 5.62 for the nominal case. In Fig. 16b the effects of changing the combustor area ratio A_{ce}/A_{ci} are shown. The extension of the curves (dashed portions) for $A_{ce}/A_{ci} = 1.50$ and 2.00 (the nominal case) beyond their respective locations of the completion of heat release to $A/A_{ci} = 2.50$ are based on isentropic expansion. For a given heat release, p_s/p_{ci} decreases with increasing area ratio, but pressure levels are nearly the same for $A/A_{ci} > 1.5$. Changes in slope at the A/A_{ci} values corresponding to the end of heat release in the smaller area ratio combustors are not evidenced because the entropy limit condition is met when the slope of the heat addition process $(dp/dA)_{\epsilon=c}$ is equal to the slope of an isentrope $(dp/dA)_{s=c}$ at this point. Thus, it would be difficult to deduce the effective location of the end of heat addition from pressures in this region in combustors having continuously increasing area. For example, in the 0.914m (36-in.) conical combustor (Configuration B) having a geometric $A_{ce}/A_{ci} = 2.59$, the heat release could be effectively completed at, say, $x = 0.617$m (24.3 in.), i.e., $A/A_{ci} = 2.00$, and the predicted downstream pressure distribution would be very nearly the same as for completion of heat release at the geometric combustor exit. Thus, to discriminate between the two hypothetical cases postulated, the upstream pressures would have to be examined. A second dilemma arises here in that wall static pressure in the region of the shock/boundary-layer interaction and separation are not, in general, the same as their more representative in-stream counterparts, which are very difficult to obtain experimentally. This point will become clearer in the subsequent discussion of the experimental pressure distributions.

(U) In Fig. 16c the effect of changes in the surface area A_w/A_{ci}, for the same A_{ce}/A_{ci} are shown. Changes in A_w/A_{ci} result in proportional changes in both $\bar{Q}_w$ and $\bar{\tau}_w A_w$, but the latter is by far the more significant effect. Increasing $\bar{Q}_w$ decreases p_s/p_{ci} and the downstream pressure distribution, whereas increasing $\bar{\tau}_w A_w$ has just the opposite effect. For example, the increased heat transfer associated with the increase in A_w/A_{ci} from 42.2 (nominal case) to 69.2 would decrease p_s/p_{ci} by 15%. However, the increased shear would increase p_s/p_{ci} by 36%; thus, the net effect is the 21% increase shown.

COMPARISON OF THEORETICAL AND EXPERIMENTAL RESULTS

(C) Having the theoretical predictions, it is now possible to make comparisons with experimental pressure distributions. Wall static pressure ratios for the $ER_{eff} = 0.80 \times 0.72 = 0.572$ and the cold point from Run 108 are shown as the data points in Fig. 17. The theoretical pressure distributions based on the above analysis are indicated as the smooth curves. It should be emphasized here that the value of ε used to generate the theoretical curve results from the calorimetrically determined combustion efficiency using the analytical procedure just described and not simply an arbitrary choice to produce a good fit with the measured static pressure distribution. The presence of the pre-combustion shock is clearly evidenced in the burning case, although the measured wall pressures in the vicinity of the injector are somewhat lower than the theoretical prediction. It is possible that instream pressures would yield even closer correspondence of theory with experiment, but, even so, the agreement is quite good considering all the assumptions needed to perform the analytical calculations and the known deviation from one-dimensional flow. The theoretical curve for the cold point was based on one dimensional flow with shear and heat transfer defined by the curves in Figs. 12 and 13. Similar correspondence of this theory with experimental data is shown in Refs. 17, 19, and 21.

(C) For the theoretical method to be valid, there should also be agreement between the other combustor exit properties measured and the theoretical values. These comparisons are shown in Fig. 18. The radial variations of the pitot pressure ratios and deduced combustor exit Mach numbers are shown. Although the data reveal the presence of a radial gradient in combustor exit flow properties, the theoretical calculations yield a good approximation for the average value. For this case the heat addition has decreased the combustor exit Mach number from the cold flow value of 3.44 to 1.70. The corresponding decrease in the mass averaged total pressure is from 1.78 to 0.48 MN/m^2 (259 psia to 70 psia). The large loss in total pressure from 3.10 to 1.78 MN/m^2 (449 psia to 259 psia) for the cold-flow case is due to the wall shear. In the burning case the wall shear loss is even greater and contributes more to the total pressure loss than does the heat addition. This example clearly illustrates the importance of minimizing surface area in the supersonic combustor.

(C) In Runs 112-129 the effects of changes in combustor geometry on combustor performance were investigated. Previous testing of liquid-fueled supersonic combustors in a program sponsored by the United States Navy (Ref. 3) had shown the beneficial effect of the presence of an abrupt step increase in area at the combustor entrance in isolating the disturbance caused by the pre-combustion shock from the upstream flow. Similar beneficial effects had also been observed when a constant-area section was placed upstream of the fuel-injection station. In combustor configuration E (Runs 112-114) a constant-area section consisting of a water-cooled cylinder and a ring calorimeter was first placed downstream of the fuel injector to determine the effects of the added length on performance. In configuration F (Run 116) the same section was placed upstream of the injector to measure the extent of the upstream propagation of the pre-combustion pressure rise. In configuration G (Runs 119-121) the upstream half of the conical combustor was replaced with a 8.33×10^{-2}m (3.28-in.)-diameter cylindrical section to produce a 1.37×10^{-2}m (0.54-in.) step increase in diameter just downstream of the injector and match the entrance diameter of the downstream conical section. The upstream ring calorimeter was not in use in this configuration. Configuration H (Run 123) removes the downstream conical section and configuration I (Run 127-129) adds back in the upstream ring calorimeter.

(C) Representative pressure distributions for each of the combustor configurations are shown in Fig. 19. With the injector close-coupled to the air supply nozzle as in Run 114 (Fig. 19a) the high pressures caused by the pre-combustion shock are evidenced at the injector and presumably propagate into the air supply nozzle. Since pressure instrumentation was not provided in the nozzle the extent of the upstream feedback is now known. With the constant-area section moved upstream of the injector (Run 116) the pressure rise ahead of the injector could be determined (Fig.19b) The extent of the upstream propagation varied directly with the strength of the pre-combustion disturbance but did not extend into the air supply nozzle at the highest ER tested. Figures 19c and 19d show that the placement of an abrupt step increase just downstream of the injector essentially prevents the upstream propagation of the pressure rise. In Fig. 20 the pressure distributions for the four runs having nearly the same heat release parameter (ER_{eff} = 0.45-0.49) are replotted vs distance from the nozzle exit to show the effectiveness of the pressure isolation devices.

(C) Figure 21 shows effects of combustor configuration and ER on η_c for these runs. Comparison of the upper two lines at the same ER shows a 2% to 4% reduction in η_c associated with the 0.213 m (8.4-in.)shortening of the combustor. The long step-cyl-cone combustor G shows a strong dependence on ER, but when the cone is removed to make the short step-cyl combustor, η_c is insensitive to ER, but always relatively low ($\eta_c \simeq 0.7$). Comparison of combustors F and G shows the adverse effect of the step on η_c for combustors having nearly the same length; the reduction in η_c increases from 2% at ER = 0.5 to 6% at ER = 0.8.

(C) Losses in η_c include both kinetic effects and mixing inefficiency. Mixing inefficiency occurs when local regions in the flow have instantaneous values of fuel-air ratio greater than stoichiometric (ER > 1). Kinetic inefficiency can still cause a loss in η_c in regions where ER $\leq$ 1.0. The gas-sampling measurements show that for local ER < 0.4, the time-averaged η_c is generally equal to 1.0, and for ER > 0.4, η_c is less than 1.00. Presumably in the range 0.4 < ER < 1.0 kinetic losses are present, but this can not be unequivocally claimed, since the gas samples are withdrawn over a period of 7 seconds, and turbulence in the flow could present to the probe a fluctuating composition of gases including some instantaneous values above stoichiometric. A general trend of decreasing η_c with increasing overall ER would be expected, because parcels of gas with ER > 1 would appear more frequently. On the other hand, for fixed-geometry injectors as used herein, increasing ER results in increased fuel penetration and conceivably could yield a better fuel distribution for a particular injector-combustor geometry. A balancing of the two effects may explain the relative insensitivity of η_c to ER in the short step-cyl combustor.

(C) Figure 22 shows the radial variations of ER in the combustor exit plane for the same four combustors operating at overall ER_{eff} near 0.45. The combustors without steps (E and F), which gave higher η_c's, had relatively flatter profiles. For the step motor designs (G and H), almost no fuel penetrates to the combustor centerline, and relatively rich regions exist near the wall; the distribution is slightly more skewed for the shorter one (H). The deviation of the area-averaged ER from the overall ER for each case is due to the radial variation in mass flux and to circumferential variations in ER not accounted for in the limited number of samples.

(U) The short step-cyl design provides a means for isolating combustion-induced disturbances from the upstream flow, and it has a desirably small wall surface area (relatively low wall shear and heat transfer and less total pressure loss). However, it appears that the combination of the abrupt turning of the flow at the step together with the reduced length prevents the fuel from penetrating into the center of the combustor. Presumably the problem can be relieved by using in-stream injection from a low-drag injector in conjunction with wall injection. Tests of this type of combined injection are currently underway at the Applied Physics Laboratory.

SUMMARY AND CONCLUSIONS

(C) Tests of various direct-connect combustors have been made to determine the effects of injector and combustor geometry on the combustion characteristics of hydrogen for several combustor inlet conditions. The initial tests, which compared results from discrete-hole and wall-slot injectors in a 0.51m (20-in.)-long conical combustor, showed that:

1) For given initial air and fuel temperatures, combustion efficiency (η_c) is consistently higher with hole injection than with wall-slot injection.

2) Based on flight within the tropopause and $M_{ci} = M_0/3$, the minimum flight Mach numbers for autoignition and $\eta_c \geq 0.70$ are $M_0 = 6.3$ at a fuel-air equivalence ratio (ER) of 0.2, and $M_0 = 8.1$ @ ER = 0.8 with slot injection. The discrete-hole injectors permit operation at much lower flight speeds: $M_0 = 3.5$ @ ER = 0.4, and $M_0 = 4.7$ @ ER = 1.0.

3) Combustion efficiency increases with increasing combustor inlet temperature and decreases with increasing ER for either injector geometry.

A second set of tests was made with 0.61m (24-in.)-long conical combustors with and without zirconia-coated walls to determine the effects of combustor wall temperature on η_c for various fuel temperatures and injector designs. These tests showed that:

4) With wall-slot injection η_c increases by 3% to 8% when wall temperature is increased by 330 to 1000°K (600 to 1800°R).

5) Increasing fuel temperature produces significantly higher η_c with slot injection but has little effect on η_c with hole injection.

6) Equivalence ratio distributions obtained from gas samples in the combustor exit plane indicate that fuel distribution is the principal factor giving rise to higher η_c with hole injection. With slot injection at an overall ER near 0.5, a large region of rich flow (ER > 1) exists near the wall, whereas with hole injection no regions of ER > 1 are present.

In the final series of tests the effects of injector and combustor geometry on combustor performance showed that:

7) The presence of either a constant-area section ahead of the injectors or an abrupt increase in area downstream of the injector would provide an effective barrier to the upstream propagation of combustor-induced pressure disturbances.

8) For the longer combustors, η_c decreased by 10 to 15 percentage points when ER was increased from 0.5 to 0.8; e.g., for a 0.89m (35-in.)-long cyl-cone combustor, it dropped from 94% to 84%.

9) Decreasing combustor length from 0.89m to 0.69m (35 in. to 27 in.) resulted in a reduction of 2%-4% in η_c with cyl-cone-configurations.

10) Use of a step in a cyl-cone combustor of 0.74m (29-in.) length causes losses in η_c of 2% at ER $\approx$ 0.5 and 6% at ER $\approx$ 0.8.

11) For a short (0.38m (15-in.-long)) step-cyl combustor, η_c was insensitive to ER and was near 0.7 for the cases tested. This represents a loss of $\sim$ 20 percentage points in η_c at low ER (0.5) compared to a 0.74m (29-in)-long step-cyl-cone design.

(C) From the foregoing results it is judged that performance of a short step combustor could be substantially improved by some in-stream injection to place a portion of the fuel near the combustor centerline. Such a combustor would still provide the desired isolation of the air inlet from the combustor and would have low surface area, low friction loss, and low cooling requirements.

(U) Complementing the experimental program was the development of a theoretical analysis which yields an excellent description of the bulk processes taking place in the supersonic combustor. This analysis postulates that with sufficient heat release the combustion is preceded by a compression wave. With correlations for the wall shear and heat transfer obtained from the experiments the theoretical method can be used to predict the strength of the pre-combustion shock, the pressure-area distribution in the combustor and one-dimensional values for properties in the combustor exit plane. Comparisons of theoretical and experimental values for each of these are quite favorable.

REFERENCES

1. Yates, C. L.; Billig, F. S.; and Dugger, G. L.: Experimental Results and data Analysis Techniques of a Hydrogen-Fueled Supersonic Combustor (U). (Confidential), NASA CR-531, August 1966.

2. Billig, F. S.; and Grenleski, S. E.: Experimental Studies of Hydrogen-Air Ignition in a Supersonic Combustor (U). (Confidential), Applied Physics Laboratory, The Johns Hopkins University, TG-848, August 1966.

3. Billig, F. S.; and Grenleski, S. E.: Direct-Connect and Free Jet Tests of SCRAM Engine (U). (Confidential), AIAA 5th Propulsion Joint Specialists Conference, Colorado Springs, Colorado, June 9-13, 1969.

4. Billig, F. S.; Pirkle, J. C.; Yates, C. L.; and Dugger, G. L.: Research on Liquid Injection into a Supersonic Air Stream and Scramjet Fuels Evaluation (U). (Confidential), Air Force Aero Propulsion Laboratory Rept. No. TR-70-17, May 1970.

5. Colley, W. C.; and Harsha, P. T.: Performance Tests of a Supersonic Combustor Having a Wall Step Flameholder (U). (Confidential), General Electric Rept. R65FPD18, April 1965.

6. Schetz, J. A.: Preliminary Results of an Experimental Investigation of the Diffusion and Combustion of Hydrogen in Air at Supersonic Speeds (U). (Confidential), General Applied Science Laboratories, Inc., Technical Report No. 311, August 1962.

7. Supersonic Combustion Ramjet Sixth Quarterly Report (U). (Confidential), United Aircraft Research Laboratories, Report E910358-24, January 1967.

8. Dual Mode Scramjet Phase II (U). (Confidential), Marquardt Corporation, Report No. AF 33(615)-2834, January 1968.

9. Hypersonic Research Engine Project - Phase IIA Combustor Program Seventh Interim Technical Data Report (U). (Confidential), Garrett Corporation, AiResearch Manufacturing Division, Report No. AP-68-4439, November 18, 1968.

10. Cookson, R. A.; Flanagan, P.; and Penny, G. D.: A Study of Free-Jet and Enclosed Supersonic Diffusion Flames. Twelfth Symposium (International) on Combustion. The Combustion Institute, 1969, pp. 1115-1124.

11. Mestre, A.; and Viaud, L.: Combustion Supersonique Dans un Canal Cylindrique. Supersonic Flow Chemical Processes and Radiative Transfer. The Macmillan Company, New York, 1964, pp. 93-111.

12. Billig, F. S.; and Lasky, M.: "Flowfield Determination for Engine Testing" Section III-17, Research and Development Programs Quarterly Report, January-March 1971 (U). (Confidential), The Applied Physics Laboratory, The Johns Hopkins University, C-RQR/71-1.

13. Casaccio, A.; and Rupp, R. L.: A Supersonic Combustion Test Program Utilizing Gas Sampling, Optical and Photographic Measuring Techniques. NASA CR-66393, August 1967, Fairchild Hiller, Republic Aviation Division, Farmingdale, N. Y.

14. Orth, R. C.; and Land, H. B.: A Production Type Gas Chromatograph Analysis System for Light Gases. Journal of Chromatographic Science, Vol. 9, June 1971.

15. Cruise, D. R.: Notes on the Rapid Computation of Chemical Equilibria. J. Physical Chemistry, 68, 3798, 1964.

16. Billig, F. S.; and Dugger, G. L.: The Interaction of Shock Waves and Heat Addition in the Design of Supersonic Combustors. Twelfth Symposium (International) on Combustion. The Combustion Institute, 1969, pp. 1125-1139.

17. Wagner, J. P.; Cameron, J. M.; and Billig, F. S.: Penetration and Spreading of Transverse Jets of Hydrogen in a Mach 2.72 Airstream. NASA CR-1794, March 1971.

18. Yates, C. L.: Two Dimensional, Supersonic Mixing of Hydrogen and Air Near a Wall. NASA CR-1793, March 1971.

19. Billig, F. S.; and Grenleski, S. E.: Heat Transfer in Supersonic Combustion Processes. Fourth International Heat Transfer Conference, Paris-Versailles, August 1970, Vol. III Elsevier Publishing Co., Amsterdam 1970.

20. Grenleski, S. E.; Billig, F. S.; and Dale, L. A.: "Heat Transfer Measurements in Supersonic Combustors" Section III/10d, Research and Development Programs Quarterly Report, July-September 1970 (U). (Confidential), Applied Physics Laboratory, Johns Hopkins University, C-RQR/70-3.

21. Billig, F. S.: Design of Supersonic Combustors Based on Pressure Area Fields. Eleventh Symposium (International) on Combustion. The Combustion Institute 1967, pp. 755-769.

22. Mager, A.: On the Model of Free, Shock-Separated Turbulent Boundary Layer. J. of Aeronautical Sciences, Vol. 23, No. 2, pps. 181-184, February 1956.

TABLE I

Summary of Supersonic Combustion Test (U)

Run No.	$\dot{w}_a$ (kg/s)	P_{t_a} (MN/m^2)	h_{t_a} (MJ/kg)	M_{ci} +	$\dot{w}_f$ (kg/s)	P_{t_f} (MN/m^2)	T_{t_f} (°K)	ER	Combustion Efficiency η_c	T_{t_a} (°K)	T_{ci} (°K)	P_{ci} (MN/m^2)	Configuration*
78-1	1.28	3.17	3.835	2.80	0.012	0.77	796	0.31	0.93	3050	1279	0.103	A-c
-2	1.28	3.17	3.835	2.80	0.022	1.40	816	0.60	0.82	3050	1279	0.103	A-c
79-1	1.33	2.99	3.021	2.87	0.015	0.92	756	0.42	0.72	2534	1078	0.083	A-c
-2	1.33	2.92	3.254	2.86	0.008	0.63	756	0.20	0.95	2689	1133	0.084	A-c
81-1	1.53	3.10	2.394	2.92	0.012	0.68	756	0.26	0.33	2084	720	0.077	A-c
-2	1.64	3.09	2.394	2.92	0.022	1.29	756	0.50	0.20	2084	720	0.077	A-c
-3	1.52	3.12	2.440	2.92	0.035	2.05	756	0.80	0.17	2122	743	0.078	A-c
82-1	1.53	3.11	2.394	2.92	0.022	1.50	1033	0.50	0.20	2084	717	0.077	A-c
-2	1.53	3.10	2.394	2.92	0.033	2.25	1033	0.80	0.15	2084	717	0.077	A-c
83-1	1.32	2.89	2.380	2.92	0.025	1.88	778	0.65	0.85	2078	879	0.072	A-a
-2	1.31	2.90	2.405	2.92	0.016	1.17	820	0.41	0.96	2095	888	0.072	A-a
-3	1.31	2.86	2.343	2.92	------- Cold Point ---------------					2047	878	0.070	A-a
84-1	1.32	2.94	2.473	2.92	0.035	2.61	833	0.92	0.80	2145	912	0.072	A-a
-2	1.32	2.97	2.519	2.92	0.022	1.56	806	0.57	0.92	2178	947	0.074	A-a
-3	1.31	3.01	2.596	2.92	------- Cold Point ---------------					2217	957	0.075	A-a
87-1	1.34	2.76	2.071	2.94	0.040	2.81	817	1.02	0.66	1839	730	0.065	A-a
-2	1.34	2.74	2.054	2.94	------- Cold Point ---------------					1828	729	0.064	A-a
88-1	1.32	2.75	1.929	2.96	0.024	1.74	842	0.62	0.72	1733	691	0.061	A-a
-2	1.32	2.76	1.922	2.96	------- Cold Point ---------------					1731	692	0.066	A-a
89-1	1.39	3.24	2.419	3.27	0.024	1.90	974	0.59	0.82	2105	784	0.053	B-a
-2	1.39	3.24	2.421	3.27	------- Cold Point ---------------					2105	785	0.053	B-a
91-19	1.33	2.83	2.312	3.32	------- Cold Point ---------------					2025	747	0.046	B-a
92-19	1.34	2.88	2.301	3.32	0.038	2.47	897	0.96	0.88	2022	745	0.046	B-a
96-20	1.40	3.18	2.603	3.23	------- Cold Point ---------------					2242	851	0.052	D-d

TABLE I (cont'd)

Run No.	$\dot{w}_a$ (kg/s)	P_{t_a} (MN/m^2)	h_{t_a} (MJ/kg)	M_{ci} +	$\dot{w}_f$ (kg/s)	P_{t_f} (MN/m^2)	T_{t_f} (°K)	ER	Combustion Efficiency η_c	T_{t_a} (°K)	T_{ci} (°K)	P_{ci} (MN/m^2)	Configuration*
98-27	1.38	3.14	2.589	3.23	0.032	0.61	830	0.79	0.65	2228	845	0.052	D-d
-31	1.38	3.14	2.589	3.23	0.020	0.42	830	0.50	0.84	2228	845	0.052	D-d
100-17	1.39	3.23	2.761	3.23	0.034	2.43	930	0.84	0.64	2349	904	0.054	C-d
-21	1.39	3.23	2.745	3.23	0.021	1.73	907	0.53	0.71	2343	902	0.054	C-d
-25	1.38	3.23	2.754	3.23	-------	Cold	Point	-------	-------	2345	903	0.054	C-d
102-17	1.39	3.15	2.547	3.23	0.034	0.57	639	0.83	0.55	2200	831	0.052	C-d
-21	1.39	3.15	2.542	3.23	0.021	0.36	628	0.52	0.72	2197	828	0.052	C-d
-25	1.39	3.15	2.540	3.23	-------	Cold	Point	-------	-------	2195	828	0.052	C-d
104-34	1.37	3.14	2.531	3.23	0.034	0.31	292	0.85	0.49	2186	823	0.052	C-d
-38	1.39	3.14	2.526	3.23	0.022	0.22	292	0.53	0.39	2185	823	0.052	C-d
-42	1.39	3.14	2.529	3.23	-------	Cold	Point	-------	-------	2186	822	0.052	C-d
106-18	1.38	3.14	2.612	3.23	0.032	0.36	294	0.81	0.52	2248	855	0.052	D-d
-23	1.38	3.14	2.619	3.23	0.020	0.26	294	0.51	0.43	2251	856	0.052	D-d
-27	1.38	3.14	2.615	3.23	-------	Cold	Point	-------	-------	2249	855	0.052	D-d
108-29	1.38	3.10	2.456	3.23	0.032	1.21	287	0.80	0.72	2134	797	0.051	D-a
-33	1.38	3.10	2.461	3.23	0.020	0.77	287	0.51	0.82	2139	800	0.051	D-a
-37	1.38	3.10	2.461	3.23	-------	Cold	Point	-------	-------	2139	800	0.051	D-a
110-28	1.37	3.14	2.638	3.23	0.033	2.10	790	0.83	0.74	2264	862	0.052	D-a
-33	1.37	3.14	2.638	3.23	0.021	1.28	755	0.52	0.84	2264	862	0.052	D-a
-37	1.37	3.14	2.652	3.23	-------	Cold	Point	-------	-------	2275	868	0.052	D-a
112-26	1.36	3.21	2.840	3.23	0.031	0.67	677	0.79	0.61	2409	936	0.054	E-d
-31	1.36	3.21	2.835	3.23	0.020	0.38	665	0.50	0.75	2405	933	0.054	E-d
-35	1.36	3.21	2.826	3.23	-------	Cold	Point	-------	-------	2398	929	0.054	E-d
114-15	1.38	3.13	2.533	3.23	0.032	1.87	707	0.78	0.85	2189	825	0.052	E-a
-20	1.38	3.13	2.526	3.23	0.020	1.16	706	0.50	0.94	2179	820	0.052	E-a
-24	1.38	3.13	2.522	3.23	-------	Cold	Point	-------	-------	2178	819	0.052	E-a

TABLE I (cont'd)

Run No.	$\dot{w}_a$ (kg/s)	P_{t_a} (MN/m^2)	h_{t_a} (MJ/kg)	M_{ci} +	$\dot{w}_f$ (kg/s)	P_{t_f} (MN/m^2)	T_{t_f} (^{o}K)	ER	Combustion Efficiency η_c	T_{t_a} (^{o}K)	T_{ci} (^{o}K)	P_{ci} (MN/m^2)	Configuration*
116-16	1.38	3.14	2.542	3.22	0.031	1.70	643	0.78	0.81	2195	828	0.052	F-a
-21	1.38	3.14	2.552	3.22	0.020	1.06	644	0.49	0.92	2203	832	0.052	F-a
-24	1.38	3.14	2.589	3.22	-------	Cold Point	---	---	---	2231	844	0.052	F-a
119-58	1.40	3.10	2.433	3.22	0.033	1.93	671	0.80	0.70	2117	789	0.051	G-b
-62	1.40	3.10	2.438	3.22	0.021	1.18	658	0.51	0.89	2120	792	0.051	G-b
-67	1.40	3.10	2.436	3.22	-------	Cold Point	---	---	---	2119	791	0.051	G-b
121-55	1.40	3.08	2.380	3.22	0.038	2.21	626	0.93	0.68	2077	772	0.050	G-b
-58	1.40	3.08	2.391	3.22	0.031	1.71	626	0.76	0.77	2084	774	0.050	G-b
-63	1.40	3.08	2.403	3.22	-------	Cold Point	---	---	---	2092	779	0.050	G-b
123-3	1.42	3.08	2.301	3.22	0.029	1.73	664	0.70	0.70	2022	744	0.050	H-b
-5	1.42	3.08	2.303	3.22	0.023	1.30	650	0.56	0.74	2022	745	0.050	H-b
-7	1.42	3.08	2.310	3.22	-------	Cold Point	---	---	---	2025	747	0.050	H-b
127-64	1.41	3.17	2.496	3.22	0.039	2.14	580	0.94	0.73	2161	811	0.052	I-b
-68	1.41	3.17	2.510	3.22	0.032	1.65	556	0.77	0.72	2172	817	0.052	I-b
-72	1.41	3.17	2.512	3.22	-------	Cold Point	---	---	---	2173	817	0.052	I-b
129-121 } -334 }	1.39	3.16	2.580	3.22	0.033	1.94	710	0.81	0.65	2222	842	0.052	I-b
-350 } -593 }	1.39	3.19	2.638	3.22	0.026	1.51	694	0.64	0.67	2264	862	0.053	I-b
-594 } -858 }	1.39	3.14	2.533	3.22	-------	Cold Point	---	---	---	2186	825	0.052	I-b

+Mach 2.92 conical nozzle, Mach 3.23 contoured nozzle

*Capital letter indicates combustor (Fig. 3); small letter indicates injector (Fig. 2)

(THIS PAGE UNCLASSIFIED)

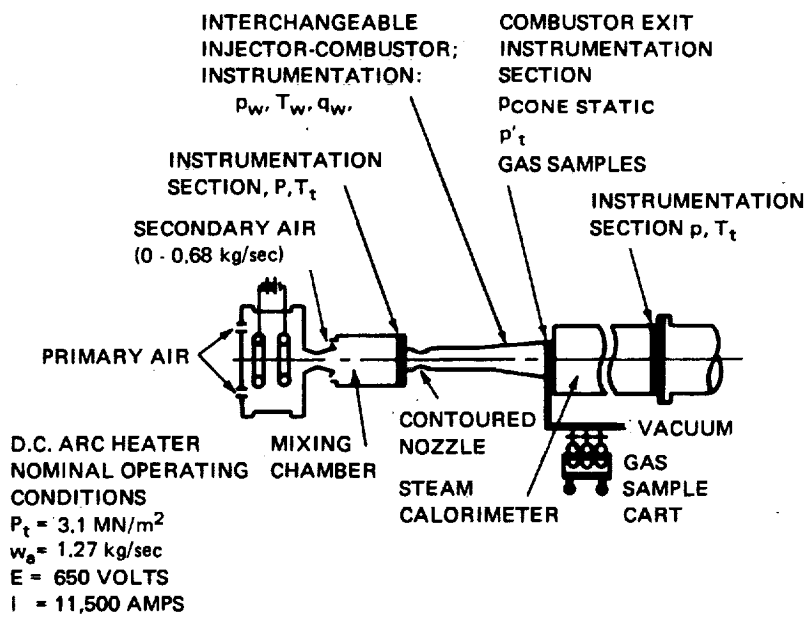

(U) FIG. 1 SCHEMATIC OF MACH 3.2 ARC HEATER SET-UP (U)

INJECTORS

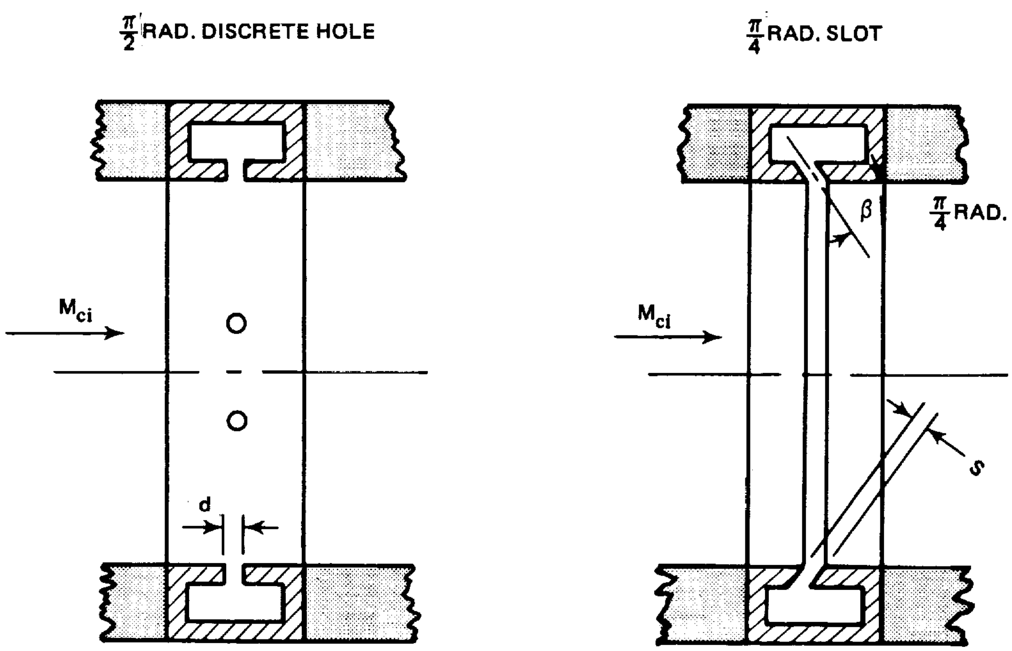

CODE	NUMBER OF HOLES	d (mm)
a	8	2.64
b	10	2.29

CODE	s (mm)
c	0.23
d	0.89

(U) FIG. 2 SCHEMATIC ILLUSTRATIONS OF FUEL INJECTORS (U)

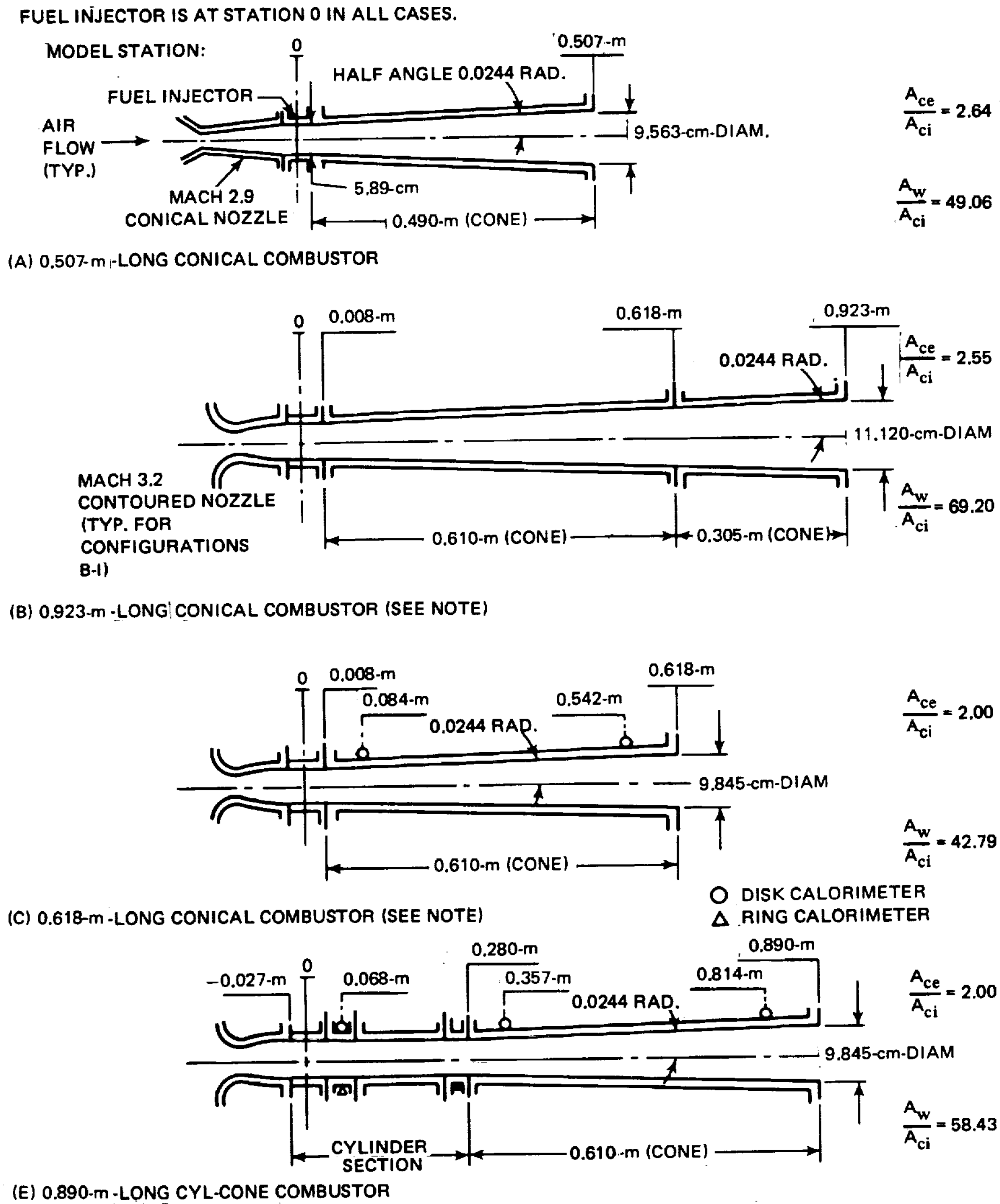

NOTE: CONFIGURATION D IDENTICAL TO C EXCEPT INSIDE SURFACE IS COATED WITH 0.0076 cm OF NICHROME AND 0.076 cm OF ZIRCONIA. CONFIGURATION B ALSO HAS THIS INNER SURFACE COATING ON CONICAL EXTENSION SECTION.

(C) FIG. 3 COMBUSTOR CONFIGURATIONS (U)

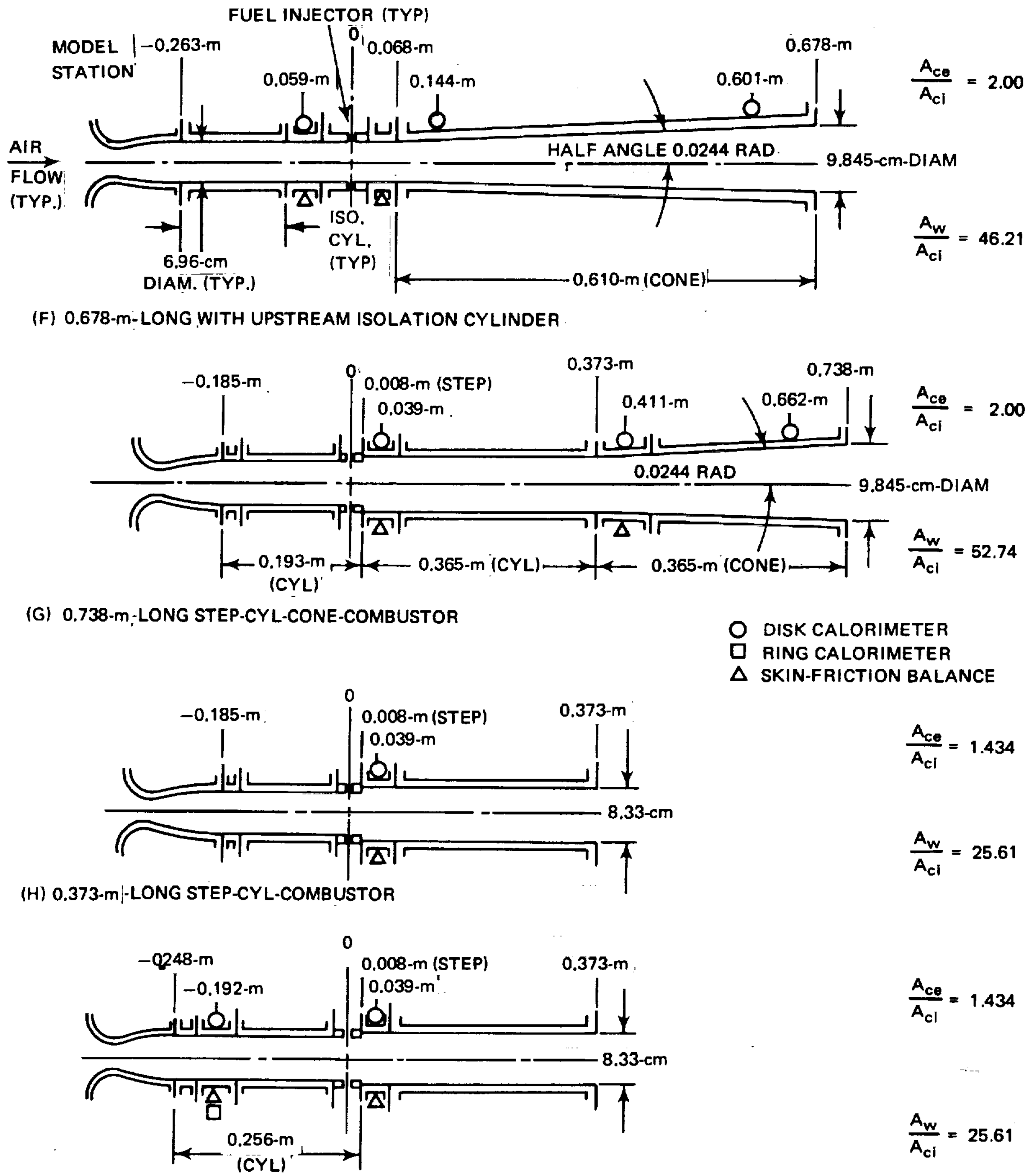

(F) 0.678-m-LONG WITH UPSTREAM ISOLATION CYLINDER

(G) 0.738-m-LONG STEP-CYL-CONE-COMBUSTOR

(H) 0.373-m-LONG STEP-CYL-COMBUSTOR

(I) 0.373-m-LONG STEP-CYL-COMBUSTOR WITH UPSTREAM CALORIMETER SECTION

(C) FIG. 3 (CONT'D) COMBUSTOR CONFIGURATIONS (U)

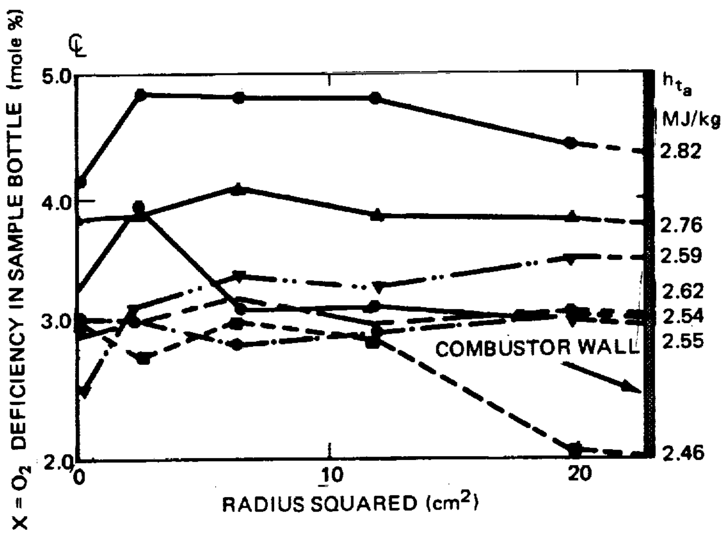

(U) FIG. 4 OXYGEN DEFICIENCY IN SAMPLE BOTTLE FOR VARIOUS TOTAL ENTHALPY LEVELS. (U)

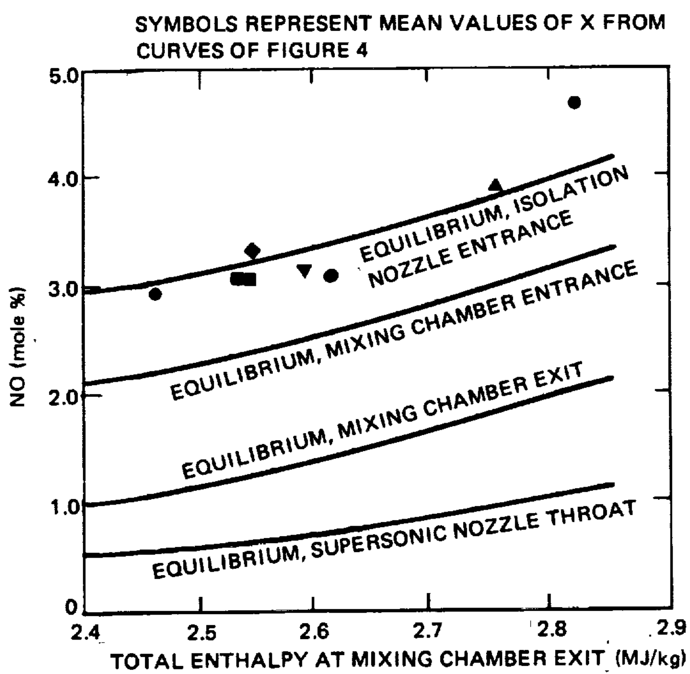

(U) FIG. 5 CONCENTRATION OF NO IN AIR STREAM. (U)

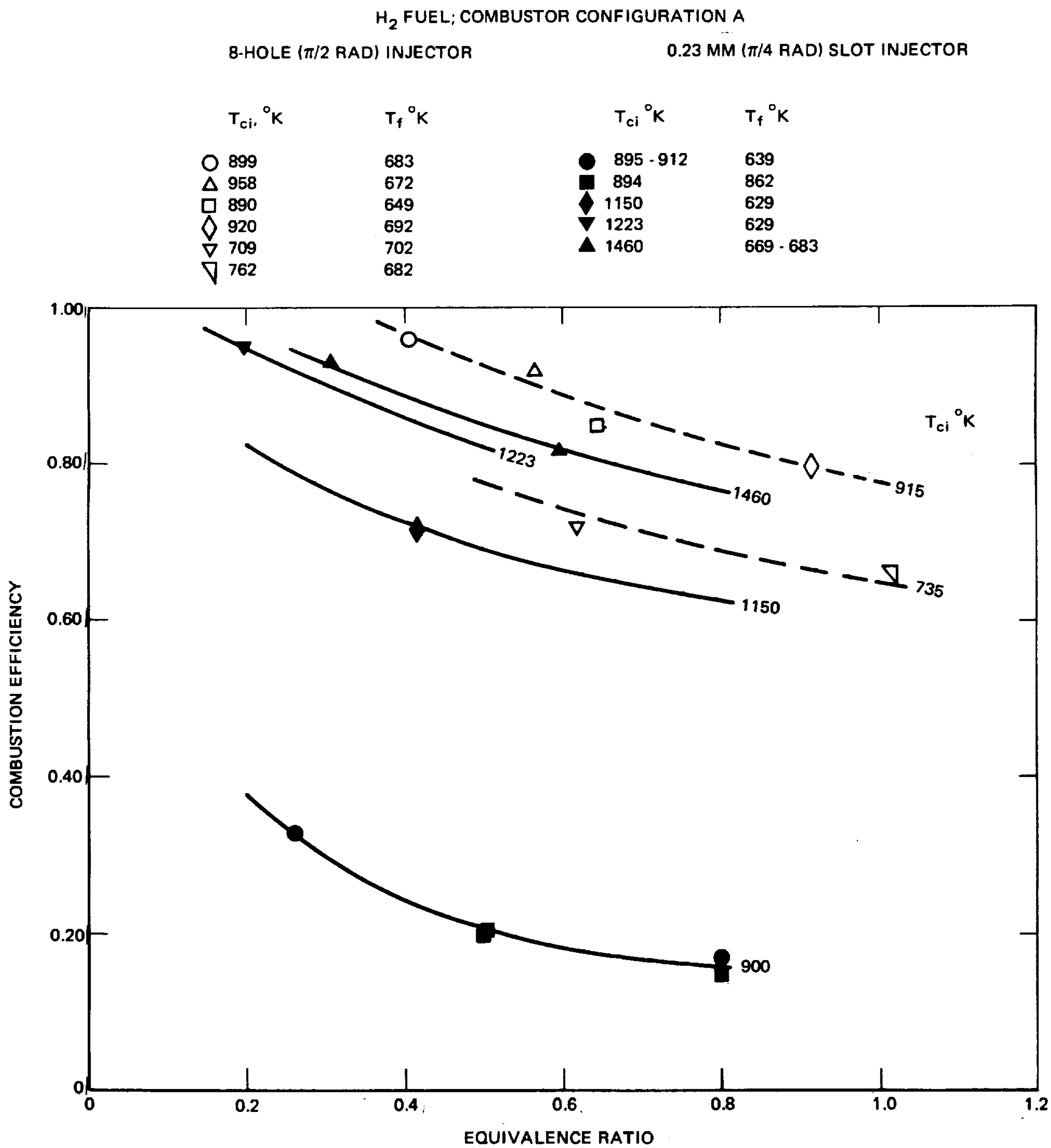

(C) FIGURE 6 COMBUSTION EFFICIENCY VS. EQUIVALENCE RATIO FOR HOLE- AND SLOT-TYPE INJECTORS (U)

H_2 FUEL, COMBUSTOR CONFIGURATION A
$T_f \sim 679\ ^{\circ}K$

FLIGHT CONDITIONS BASED ON: $M_{ci} = M_0/3$, $T_0 = 225^{\circ}K$

8-HOLE (π/2 RAD) HOLES INJECTOR		0.23 MM (π/4 RAD) SLOT INJECTOR	
	ER		ER
○	0.41	●	0.26,0.50,0.80
△	0.57	■	0.50,0.80
□	0.65	♦	0.42
◇	0.92	▼	0.20
▽	0.62	▲	0.31,0.60
◁	1.02		

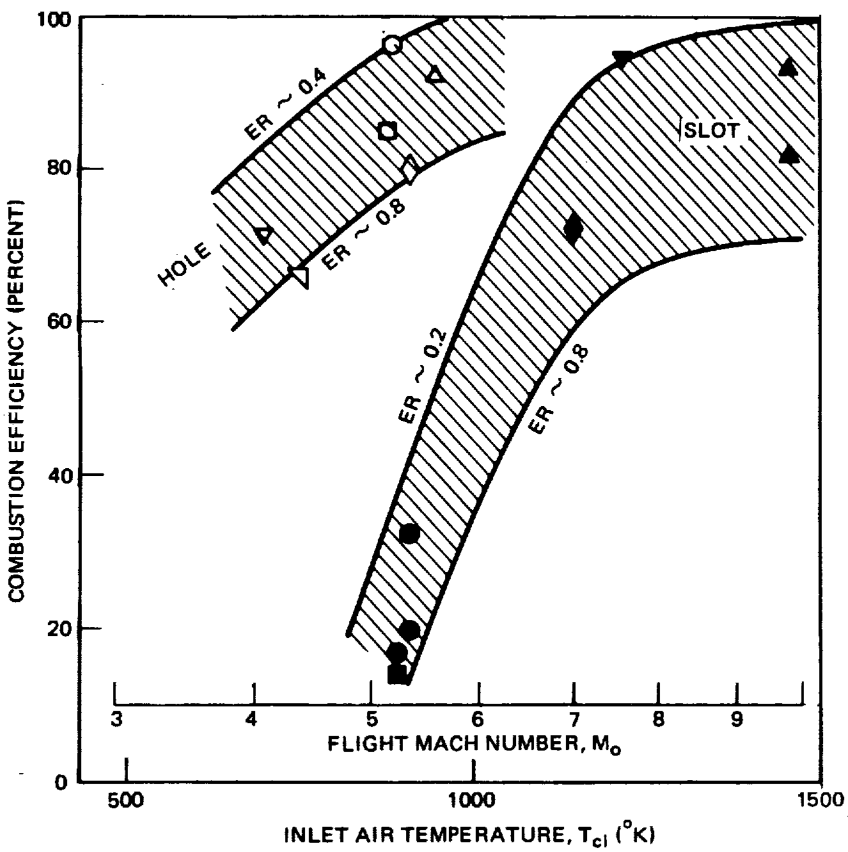

(C) FIG. 7 COMBUSTION EFFICIENCY VS. COMBUSTOR INLET AIR TEMPERATURE FOR HOLE AND SLOT TYPE INJECTORS (U)

COMBUSTOR CONFIGURATION A (0.507-m LONG CONICAL)

RUN NO.	COMB.	INJ.	ER	η_c
83-2	A	a	0.41	0.96

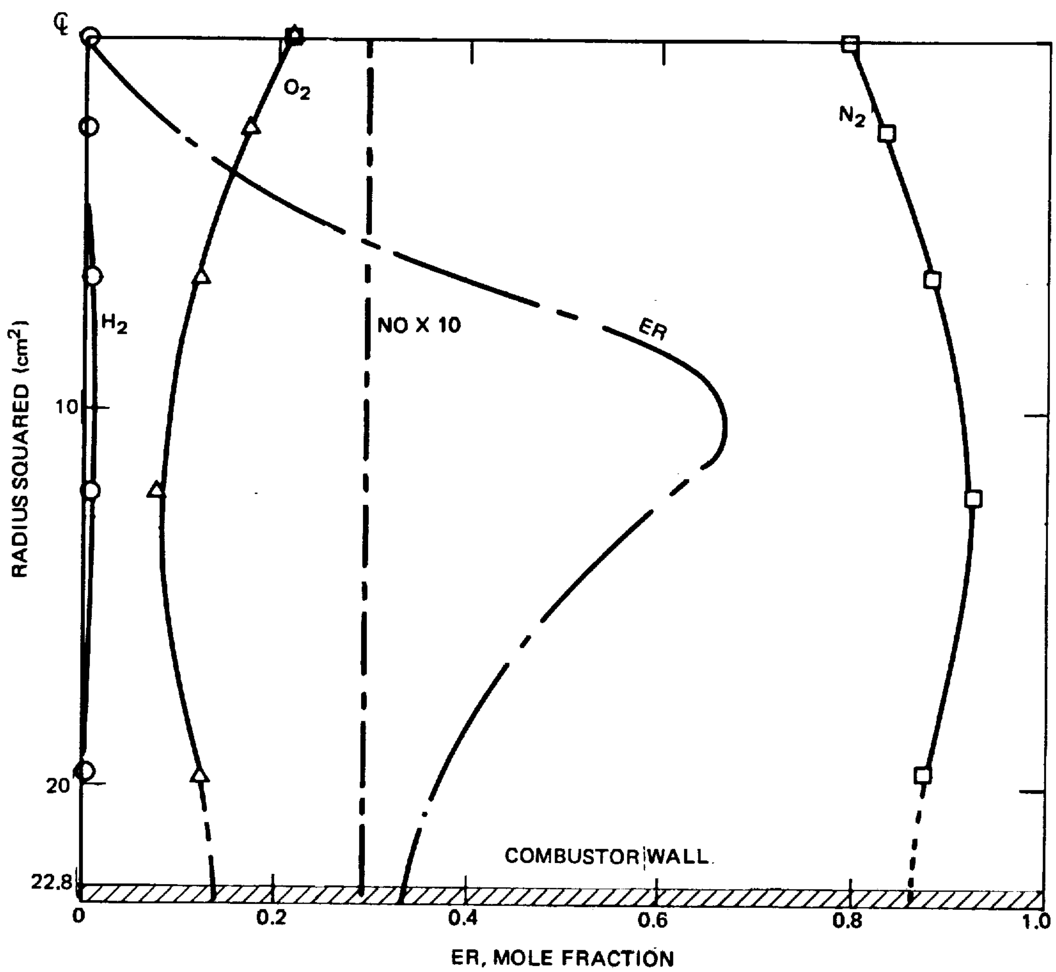

(C) FIG. 8 RADIAL VARIATION OF SPECIES, MOLE FRACTION AND DEDUCED ER IN COMBUSTOR EXIT PLANE (U)

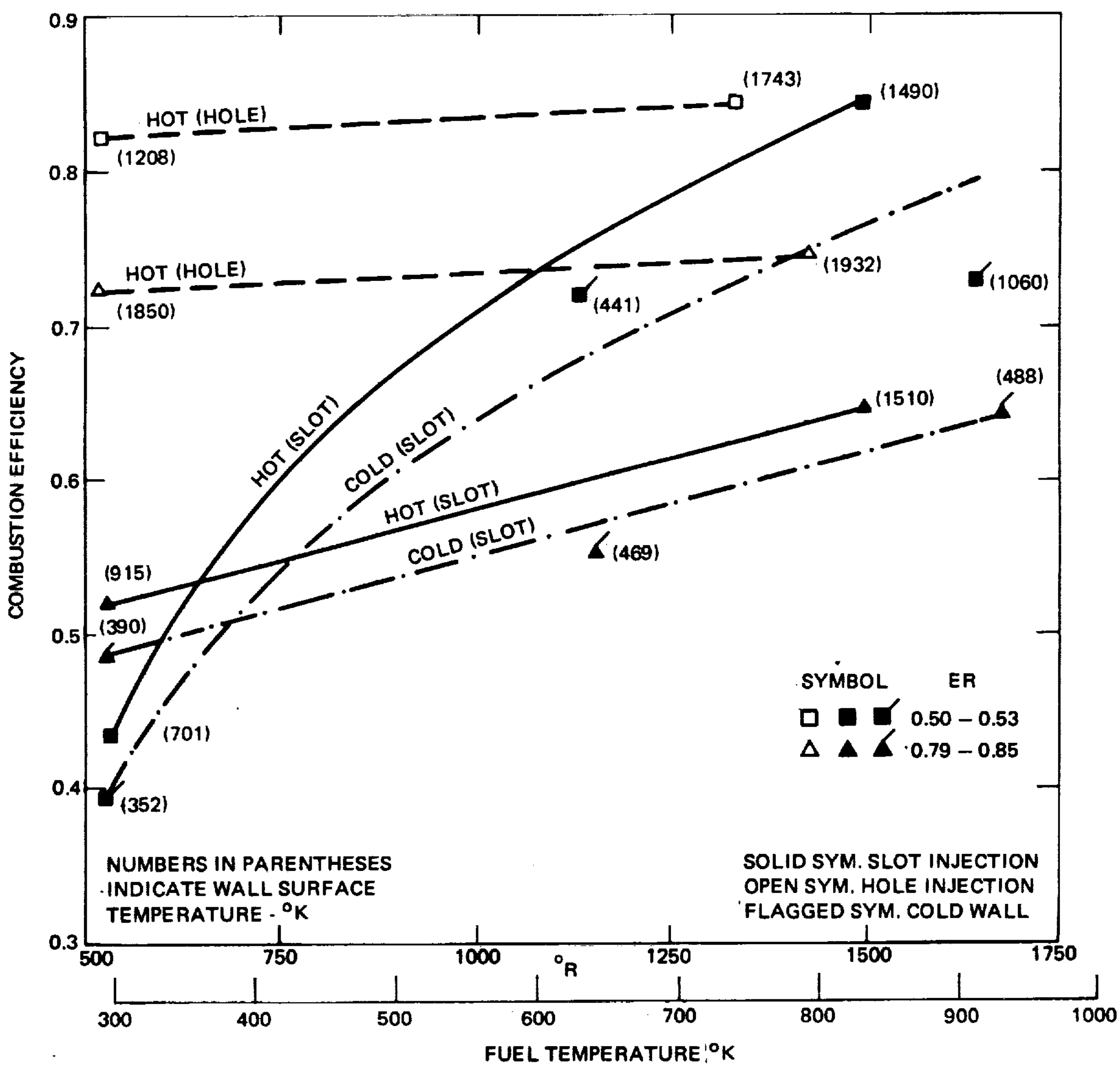

(C) FIG. 9 EFFECT OF INJECTOR GEOMETRY AND WALL TEMPERATURE ON EFFICIENCY (U)

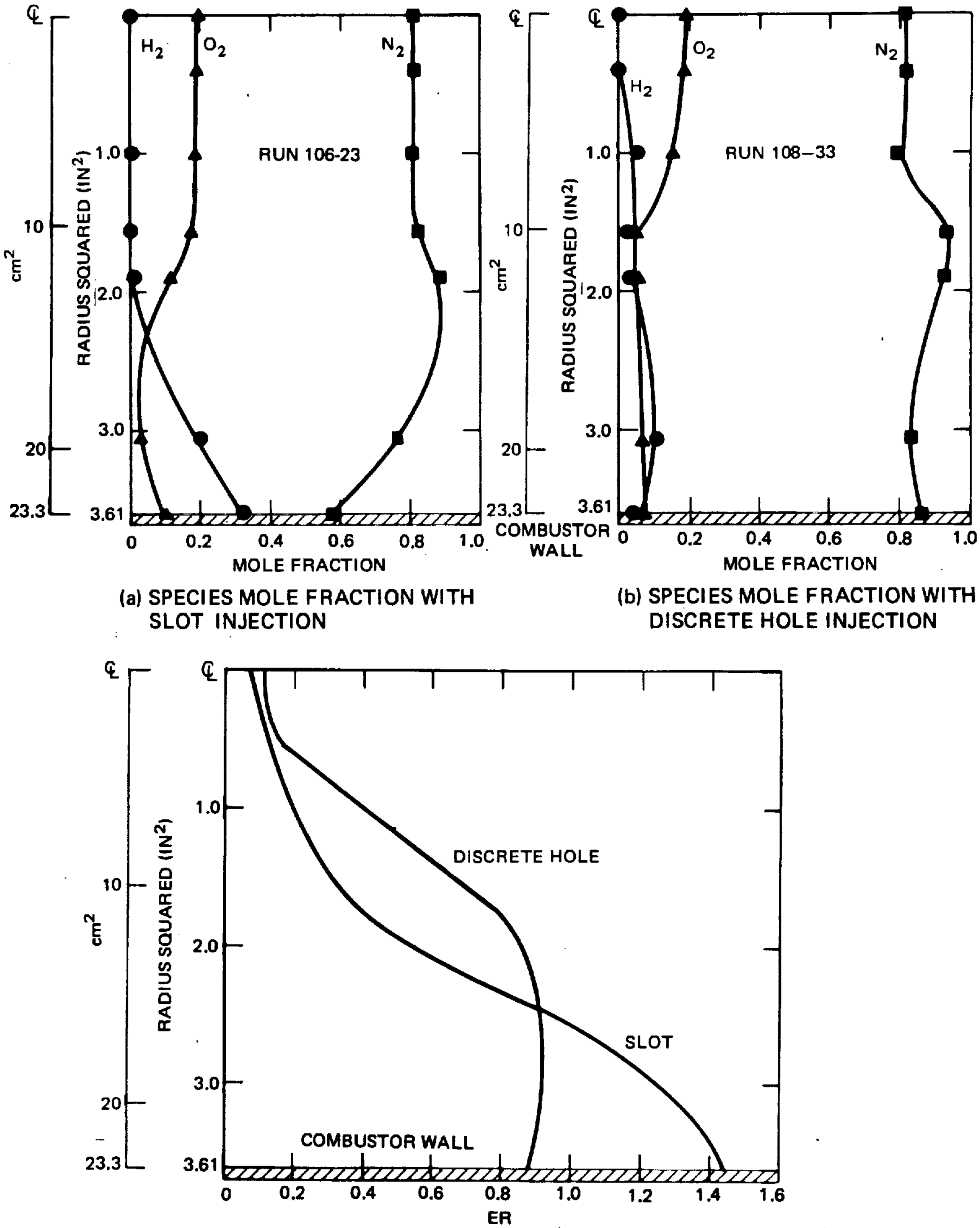

(a) SPECIES MOLE FRACTION WITH SLOT INJECTION

(b) SPECIES MOLE FRACTION WITH DISCRETE HOLE INJECTION

(c) DEDUCED ER DISTRIBUTION

(C) FIG. 10 RADIAL VARIATION OF GAS COMPOSITION IN COMBUSTOR EXIT PLANE 0.610-m LONG CONICAL COMBUSTOR (U)

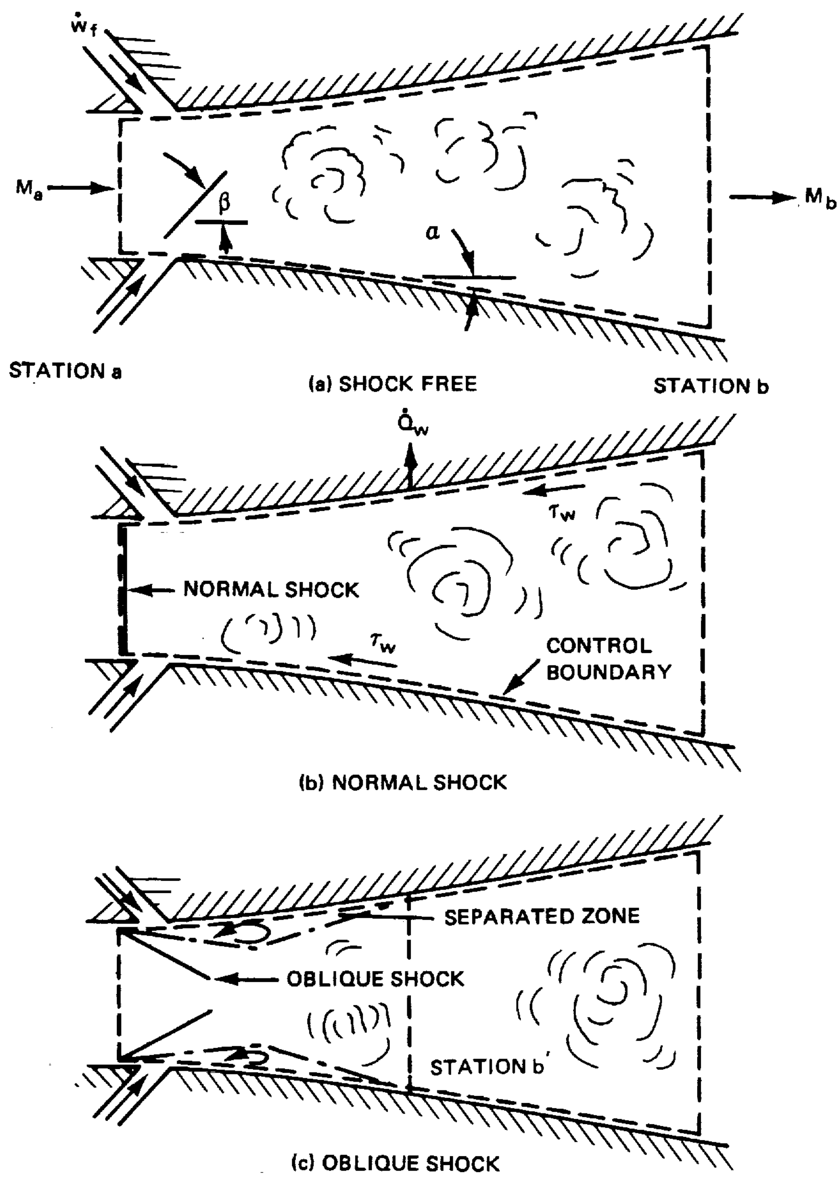

(U) FIG. 11 SCHEMATIC ILLUSTRATIONS OF COMBUSTION PROCESSES (U)

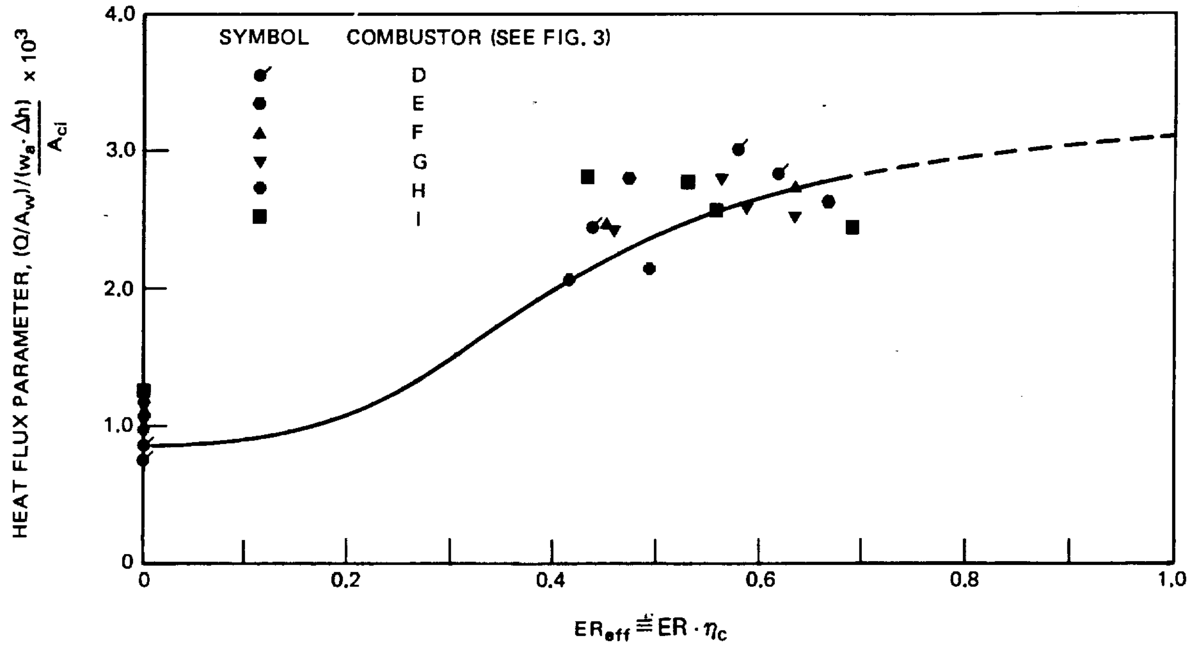

(U) Fig. 12 COMBUSTOR HEAT FLUX CORRELATION (U)

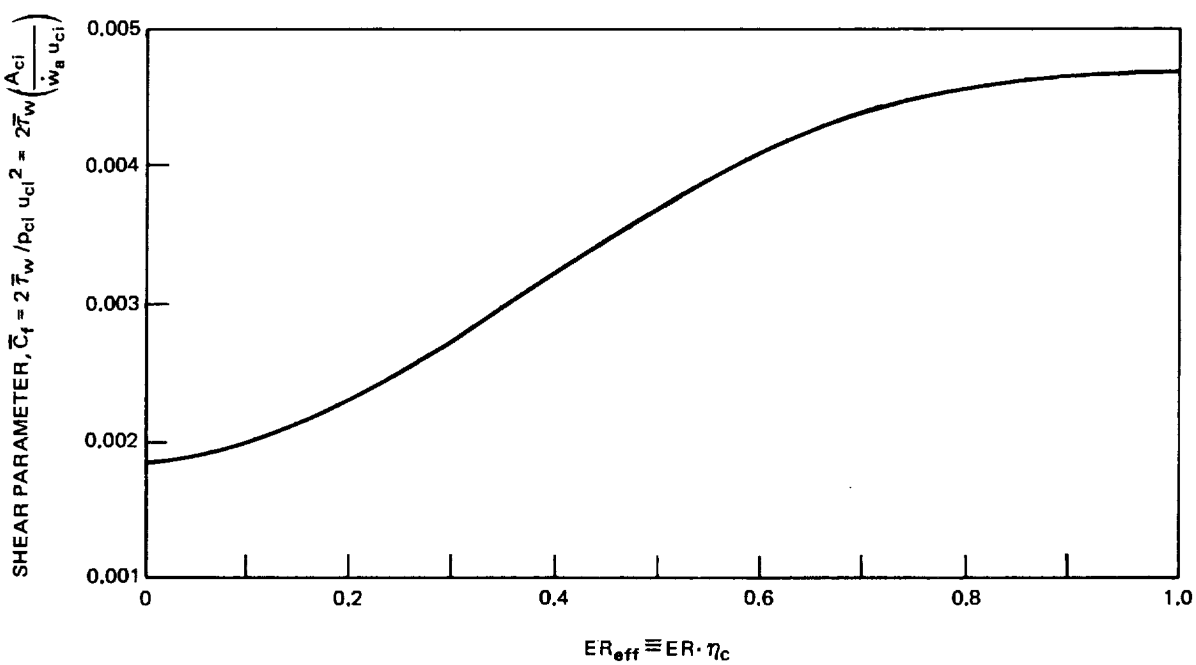

(U) Fig. 13 DEDUCED COMBUSTOR SHEAR PARAMETER (U)

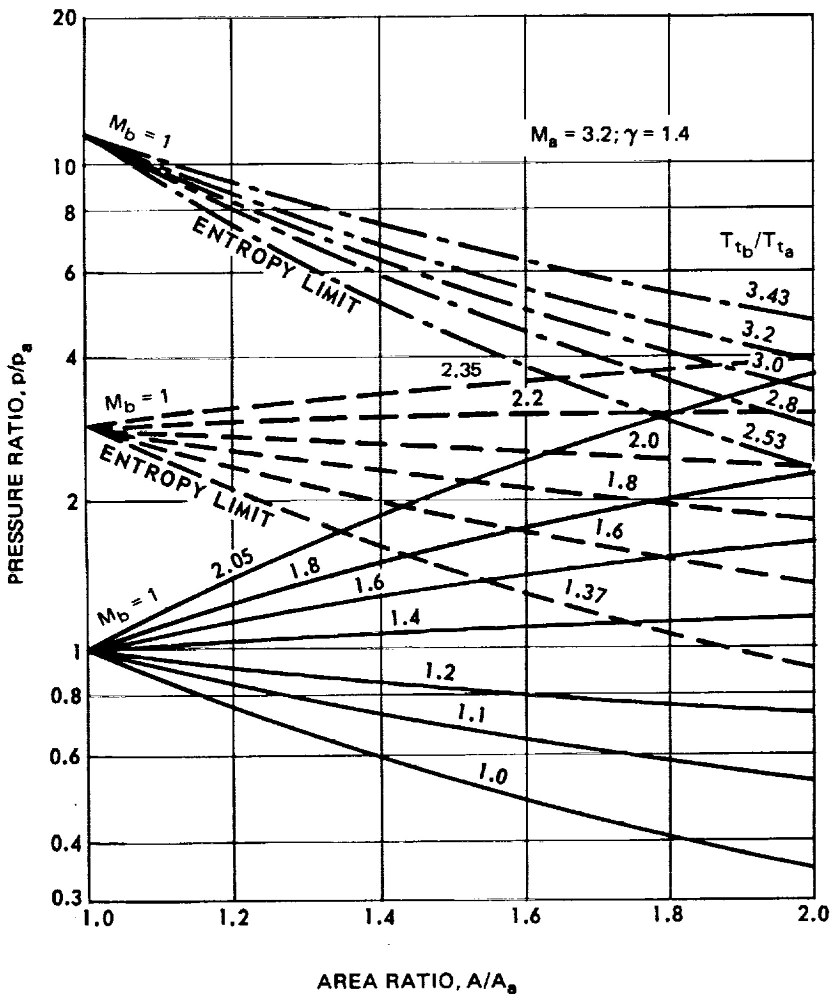

(U) FIG. 14 PREDICTED STATIC PRESSURE DISTRIBUTIONS FOR COMBUSTOR WITH AREA RATIO = 2 (U)

(THIS PAGE UNCLASSIFIED)

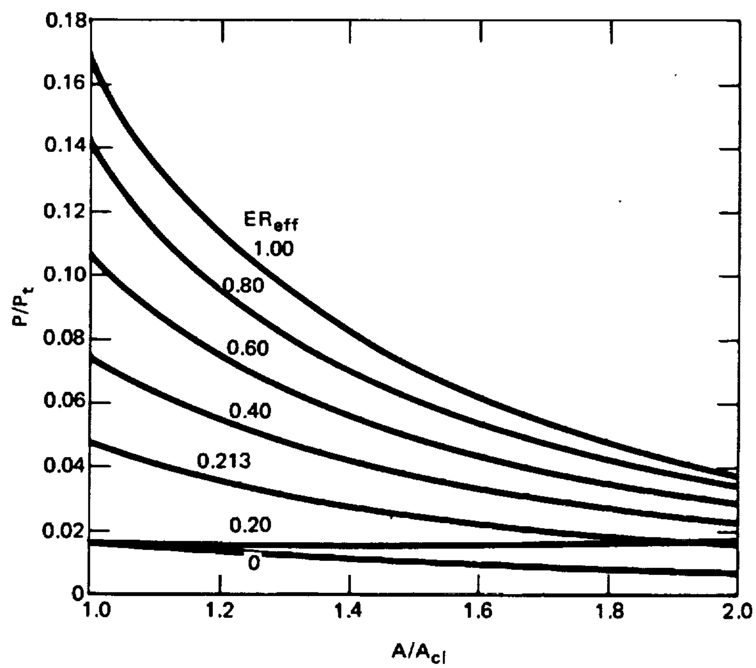

(U) FIG. 15 PREDICTED PRESSURE AREA DISTRIBUTION FOR COMBUSTOR WITH AREA RATIO = 2 (U)

NOMINAL CASE: h_{t_a} = 2.325 MJ/kg A_{ce}/A_{ci} = 2.0; A_w/A_{ci} = 42.2; ER_{eff} = 0.50;

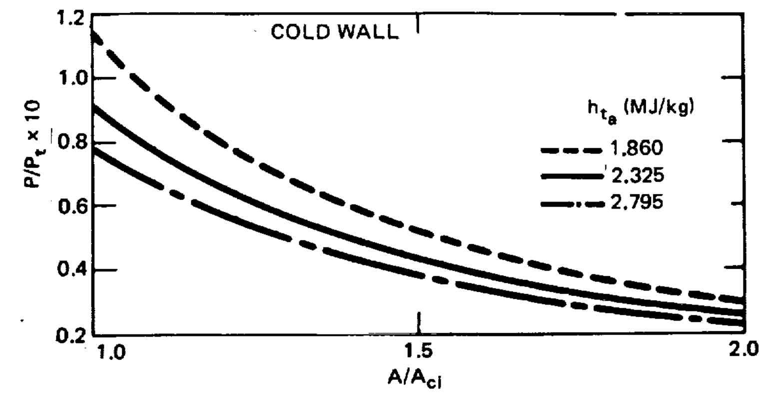

(a) PERTURBATION OF INLET AIR ENTHALPY

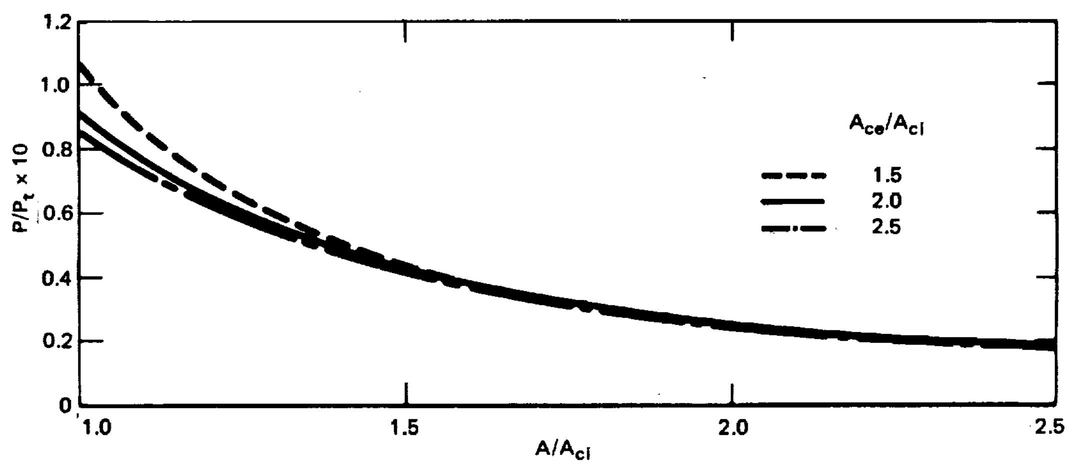

(b) PERTURBATION OF A_{ce}/A_{ci}

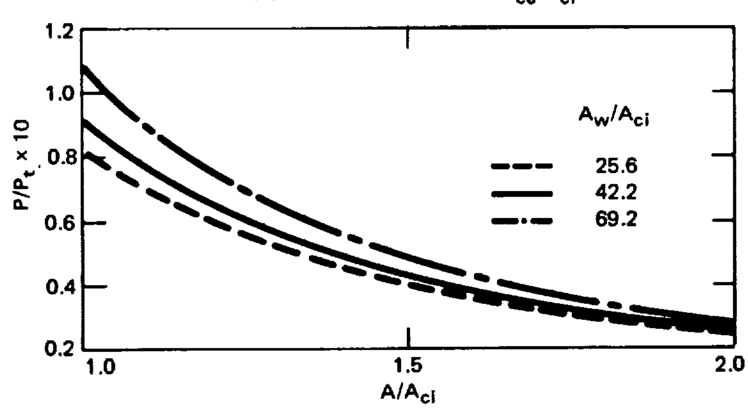

(c) PERTURBATION OF A_w/A_{ci}

(U) FIG 16 - EFFECTS OF PERTURBATION OF INLET AIR ENTHALPY AND COMBUSTOR GEOMETRY ON THEORETICAL COMBUSTOR PRESSURE DISTRIBUTION (U)

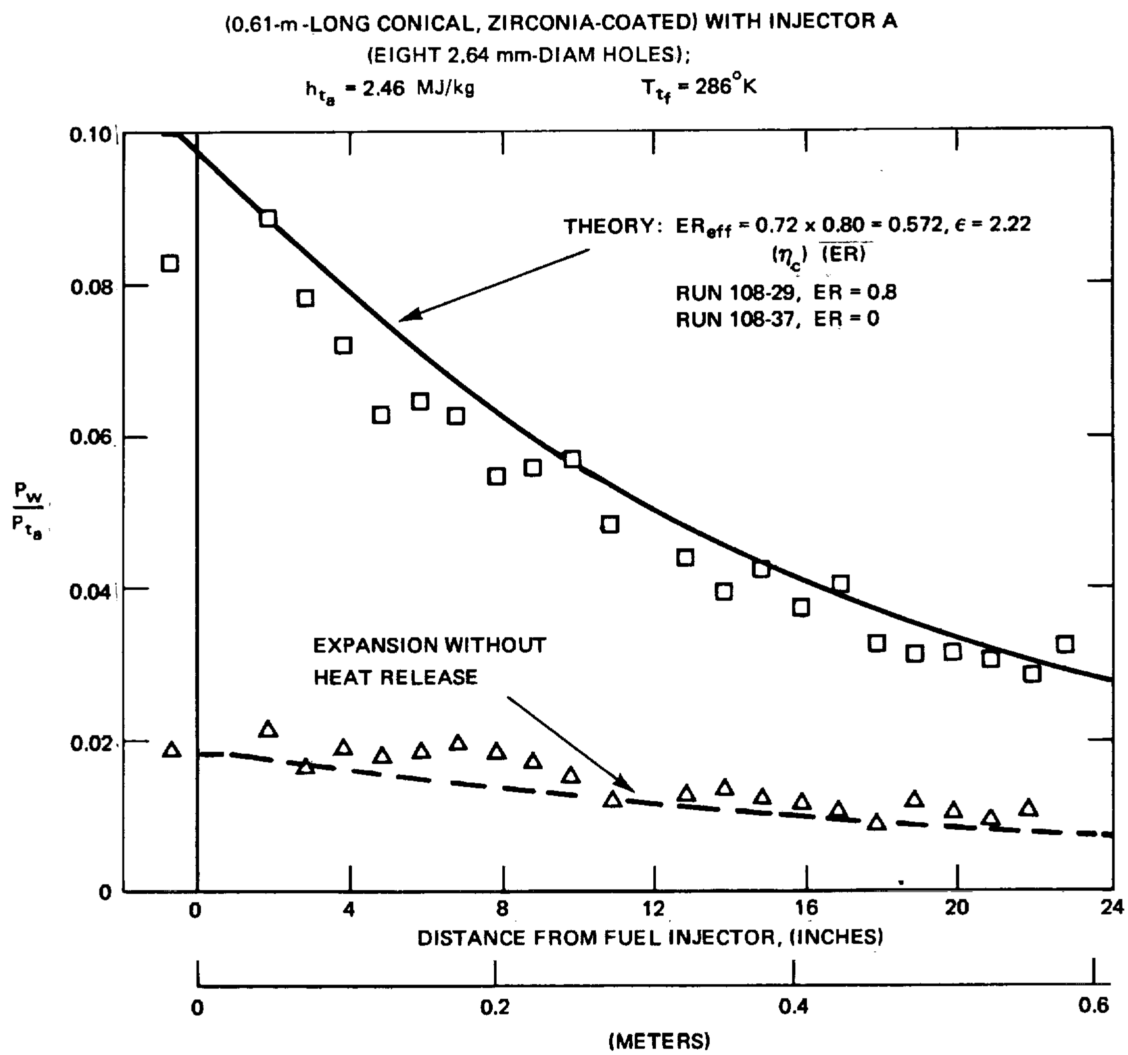

(C) FIGURE 17 COMPARISON OF EXPERIMENTAL AND THEORETICAL COMBUSTOR PRESSURE DISTRIBUTIONS FOR COMBUSTOR D. (U)

SYM.	RUN NO.	COMBUSTOR	INJECTOR	$\frac{P_{t_a}}{MN/m^2}$	ER	η_c
□	108-29	D	a	3.10	0.80	0.72

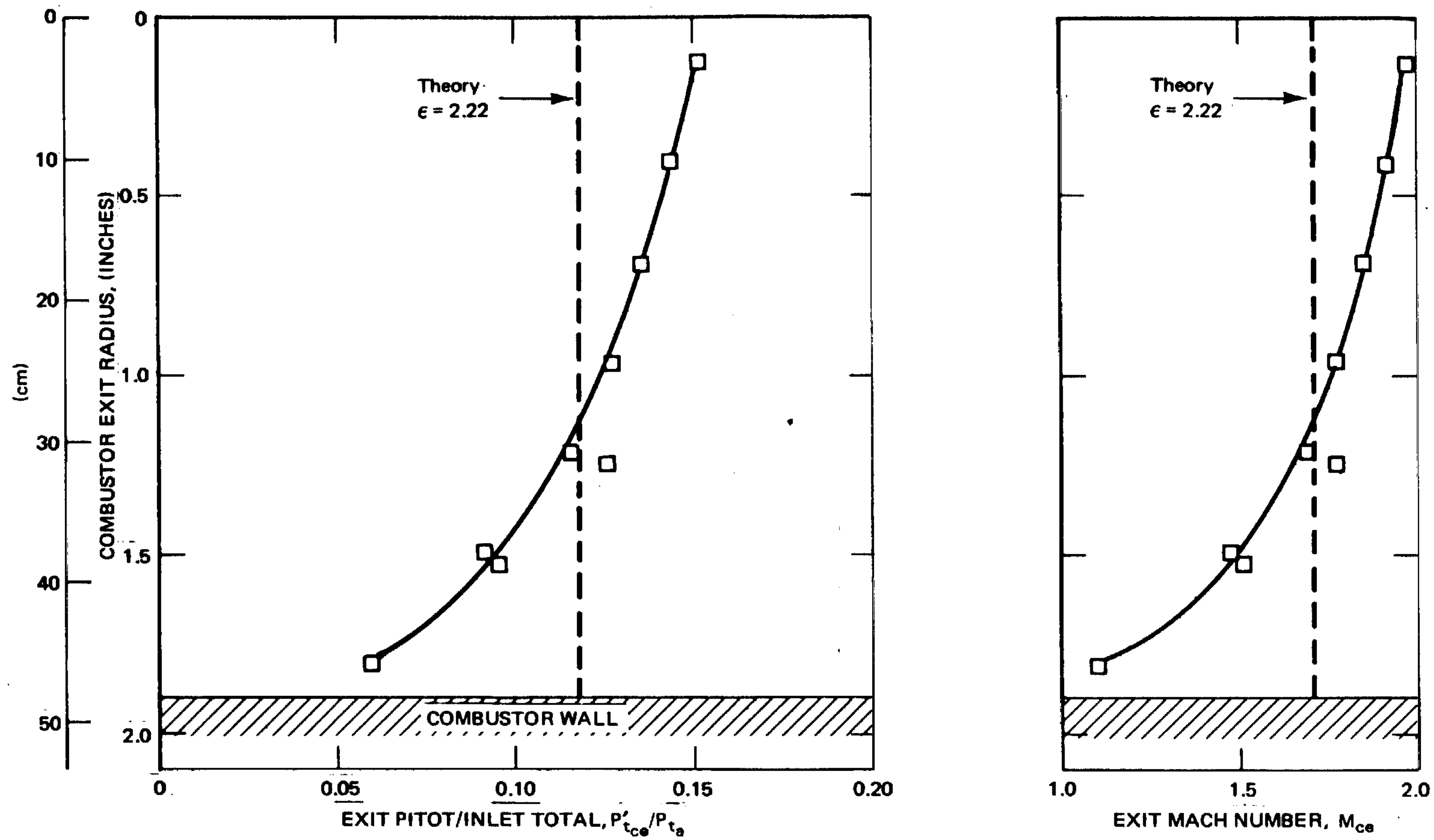

(C) FIG. 18 COMPARISON OF EXPERIMENTAL AND THEORETICAL COMBUSTOR EXIT PITOT PRESSURES AND MACH NUMBERS FOR RUN 108. (U)

~~CONFIDENTIAL~~

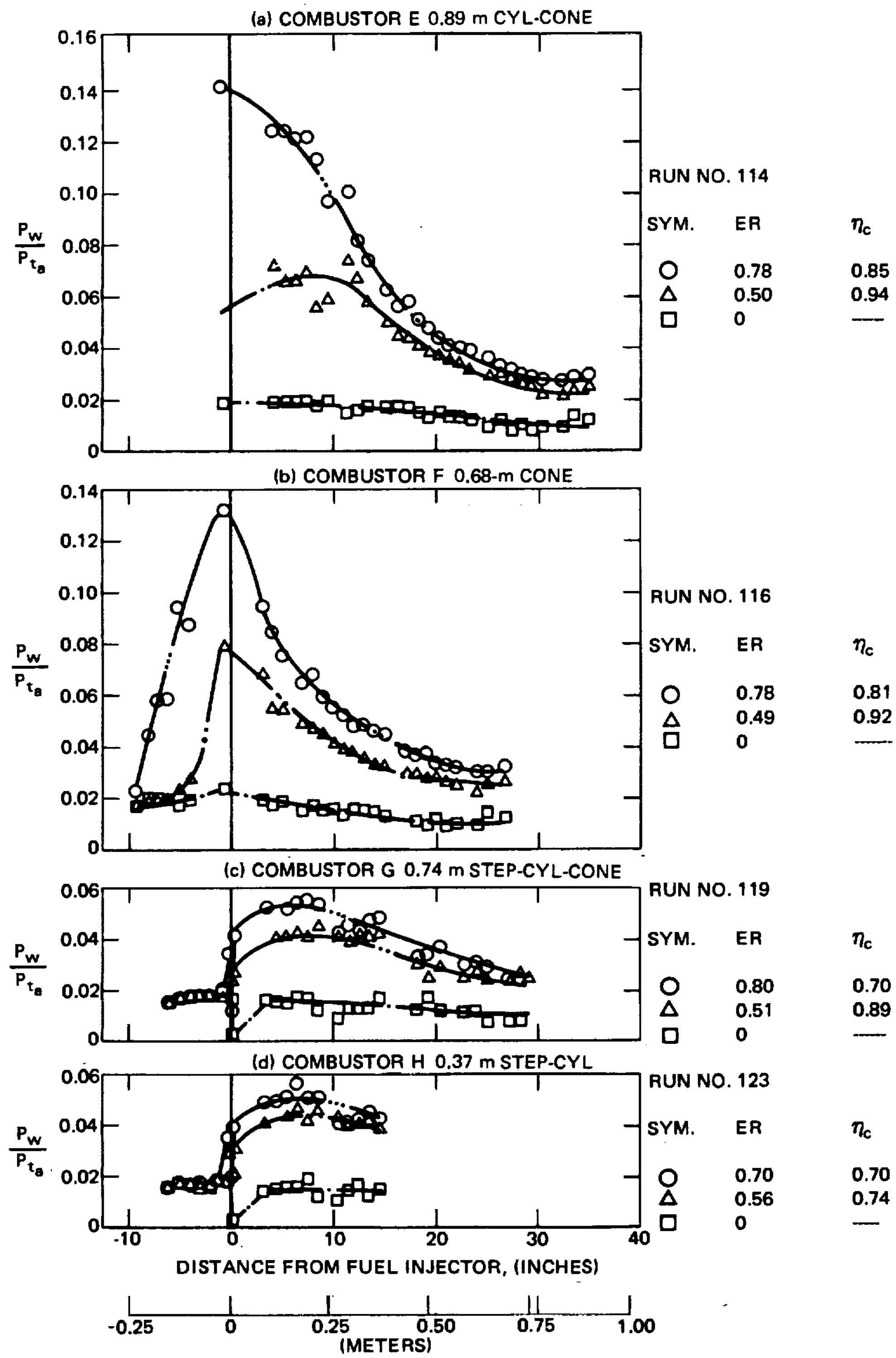

(C) FIGURE 19 COMBUSTOR STATIC PRESSURE DISTRIBUTIONS FOR FOUR COMBUSTOR GEOMETRIES. (U)

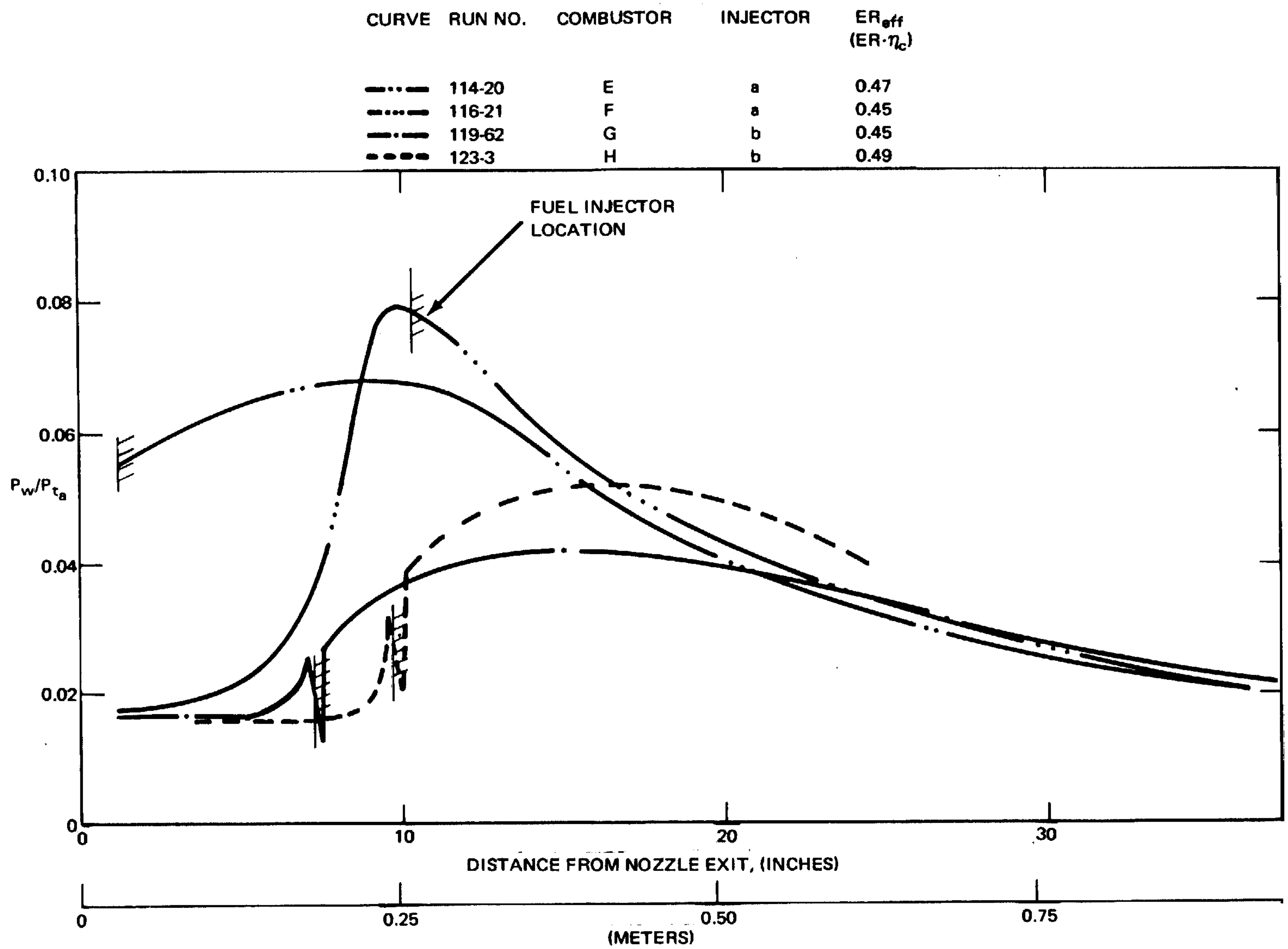

(C) FIGURE 20 EFFECT OF ISOLATION DEVICES IN ISOLATING UPSTREAM PRESSURE RISE AT $ER_{eff} = 0.47 \pm 0.02$ (U)

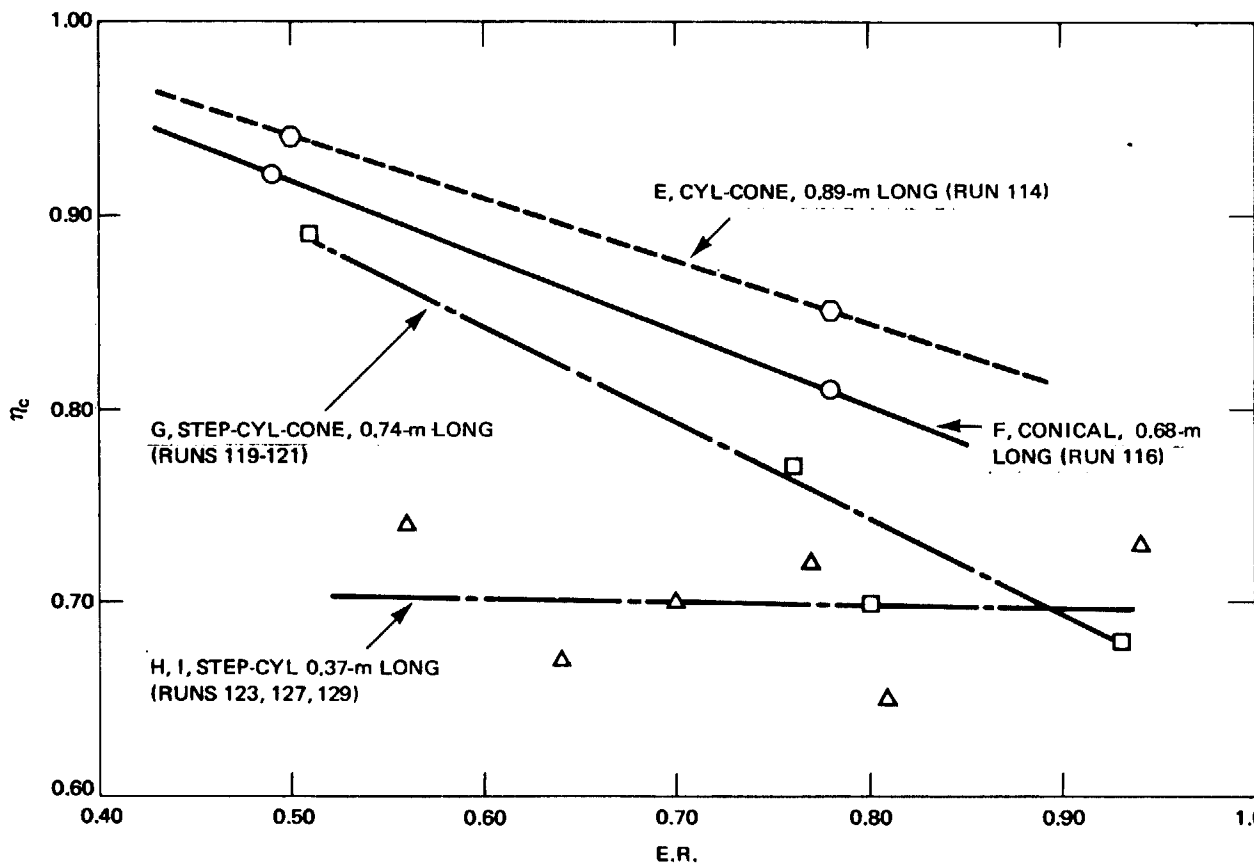

(C) FIG. 21 EFFECT OF COMBUSTOR GEOMETRY ON COMBUSTION EFFICIENCY WITH DISCRETE HOLE INJECTION (U)

SYM.	RUN	INJ.	ER	η_c	ER_{eff}
○	114	a	0.50	0.94	0.47
□	116	a	0.49	0.92	0.45
△	119	b	0.51	0.89	0.45
◇	123	b	0.56	0.74	0.41

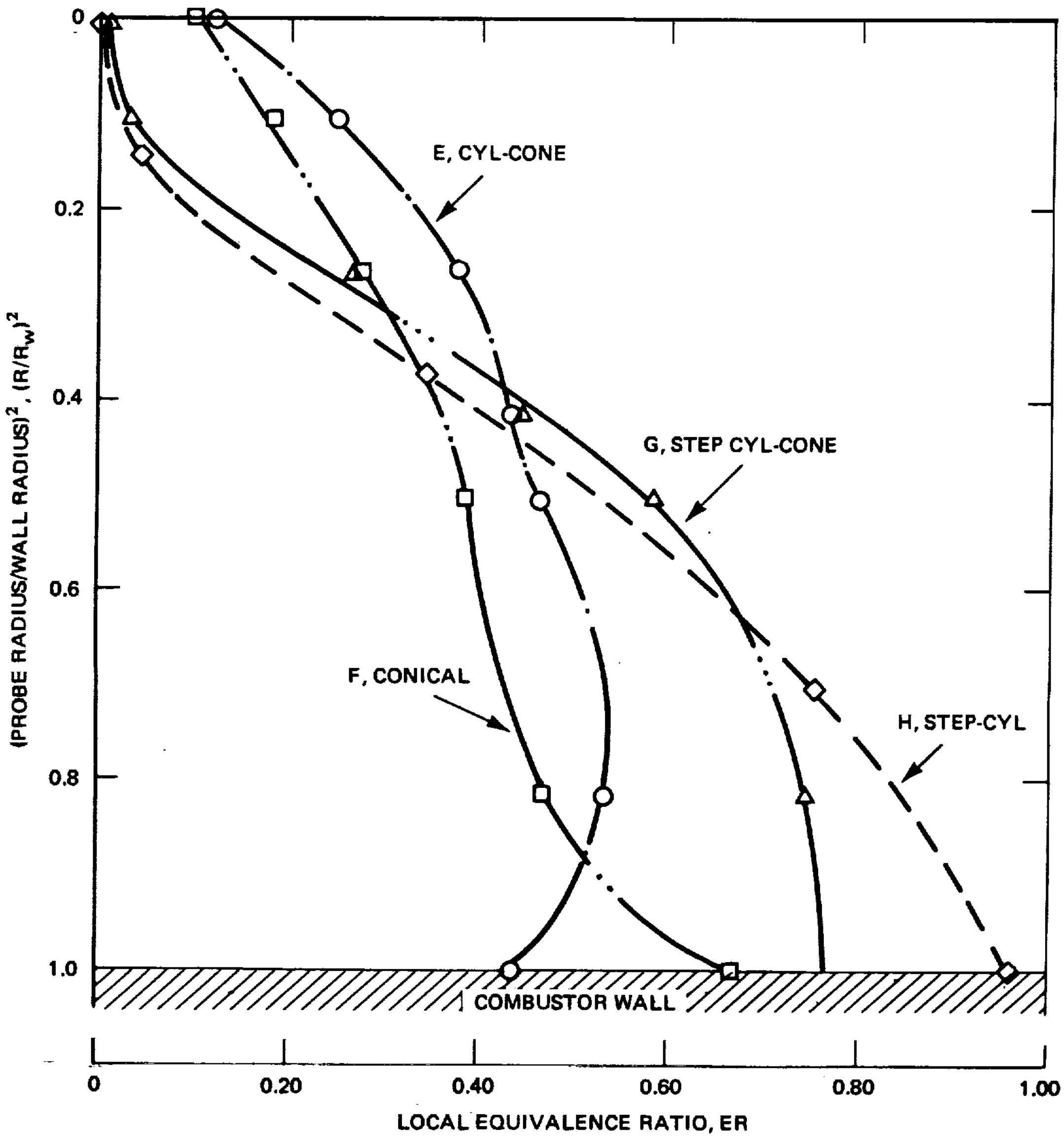

(C) FIGURE 22 RADIAL VARIATION OF ER IN EXIT PLANE OF FOUR COMBUSTOR GEOMETRIES. (U)

APPENDIX

(U) The Appendix contains all of the available basic data plots of combustor wall pressure ratio, combustor exit plane pitot pressure and combustor exit plane specie mole fraction and deduced ER distribution.

SYM.	RUN NO.	COMBUSTOR	INJECTOR	ER	η_c
○	78-1	A	c	0.31	0.93
□	78-2	A	c	0.60	0.82

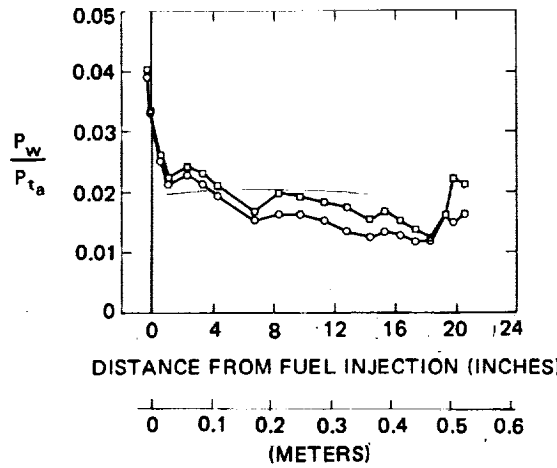

a) (C) COMBUSTOR WALL STATIC PRESSURE DISTRIBUTIONS FOR RUN 78. (U)

SYM.	RUN NO.	COMBUSTOR	INJECTOR	ER	η_c
○	79-1	A	c	0.42	0.72
□	79-2	A	c	0.20	0.95

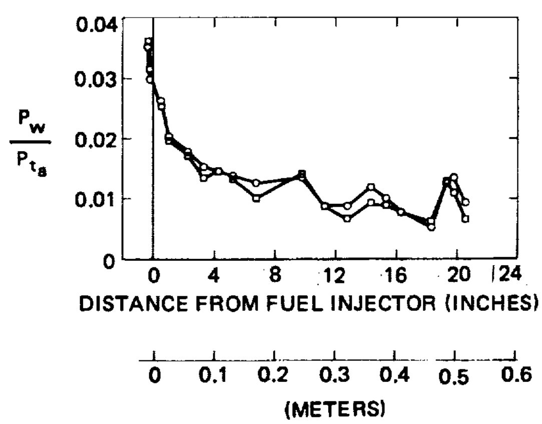

b) (C) COMBUSTOR WALL STATIC PRESURE DISTRIBUTIONS FOR RUN 79. (U)

Fig. A-1

SYM.	RUN NO.	COMBUSTOR	INJECTOR	ER	η_c
○	81-1	A	c	0.26	0.33
□	81-2	A	c	0.50	0.20
△	81-3	A	c	0.80	0.17

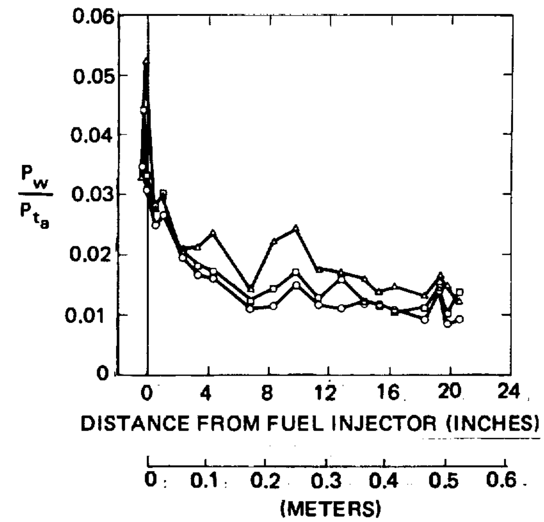

c) (C) COMBUSTOR WALL STATIC PRESSURE DISTRIBUTIONS FOR RUN 81. (U)

SYM.	RUN NO.	COMBUSTOR	INJECTOR	ER	η_c
□	82-1	A	c	0.50	0.20
○	82-2	A	c	0.80	0.15

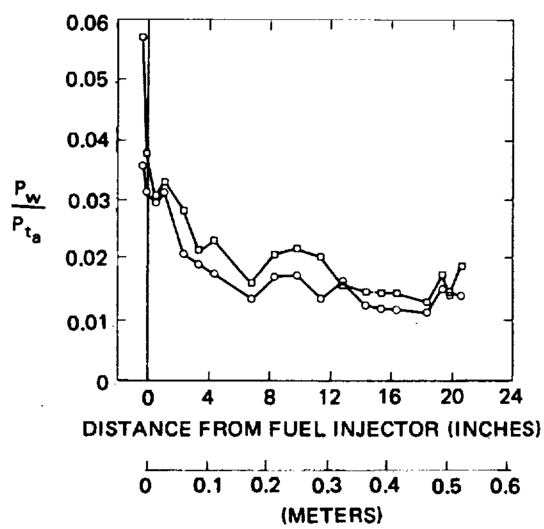

d) (C) COMBUSTOR WALL STATIC PRESSURE DISTRIBUTIONS FOR RUN 82. (U)

Fig. A-1 (cont'd)

SYM.	RUN NO.	COMBUSTOR	INJECTOR	ER	η_c
○	83-1	A	a	0.65	0.85
□	83-2	A	a	0.41	0.96
△	83-3	A	a	COLD POINT	

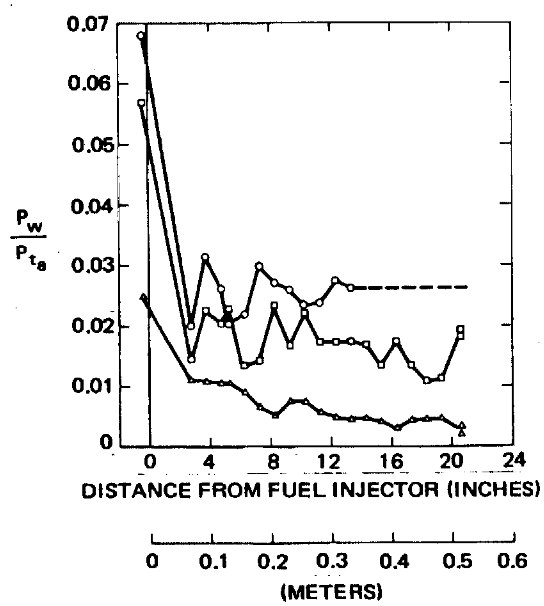

e) (C) COMBUSTOR WALL STATIC PRESSURE DISTRIBUTIONS FOR RUN 83. (U)

SYM.	RUN NO.	COMBUSTOR	INJECTOR	ER	η_c
○	84-1	A	a	0.92	0.80
□	84-2	A	a	0.57	0.92
△	84-3	A	a	COLD POINT	

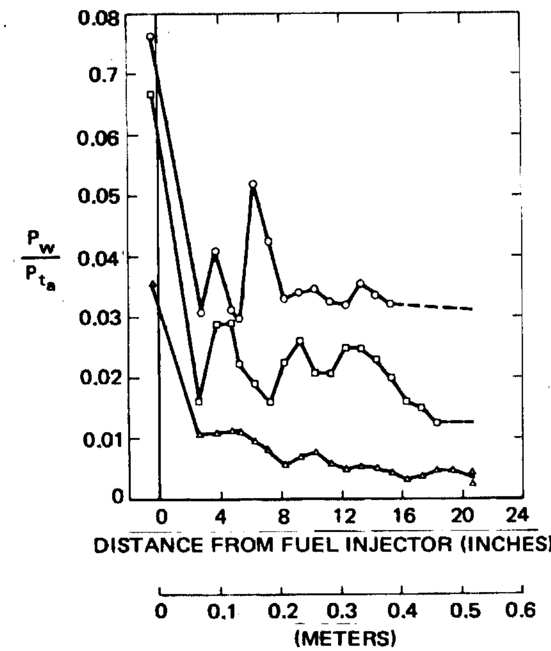

f) (C) COMBUSTOR WALL STATIC PRESSURE DISTRIBUTIONS FOR RUN 84. (U)

Fig. A-1 (cont'd)

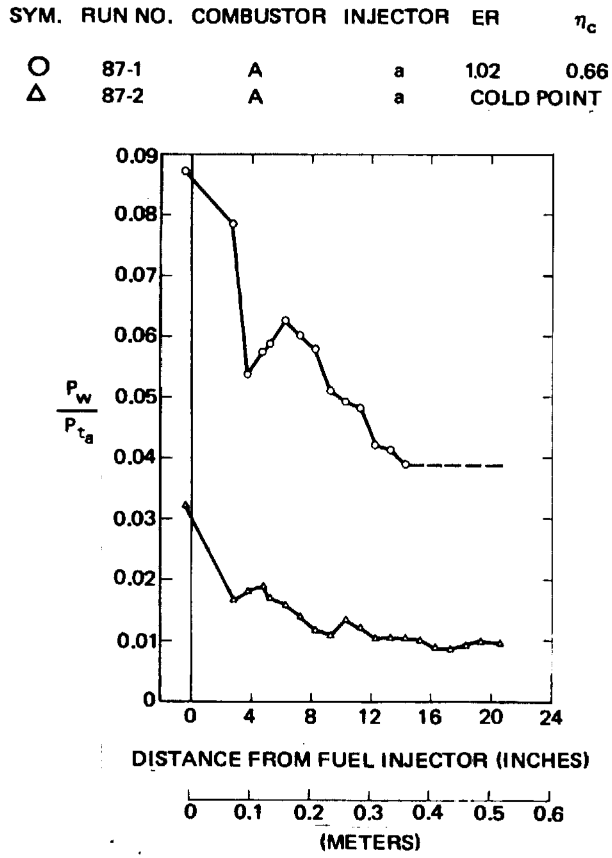

g) (C) COMBUSTOR WALL STATIC PRESSURE DISTRIBUTIONS FOR RUN 87. (U)

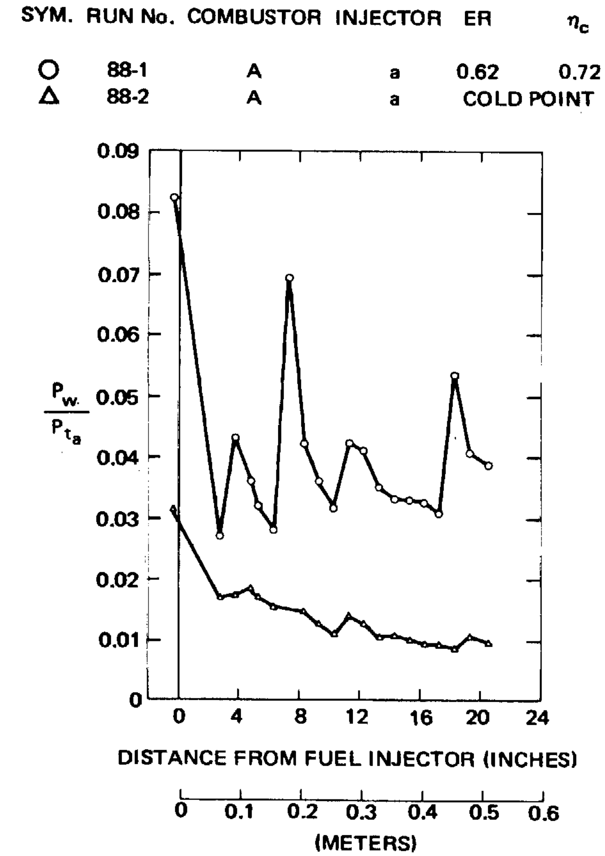

h) (C) COMBUSTOR WALL STATIC PRESSURE DISTRIBUTIONS FOR RUN 88. (U)

Fig. A-1 (cont'd)

SYM.	RUN NO.	COMBUSTOR	INJECTOR	ER	η_c
○	89-1	B	a	0.59	0.82
△	89-2	B	a	COLD POINT	

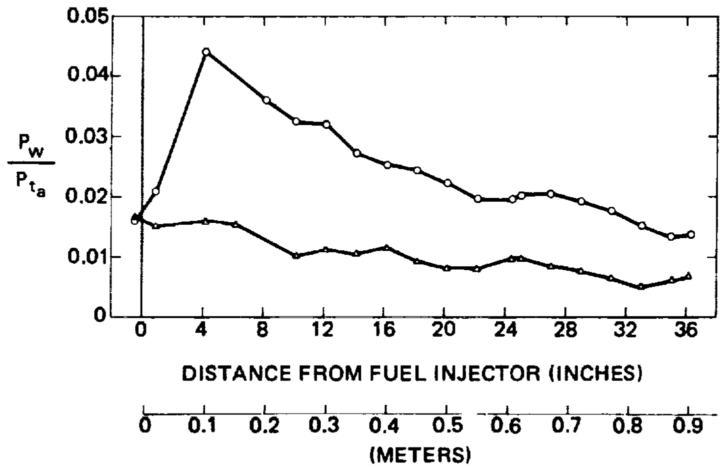

i) (C) COMBUSTOR WALL STATIC PRESSURE DISTRIBUTIONS FOR RUN 89. (U)

SYM.	RUN NO.	COMBUSTOR	INJECTOR	ER	η_c
□	98-27	D	d	0.79	0.65
○	98-31	D	d	0.50	0.84
△	96-20	D	d	COLD POINT	

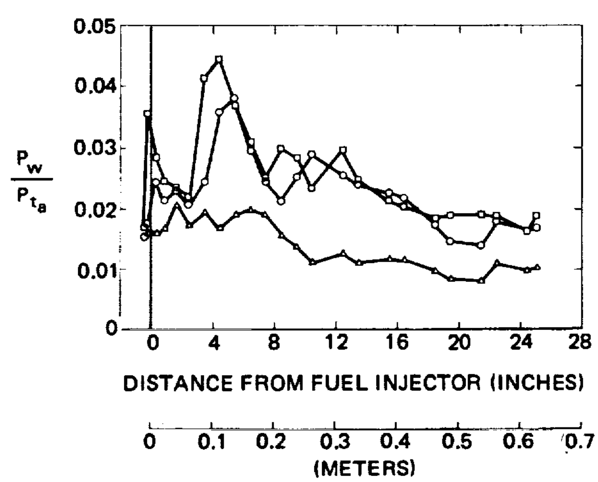

j) (C) COMBUSTOR WALL STATIC PRESSURE DISTRIBUTIONS FOR RUNS 96 AND 98. (U)

Fig. A-1 (cont'd)

SYM.	RUN NO.	COMBUSTOR	INJECTOR	ER	η_c
□	100-17	C	d	0.84	0.64
○	100-21	C	d	0.53	0.71
△	100-25	C	d	COLD POINT	

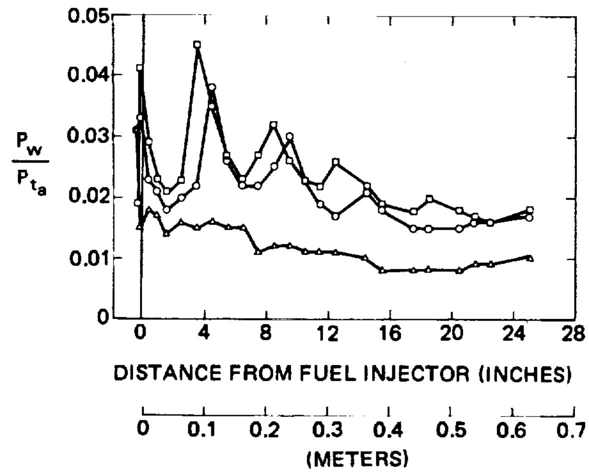

k) (C) COMBUSTOR WALL STATIC PRESSURE DISTRIBUTIONS FOR RUN 100. (U)

SYM.	RUN NO.	COMBUSTOR	INJECTOR	ER	η_c
□	102-17	C	d	0.83	0.55
○	102-21	C	d	0.52	0.72
△	102-25	C	d	COLD POINT	

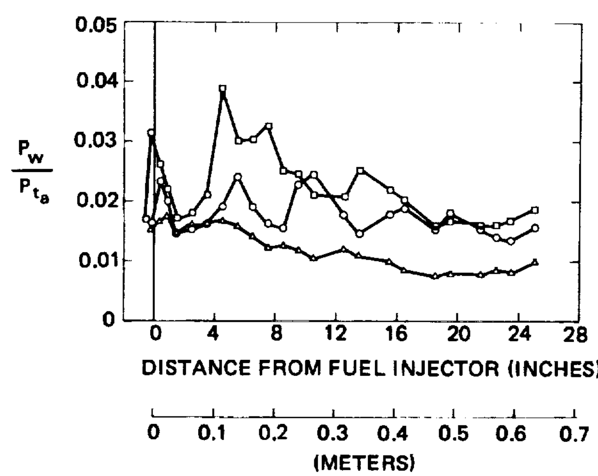

l) (C) COMBUSTOR WALL STATIC PRESSURE DISTRIBUTIONS FOR RUN 102. (U)

Fig. A-1 (cont'd)

SYM.	RUN NO.	COMBUSTOR	INJECTOR	ER	η_c
□	104-34	C	d	0.85	0.49
○	104-38	C	d	0.53	0.39
△	104-42	C	d	COLD POINT	

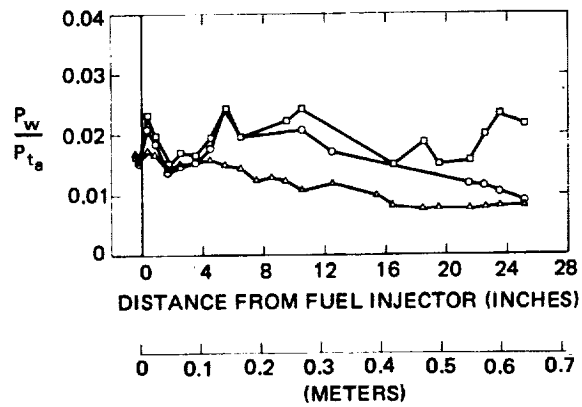

m) (C) COMBUSTOR WALL STATIC PRESSURE DISTRIBUTIONS FOR RUN 104. (U)

SYM.	RUN NO.	COMBUSTOR	INJECTOR	ER	η_c
□	106-18	D	d	0.81	0.52
○	106-23	D	d	0.51	0.43
△	106-27	D	d	COLD POINT	

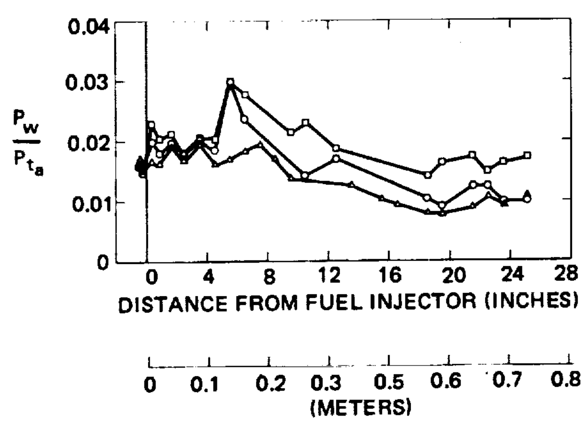

n) (C) COMBUSTOR WALL STATIC PRESSURE DISTRIBUTIONS FOR RUN 106. (U)

Fig. A-1 (cont'd)

SYM.	RUN NO.	COMBUSTOR	INJECTOR	ER	η_c
□	108-29	D	a	0.80	0.72
△	108-27	D	a	COLD POINT	

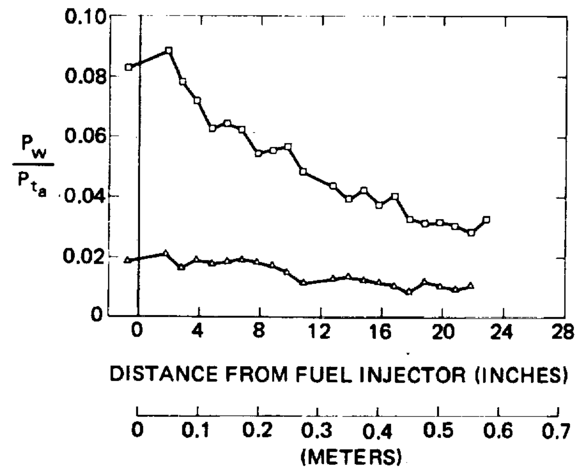

o) (C) COMBUSTOR WALL STATIC PRESSURE DISTRIBUTIONS FOR RUN 108. (U)

SYM.	RUN NO.	COMBUSTOR	INJECTOR	ER	η_c
□	110-28	D	a	0.83	0.74
○	110-33	D	a	0.52	0.84
△	110-37	D	a	COLD POINT	

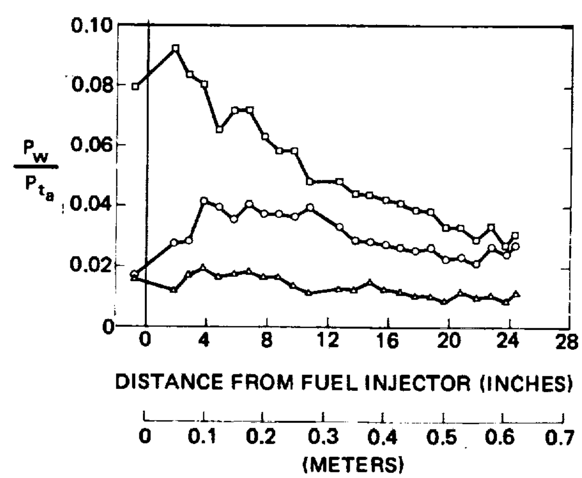

p) (C) COMBUSTOR WALL STATIC PRESSURE DISTRIBUTIONS FOR RUN 110. (U)
Fig. A-1 (cont'd)

SYM.	RUN NO.	COMBUSTOR	INJECTOR	ER	η_c
□	112-26	E	d	0.79	0.61
○	112-31	E	d	0.50	0.75
△	112-35	E	d	COLD POINT	

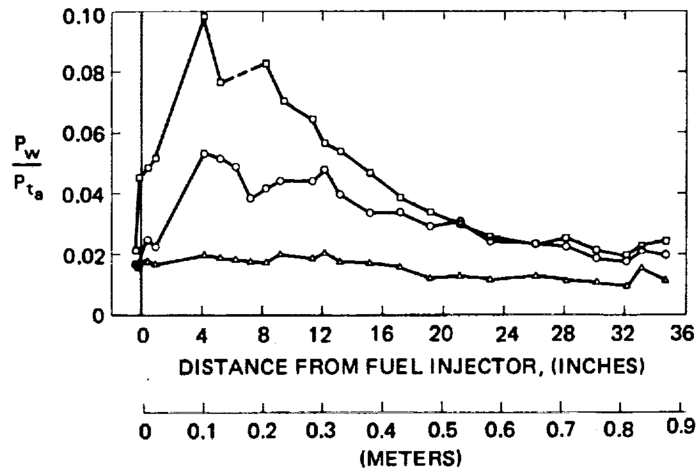

q) (C) COMBUSTOR WALL STATIC PRESSURE DISTRIBUTIONS FOR RUN 112. (U)

SYM.	RUN NO.	COMBUSTOR	INJECTOR	ER	η_c
□	114-15	E	a	0.78	0.85
○	114-20	E	a	0.50	0.94
△	114-24	E	a	COLD POINT	

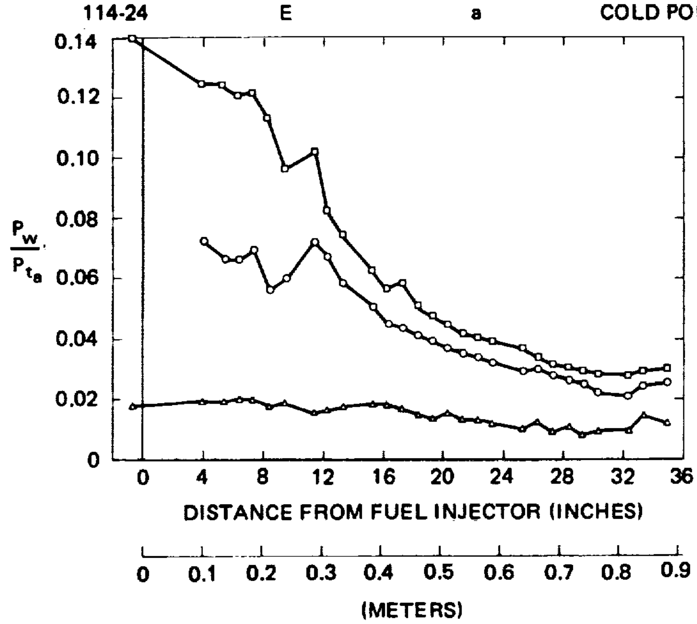

r) (C) COMBUSTOR WALL STATIC PRESSURE DISTRIBUTIONS FOR RUN 114. (U)
Fig. A-1 (cont'd)

SYM.	RUN NO.	COMBUSTOR	INJECTOR	ER	η_c
○	116-16	F	a	0.78	0.81
□	116-21	F	a	0.49	0.92
△	116-24	F	a	COLD POINT	

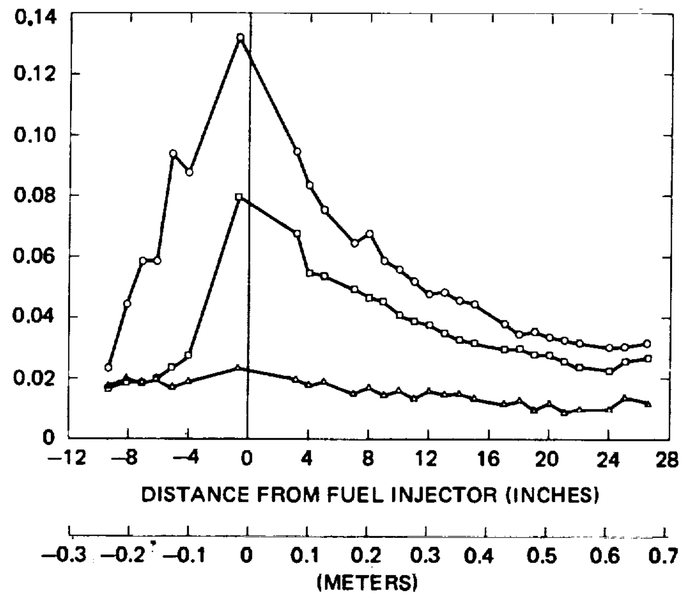

s) (C) COMBUSTOR WALL STATIC PRESSURE DISTRIBUTIONS FOR RUN 116. (U)

SYM.	RUN NO.	COMBUSTOR	INJECTOR	ER	η_c
□	119-58	F	b	0.80	0.71
○	119-62	F	b	0.51	0.88
△	119-67	F	b	COLD POINT	

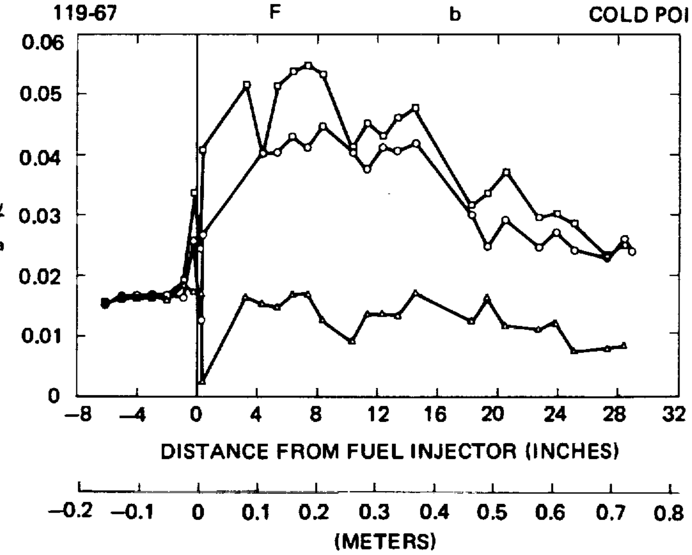

t) (C) COMBUSTOR WALL STATIC PRESSURE DISTRIBUTIONS FOR RUN 119. (U)

Fig. A-1 (cont'd)

SYM.	RUN NO.	COMBUSTOR	INJECTOR	ER	η_c
□	121-55	G	b	0.93	0.69
○	121-58	G	b	0.69	0.87
△	121-63	G	b	COLD POINT	

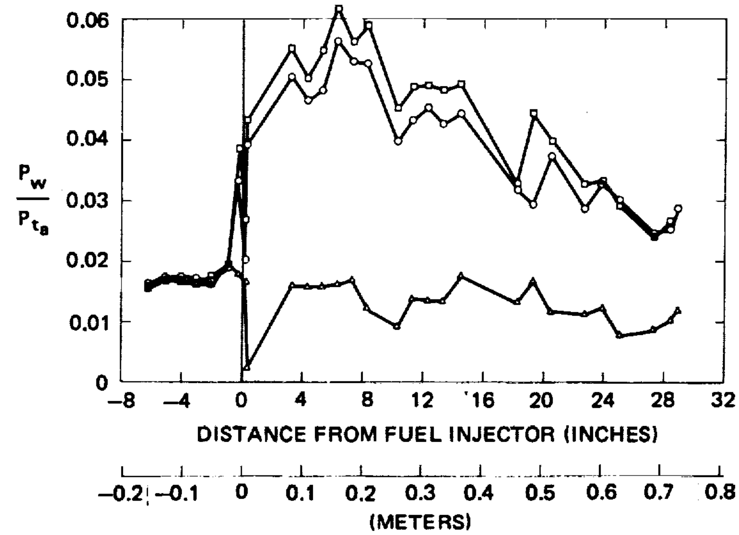

u) (C) COMBUSTOR WALL STATIC PRESSURE DISTRIBUTIONS FOR RUN 121. (U)

SYM.	RUN NO.	COMBUSTOR	INJECTOR	ER	η_c
□	123-3	H	b	0.70	0.68
○	123-5	H	b	0.50	0.73
△	123-7	H	b	COLD POINT	

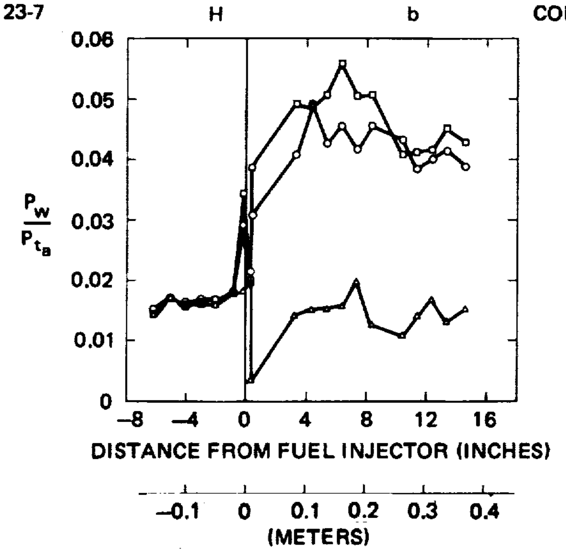

v) (C) COMBUSTOR WALL STATIC PRESSURE DISTRIBUTIONS FOR RUN 123. (U)

Fig. A-1 (cont'd)

SYM.	RUN NO.	COMBUSTOR	INJECTOR	ER	η_c
□	127-64	I	b	0.94	0.73
○	127-68	I	b	0.77	0.72
△	127-72	I	b	COLD POINT	

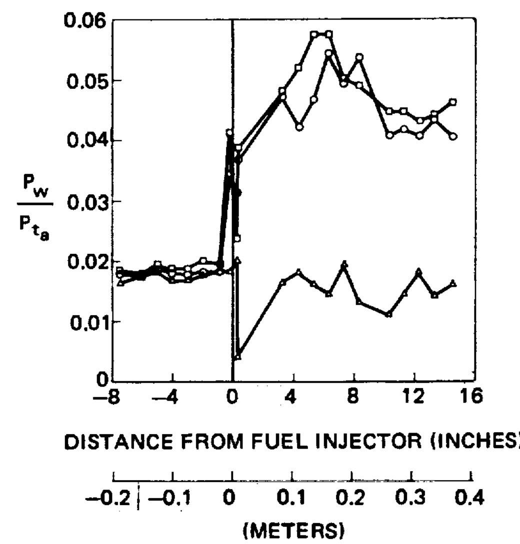

w) (C) COMBUSTOR WALL STATIC PRESSURE DISTRIBUTIONS FOR RUN 127. (U)

Fig. A-1 (concluded)

SYM.	RUN NO.	COMBUSTOR	INJECTOR	P_{t_a} (PSIA)	ER	η_c
○	78-1	A	c	460	0.31	0.93
□	78-2	A	c	460	0.60	0.82

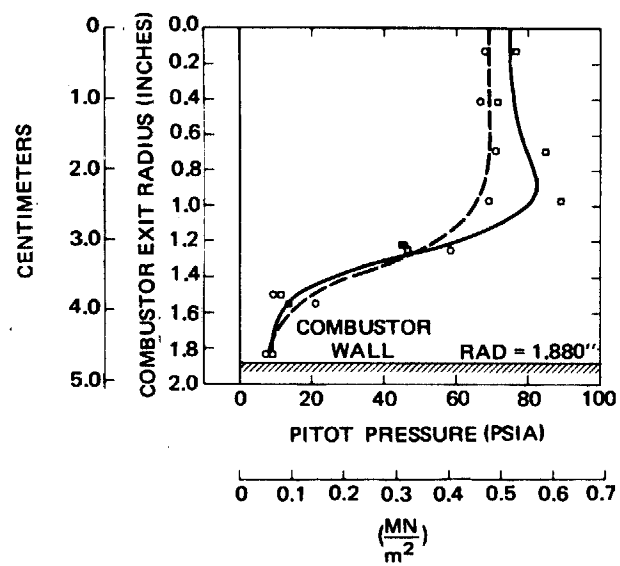

a) (C) RADIAL VARIATION OF PITOT PRESSURE IN COMBUSTOR EXIT PLANE FOR RUN 78. (U)

SYM.	RUN NO.	COMBUSTOR	INJECTOR	P_{t_a} (PSIA)	ER	η_c
—○	79-1	A	c	433	0.42	0.72
---□	79-2	A	c	424	0.20	0.95

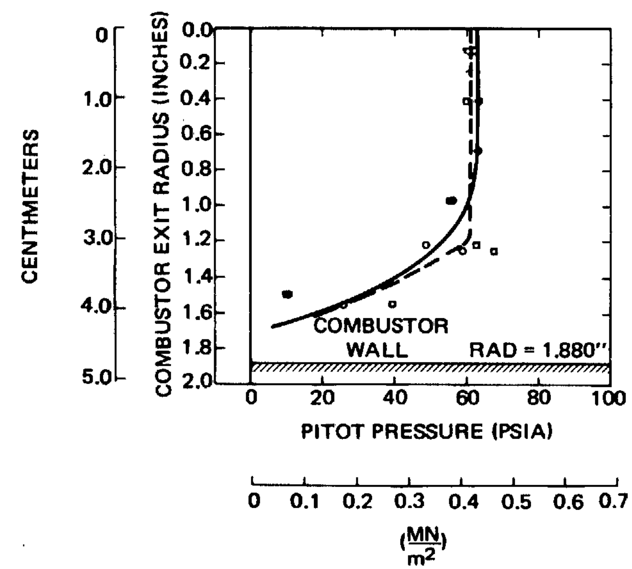

b) (C) RADIAL VARIATION OF PITOT PRESSURE IN COMBUSTOR EXIT PLANE FOR RUN 79. (U)

Fig. A-2

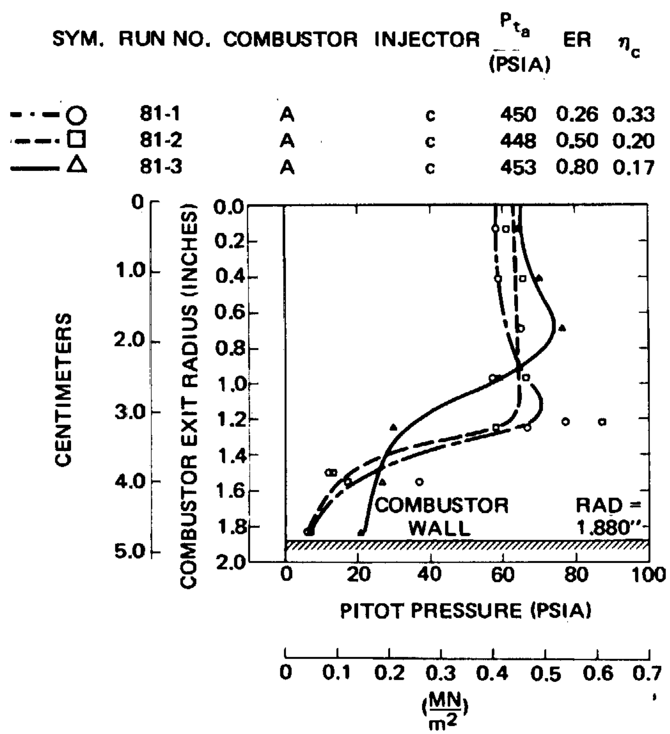

c) (C) RADIAL VARIATION OF PITOT PRESSURE IN COMBUSTOR EXIT PLANE FOR RUN 81. (U)

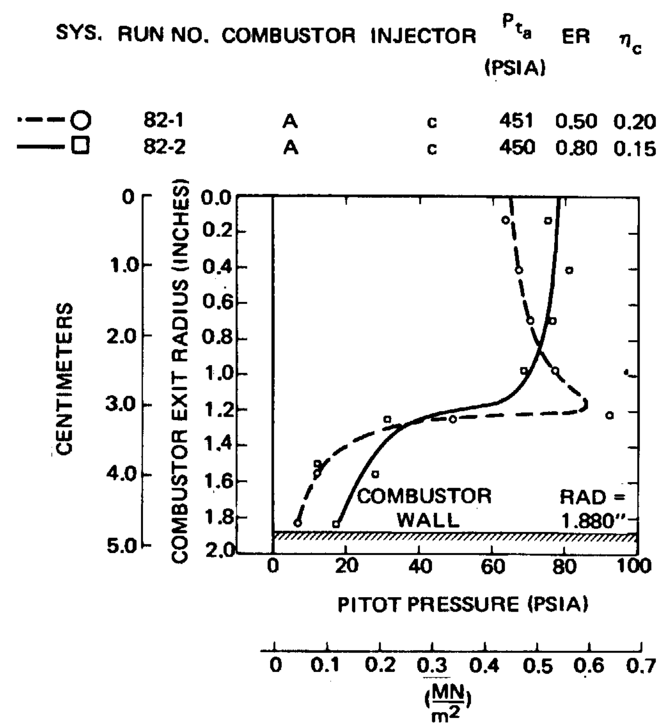

d) (C) RADIAL VARIATION OF PITOT PRESSURE IN COMBUSTOR EXIT PLANE FOR RUN 82. (U)

Fig. A-2 (cont'd)

SYM.	RUN NO.	COMBUSTOR	INJECTOR	P_{t_a} (PSIA)	ER	η_c
—□	83-1	A	a	424	0.65	0.85
- - -○	83-2	A	a	422	0.41	0.96
-·-△	83-3	A	a	413	COLD POINT	

SYM.	RUN NO.	COMBUSTOR	INJECTOR	P_{t_a} (PSIA)	ER	η_c
—○	84-1	A	a	427	0.92	0.80
- - -□	84-2	A	a	431	0.57	0.92
-·-△	84-3	A	a	436	COLD POINT	

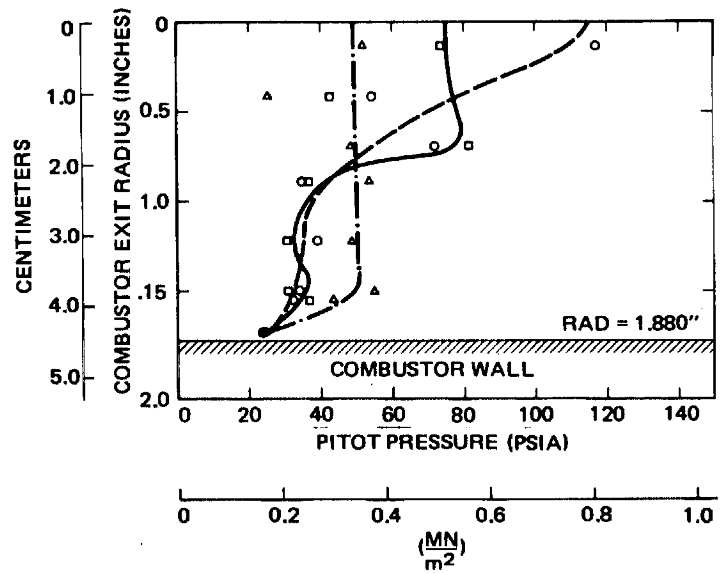

e) (C) RADIAL VARIATION OF PITOT PRESSURE IN COMBUSTOR EXIT PLANE FOR RUN 83. (U)

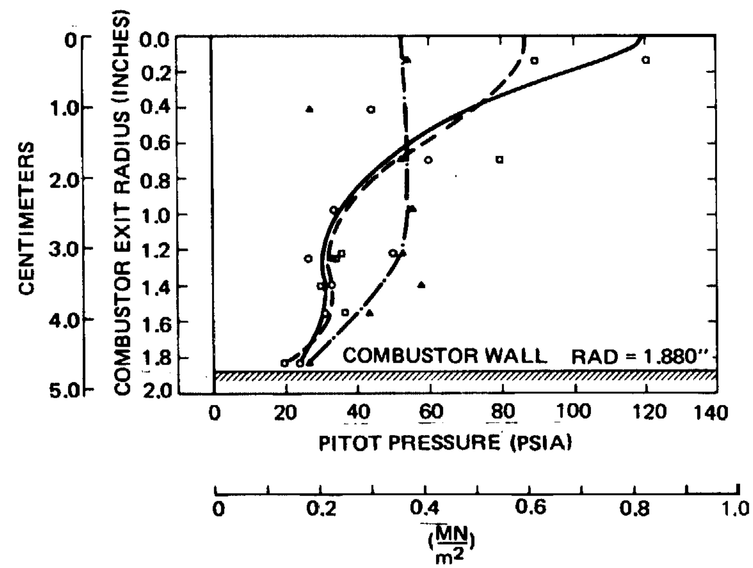

f) (C) RADIAL VARIATION OF PITOT PRESSURE IN COMBUSTOR EXIT PLANE FOR RUN 84. (U)

Fig. A-2 (cont'd)

SYM.	RUN NO.	COMBUSTOR	INJECTOR	P_{t_a} (PSIA)	ER	η_c
○	87-1	A	a	400	1.02	0.66
△	87-2	A	a	397	COLD POINT	

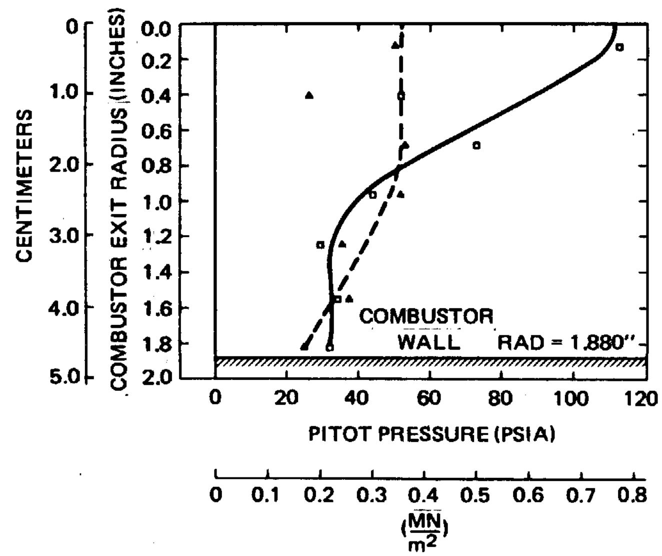

g) (C) RADIAL VARIATION OF PITOT PRESSURE IN COMBUSTOR EXIT PLANE FOR RUN 87. (U)

SYM.	RUN NO.	COMBUSTOR	INJECTOR	P_{t_a} (PSIA)	ER	η_c
○	88-1	A	a	399	0.62	0.72
△	88-2	A	a	401	COLD POINT	

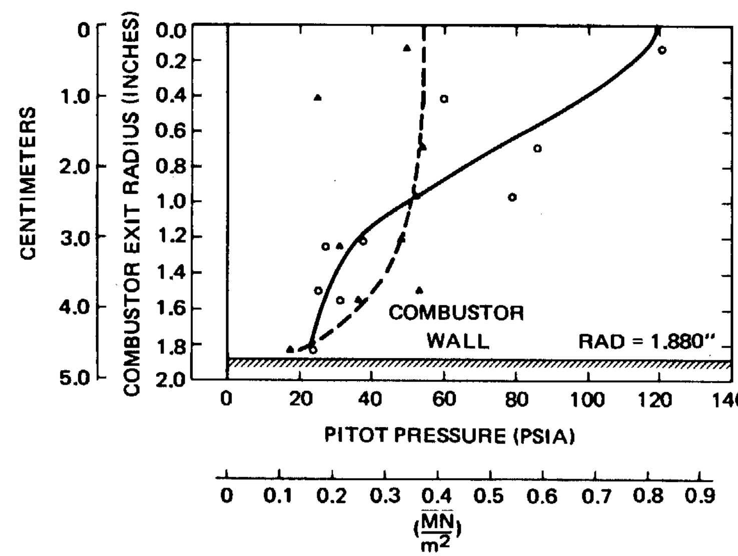

h) (C) RADIAL VARIATION OF PITOT PRESSURE IN COMBUSTOR EXIT PLANE FOR RUN 88. (U)

Fig. A-2 (cont'd)

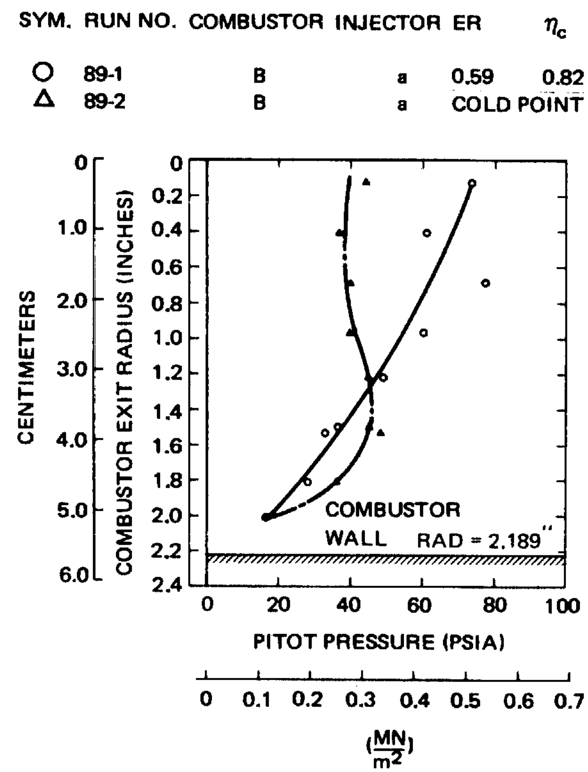

i) (C) RADIAL VARIATION OF PITOT PRESSURE IN COMBUSTOR EXIT PLANE FOR RUN 89.(U)

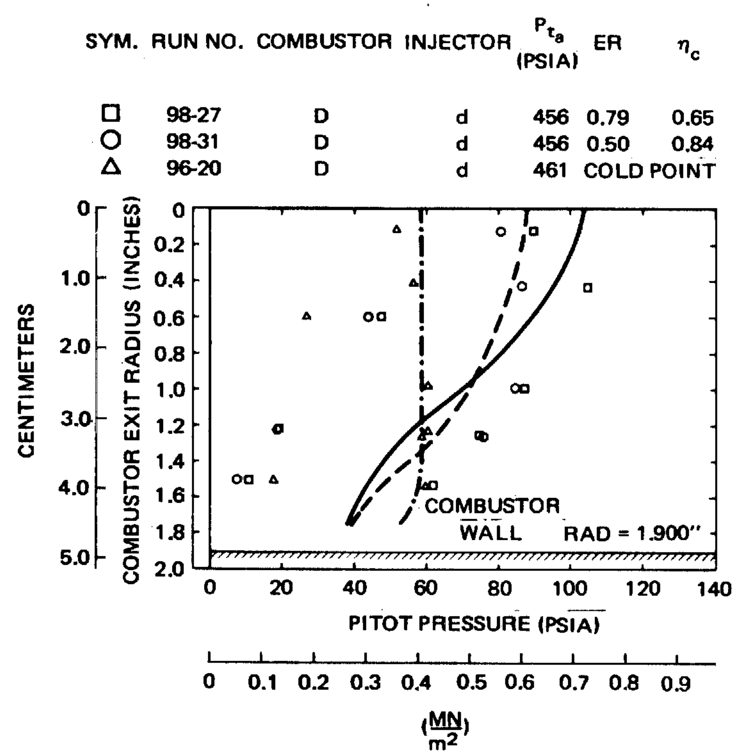

j) (C) RADIAL VARIATION OF PITOT PRESSURE IN COMBUSTOR EXIT PLANE FOR RUN 98. (U)

Fig. A-2 (cont'd)

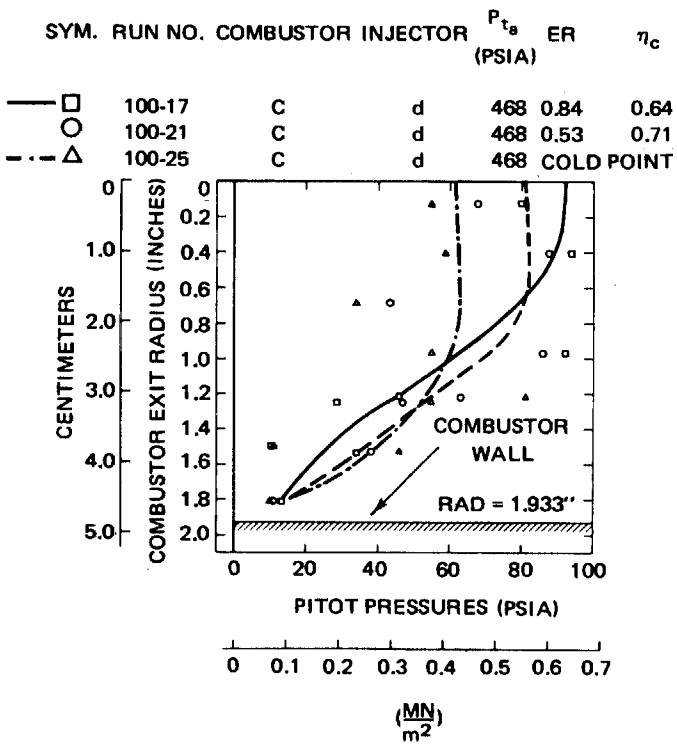

k) (C) RADIAL VARIATION OF PITOT PRESSURE IN COMBUSTOR EXIT PLANE FOR RUN 100. (U)

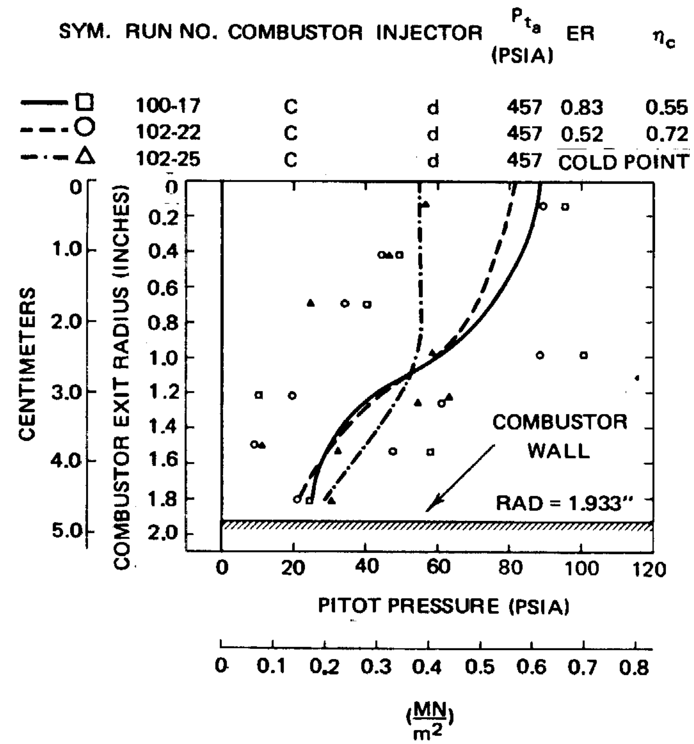

l) (C) RADIAL VARIATION OF PITOT PRESSURE IN COMBUSTOR EXIT PLANE FOR RUN 102. (U)

Fig. A-2 (cont'd)

SYM.	RUN NO.	COMBUSTOR	INJECTOR	P_{t_a} (PSIA)	ER	η_c
—□	104-34	C	d	455	0.85	0.49
- - -○	104-38	C	d	455	0.53	0.39
—·—△	104-42	C	d	455	COLD POINT	

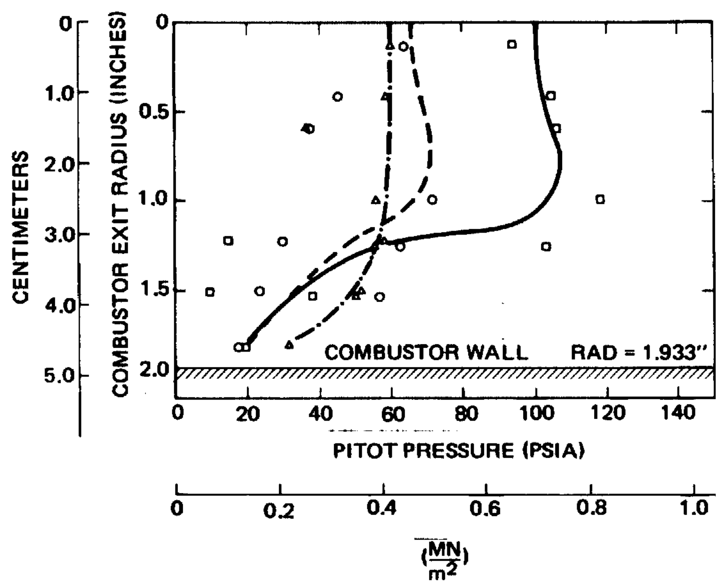

m) (C) RADIAL VARIATION OF PITOT PRESSURE IN COMBUSTOR EXIT PLANE FOR RUN 104. (U)

SYM.	RUN NO.	COMBUSTOR	INJECTOR	P_{t_a} (PSIA)	ER	η_c
—□	106-18	D	d	456	0.81	0.52
- - -○	106-23	D	d	456	0.51	0.43
—·—△	106-27	D	d	456	COLD POINT	

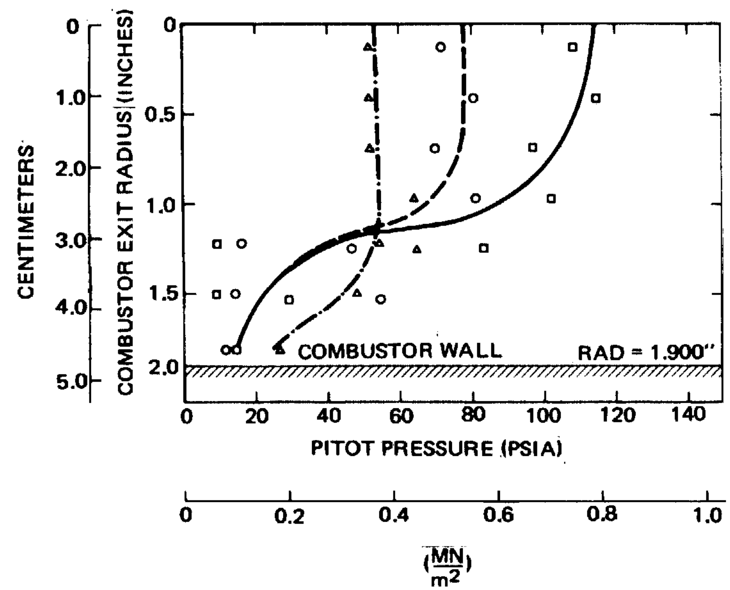

n) (C) RADIAL VARIATION OF PITOT PRESSURE IN COMBUSTOR EXIT PLANE FOR RUN 106. (U)

Fig. A-2 (cont'd)

SYM'	RUN NO.	COMBUSTOR	INJECTOR	P_{t_a} (PSIA)	ER	η_c
—□	108-29	D	a	449	0.80	0.72
--○	108-33	D	a	449	0.51	0.82
-·-△	108-37	D	a	449	COLD POINT	

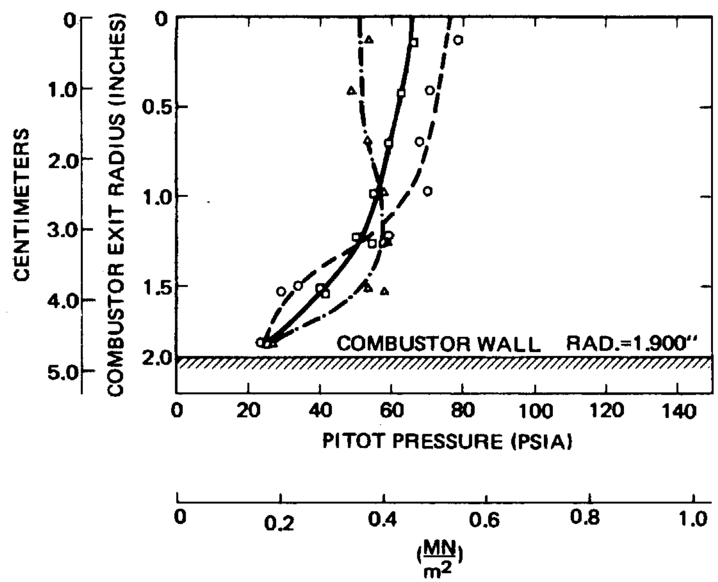

o) (C) RADIAL VARIATION OF PITOT PRESSURE IN COMBUSTOR EXIT PLANE FOR RUN 108. (U)

SYM.	RUN NO.	COMBUSTOR	INJECTOR	P_{t_a} (PSIA)	ER	η_c
—□	110-28	D	a	455	0.83	0.74
--○	110-33	D	a	455	0.52	0.84
-·-△	110-37	D	a	455	COLD POINT	

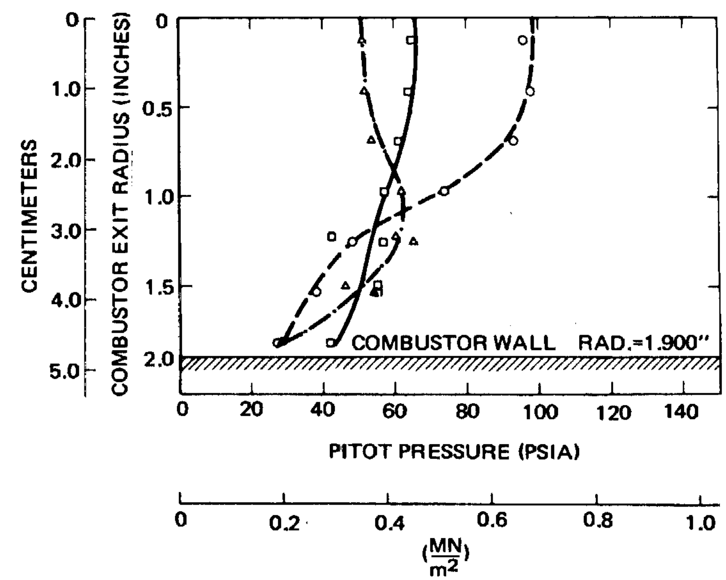

p) (C) RADIAL VARIATION OF PITOT PRESSURE IN COMBUSTOR EXIT PLANE FOR RUN 110. (U)

Fig. A-2 (cont'd)

SYM.	RUN NO.	COMBUSTOR	INJECTOR	P_{t_a} (PSIA)	ER	η_c
—□	112-16	E	d	465	0.79	0.61
- - -○	112-31	E	d	465	0.50	0.75
-·-△	112-35	E	d	465	COLD POINT	

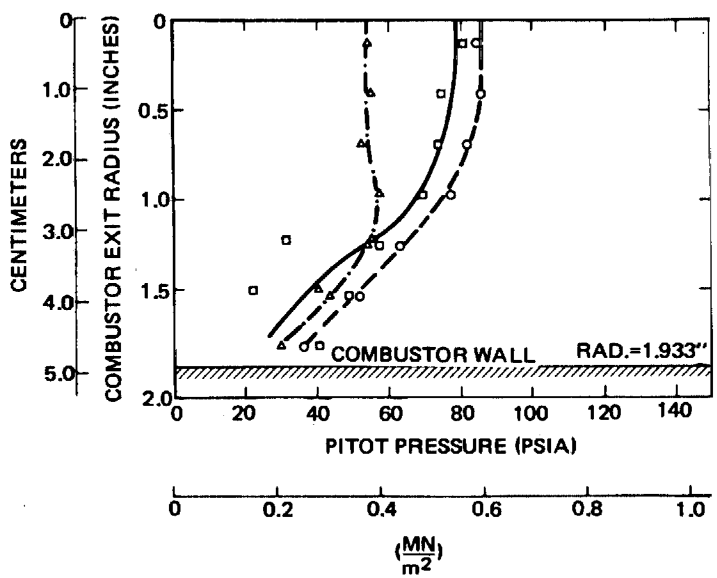

q) (C) RADIAL VARIATION OF PITOT PRESSURE IN COMBUSTOR EXIT PLANE FOR RUN 112. (U)

SYM.	RUN NO.	COMBUSTOR	INJECTOR	P_{t_a} (PSIA)	ER	η_c
—□	114-15	E	a	454	0.78	0.85
- - -○	114-20	E	a	454	0.50	0.94
-·-△	114-24	E	a	454	COLD POINT	

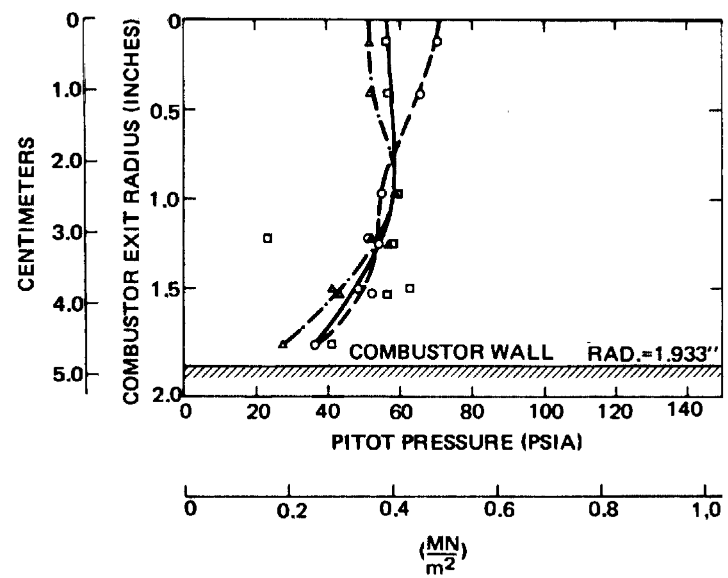

r) (C) RADIAL VARIATION OF PITOT PRESSURE IN COMBUSTOR EXIT PLANE FOR RUN 114. (U)

Fig. A-2 (cont'd)

SYM.	RUN NO.	COMBUSTOR	INJECTOR	P_{t_a} (PSIA)	ER	η_c
—□	116-16	F	a	456	0.78	0.81
---○	116-21	F	a	456	0.49	0.92
-·-△	116-24	F	a	456	COLD POINT	

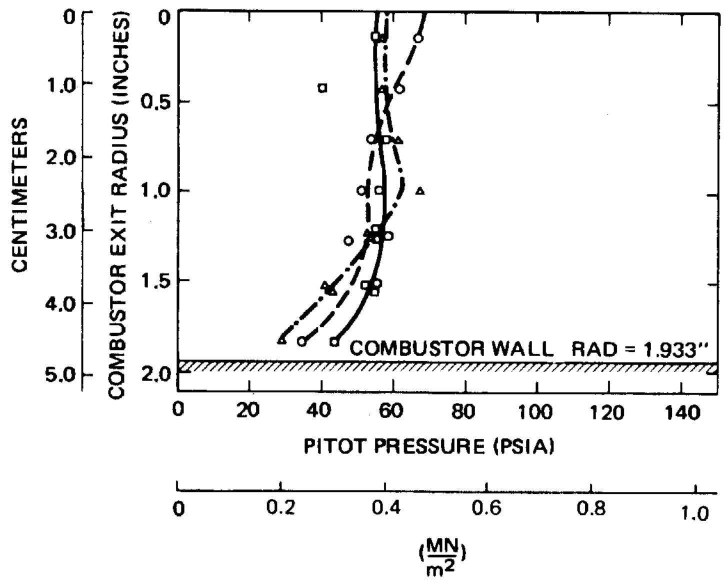

s) (C) RADIAL VARIATION OF PITOT PRESSURE IN COMBUSTOR EXIT PLANE FOR RUN 116. (U)

SYM.	RUN NO.	COMBUSTOR	INJECTOR	P_{t_a} (PSIA)	ER	η_c
—□	119-58	G	b	450	0.80	0.70
---○	119-62	G	b	450	0.51	0.89
-·-△	119-67	G	b	450	COLD POINT	

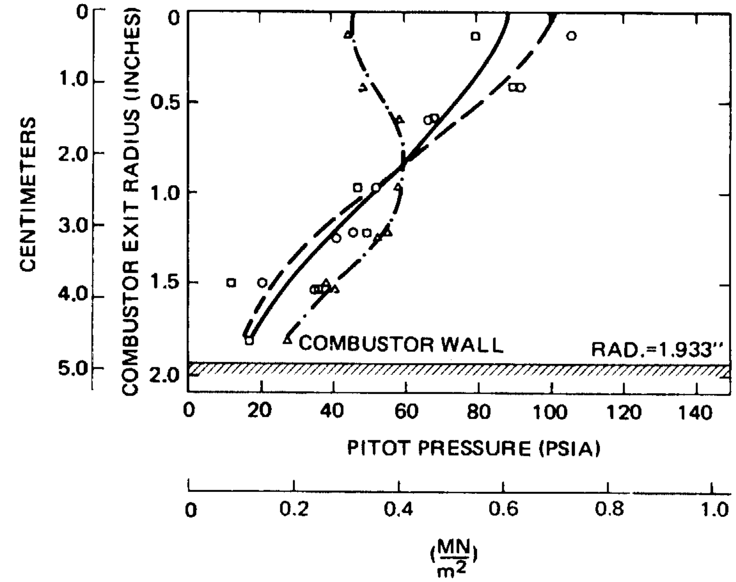

t) (C) RADIAL VARIATION OF PITOT PRESSURE IN COMBUSTOR EXIT PLANE FOR RUN 119. (U)

Fig. A-2 (cont'd)

SYM.	RUN NO.	COMBUSTOR	INJECTOR	P_{t_a} (PSIA)	ER	η_c
—□	121-55	G	b	446	0.93	0.68
---○	121-58	G	b	446	0.76	0.77
—·—△	121-63	G	b	446	COLD POINT	

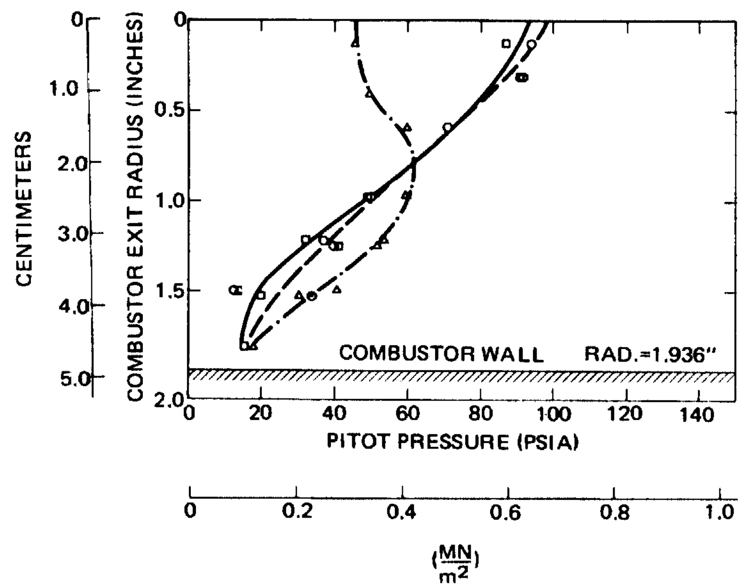

u) (C) RADIAL VARIATION OF PITOT PRESSURE IN COMBUSTOR EXIT PLANE FOR RUN 121. (U)

SYM.	RUN NO.	COMBUSTOR	INJECTOR	P_{t_a} (PSIA)	ER	η_c
—□	123-3	H	b	446	0.70	0.70
---○	123-5	H	b	446	0.56	0.74
—·—△	123-7	H	b	446	COLD POINT	

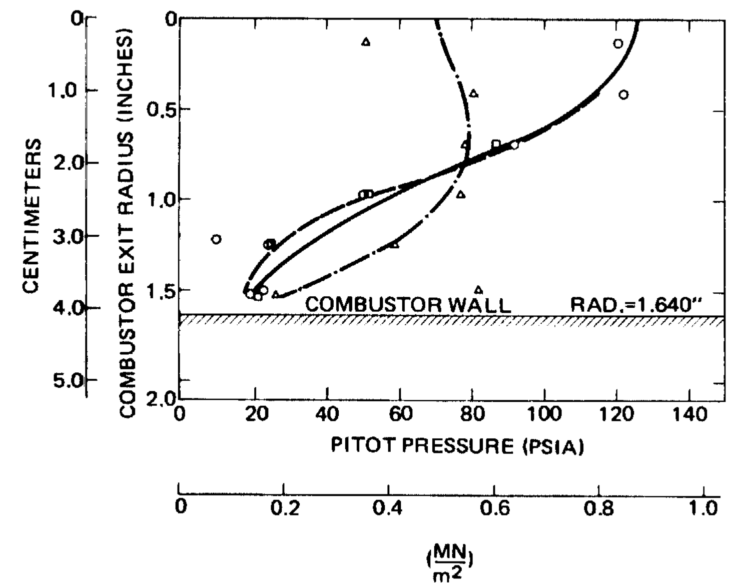

v) (C) RADIAL VARIATION OF PITOT PRESSURE IN COMBUSTOR EXIT PLANE FOR RUN 123. (U)

Fig. A-2 (cont'd)

SYM.	RUN NO.	COMBUSTOR	INJECTOR	P_{t_a} (PSIA)	ER	η_c
—□	127-64	I	b	460	0.94	0.73
‑‑‑○	127-68	I	b	460	0.77	0.72
‑·‑△	127-72	I	b	460	COLD POINT	

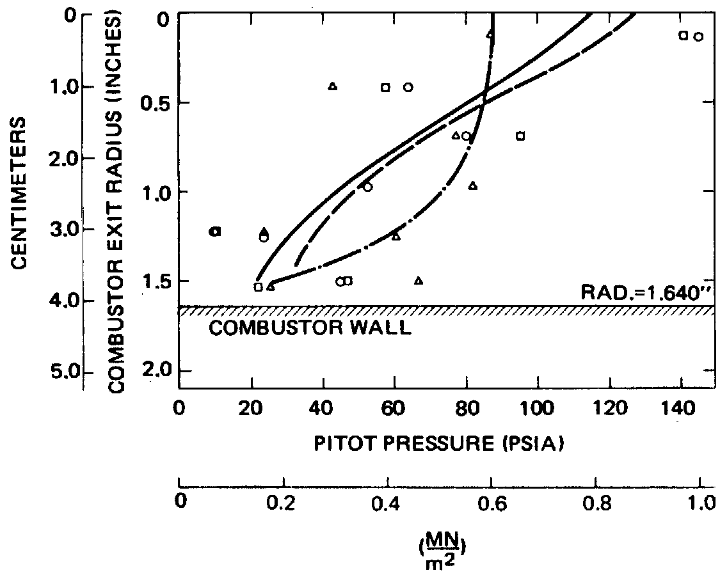

w) (C) RADIAL VARIATION OF PITOT PRESSURE IN COMBUSTOR EXIT PLANE FOR RUN 127. (U)

SYM.	RUN NO.	COMBUSTOR	INJECTOR	ER	η_c
—□	129-1	I	b	0.81	0.65
‑‑‑○	129-2	I	b	0.64	0.67
‑·‑△	129-3	I	b	COLD POINT	

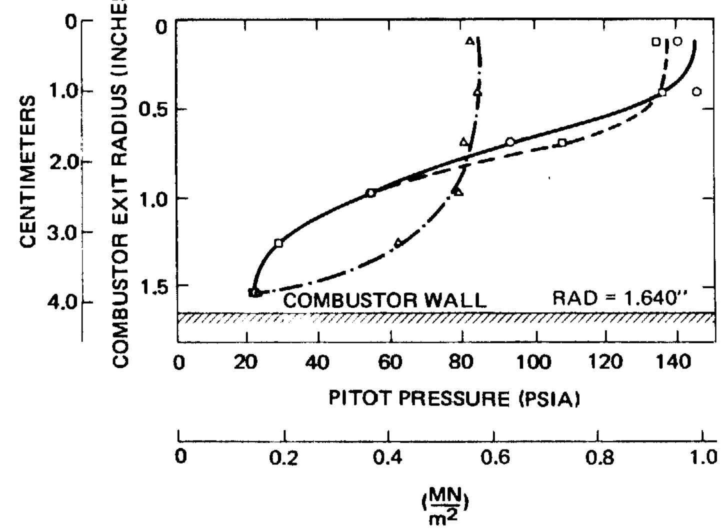

x) (C) RADIAL VARIATION OF PITOT PRESSURE IN COMBUSTOR EXIT PLANE FOR RUN 129. (U)

Fig. A-2 (concluded)

GAS SAMPLE DATA

RUN NO.	COMB.	INJ.	ER	η_c
83-1	A	a	0.65	0.85

OPEN SYMBOLS – ALIGNED WITH PORTS
SOLID SYMBOLS – BETWEEN PORTS

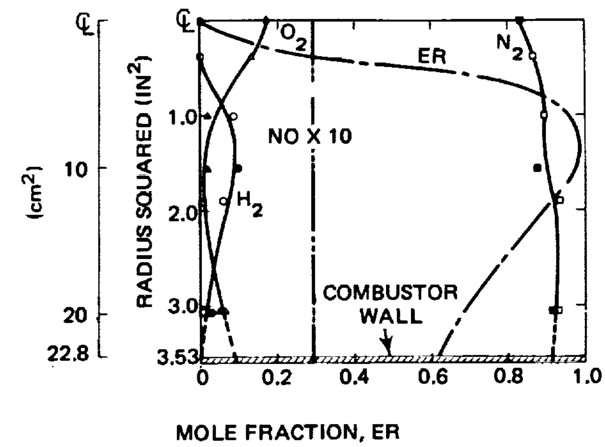

a) (C) RADIAL VARIATION OF SPECIE MOLE FRACTION AND DEDUCED ER IN COMBUSTOR EXIT PLANE. (U)

GAS SAMPLE DATA

RUN NO.	COMB.	INJ.	ER	η_c
84-1	A	a	0.92	0.80

OPEN SYMBOLS – ALIGNED WITH PORTS
SOLID SYMBOLS – BETWEEN PORTS

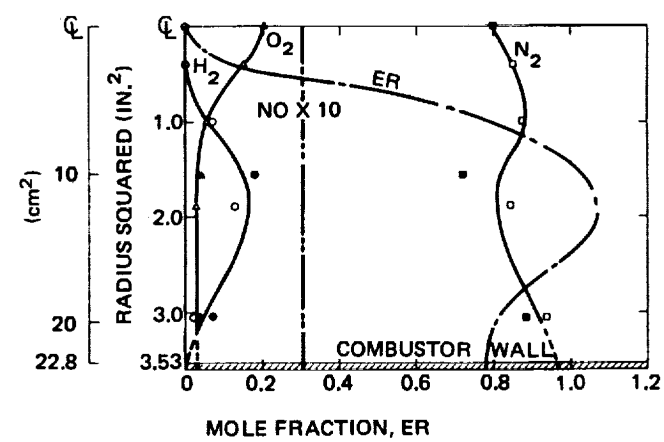

b) (C) RADIAL VARIATION OF SPECIE MOLE FRACTION AND DEDUCED ER IN COMBUSTOR EXIT PLANE. (U)

(C) Fig. A-3

GAS SAMPLE DATA

RUN NO.	COMB.	INJ.	ER	η_c
84-2	A	a	0.57	0.92

OPEN SYMBOLS – ALIGNED WITH PORTS
SOLID SYMBOLS – BETWEEN PORTS

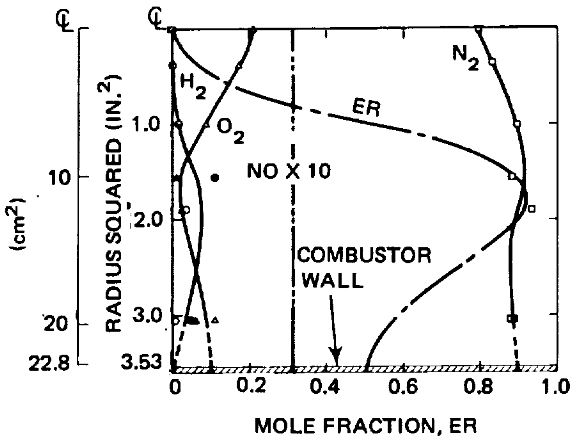

c) (C) RADIAL VARIATION OF SPECIE MOLE FRACTION AND DEDUCED ER IN COMBUSTOR EXIT PLANE. (U)

GAS SAMPLE DATA

RUN NO.	COMB.	INJ.	ER	η_c
87-1	A	a	1.02	0.66

OPEN SYMBOLS – ALIGNED WITH PORTS
SOLID SYMBOLS – BETWEEN PORTS

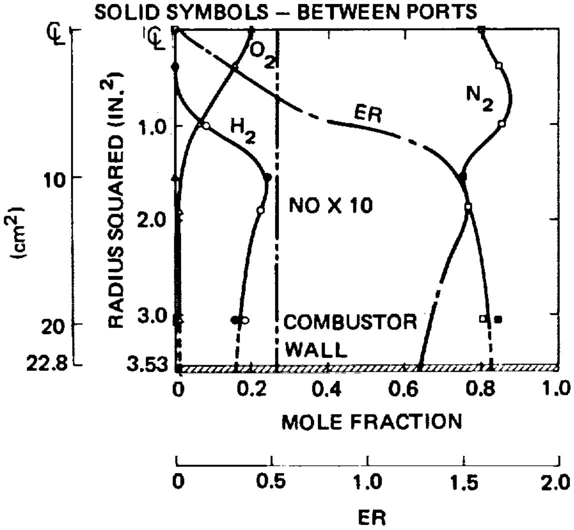

d) (C) RADIAL VARIATION OF SPECIE MOLE FRACTION AND DEDUCED ER IN COMBUSTOR EXIT PLANE. (U)

(C) Fig A-3 (cont'd)

GAS SAMPLE DATA

RUN NO.	COMB.	INJ.	ER	η_c
89-1	B	a	0.59	0.82

OPEN SYMBOLS – ALIGNED WITH PORTS
SOLID SYMBOLS – BETWEEN PORTS

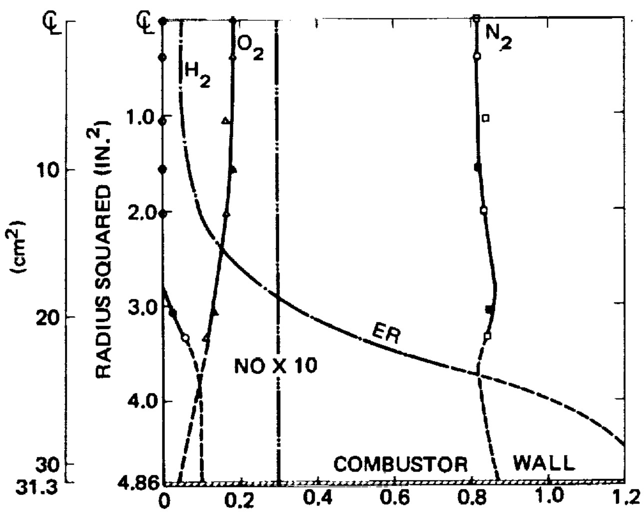

e) (C) RADIAL VARIATION OF SPECIE MOLE FRACTION AND DEDUCED ER IN COMBUSTOR EXIT PLANE. (U)

GAS SAMPLE DATA

RUN NO.	COMB.	INJ.	ER	η_c
98-27	D	d	0.79	0.65

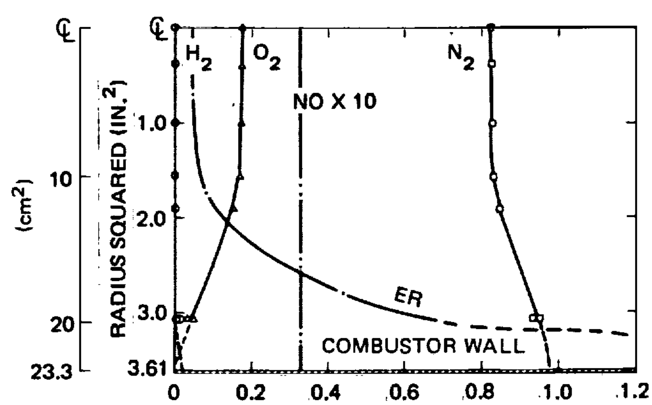

MOLE FRACTION, ER

f) (C) RADIAL VARIATION OF SPECIE MOLE FRACTION AND DEDUCED ER IN COMBUSTOR EXIT PLANE. (U)

(C) Fig. A-3 (cont'd)

GAS SAMPLE DATA

RUN NO.	COMB.	INJ.	ER	η_c
98-31	D	d	0.50	0.84

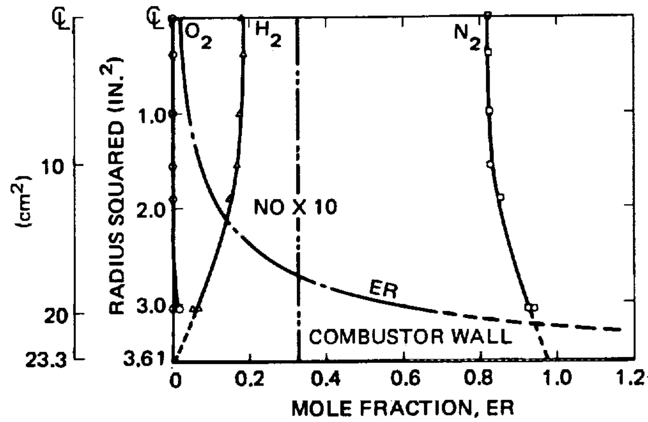

g) (C) RADIAL VARIATION OF SPECIE MOLE FRACTION AND DEDUCED ER IN COMBUSTOR EXIT PLANE. (U)

GAS SAMPLE DATA

RUN NO.	COMB.	INJ.	ER	η_c
100-17	C	d	0.84	0.64

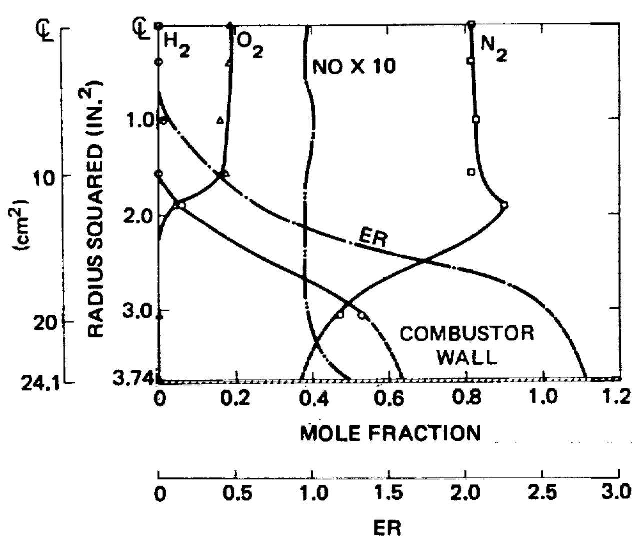

h) (C) RADIAL VARIATION OF SPECIE MOLE FRACTION AND DEDUCED ER IN COMBUSTOR EXIT PLANE. (U)

(C) Fig. A-3 (cont'd)

GAS SAMPLE DATA

RUN NO.	COMB.	INJ.	ER	η_c
100-21	C	d	0.53	0.71

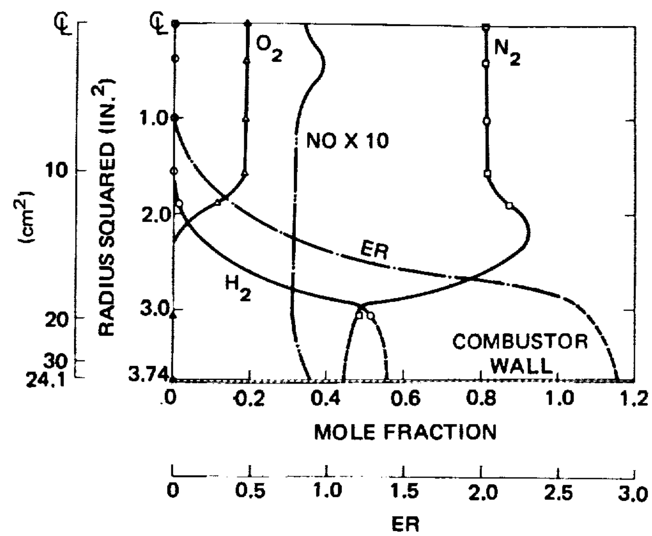

i) (C) RADIAL VARIATION OF SPECIE MOLE FRACTION AND DEDUCED ER IN COMBUSTOR EXIT PLANE. (U)

GAS SAMPLE DATA

RUN NO.	COMB.	INJ.	ER	η_c
102-17	C	d	0.83	0.55

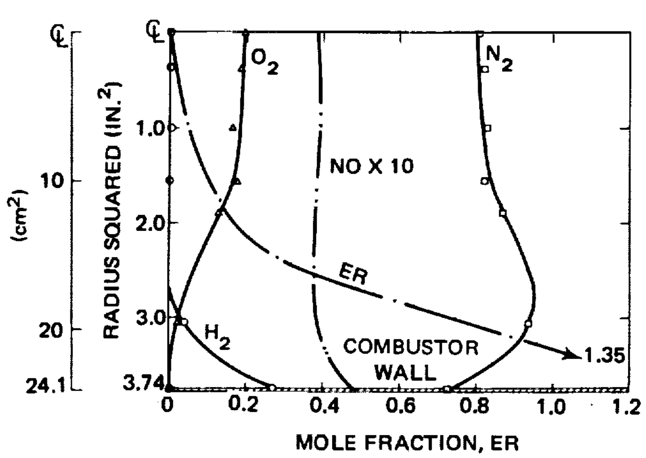

j) (C) RADIAL VARIATION OF SPECIE MOLE FRACTION AND DEDUCED ER IN COMBUSTOR EXIT PLANE. (U)

(C) Fig. A-3 (cont'd)

GAS SAMPLE DATA

RUN NO.	COMB.	INJ.	ER	η_c
102-21	C	d	0.52	0.72

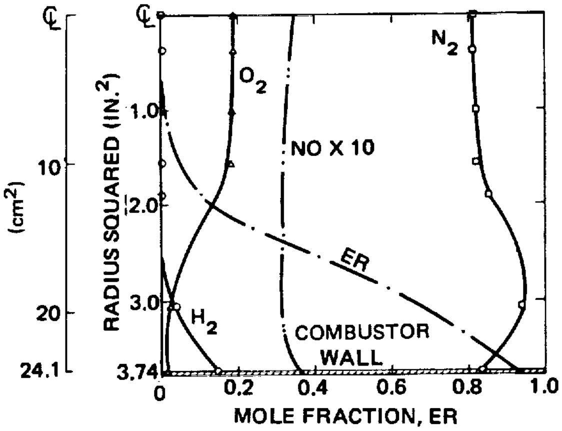

k)|(C) RADIAL VARIATION OF SPECIE MOLE FRACTION AND DEDUCED ER IN COMBUSTOR EXIT PLANE. (U)

GAS SAMPLE DATA

RUN NO.	COMB.	INJ.	ER	η_c
104-38	C	d	0.53	0.39

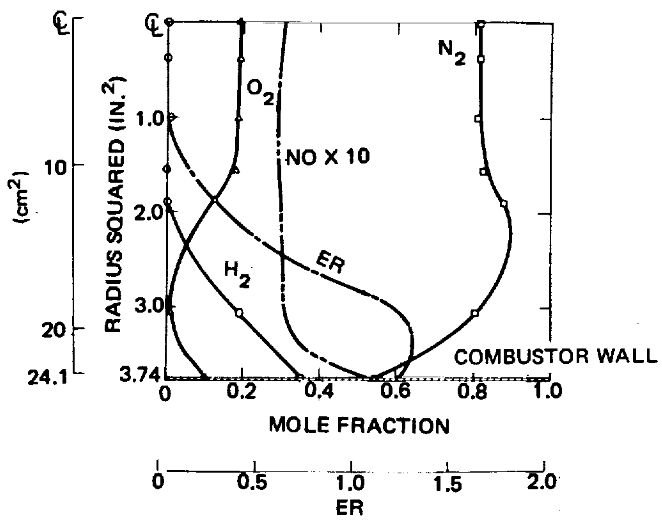

l)|(C) RADIAL VARIATION OF SPECIE MOLE FRACTION AND DEDUCED ER IN COMBUSTOR EXIT PLANE. (U)

(C) Fig. A-3 (cont'd)

GAS SAMPLE DATA

RUN NO.	COMB.	INJ.	ER	η_c
106-18	D	d	0.81	0.52

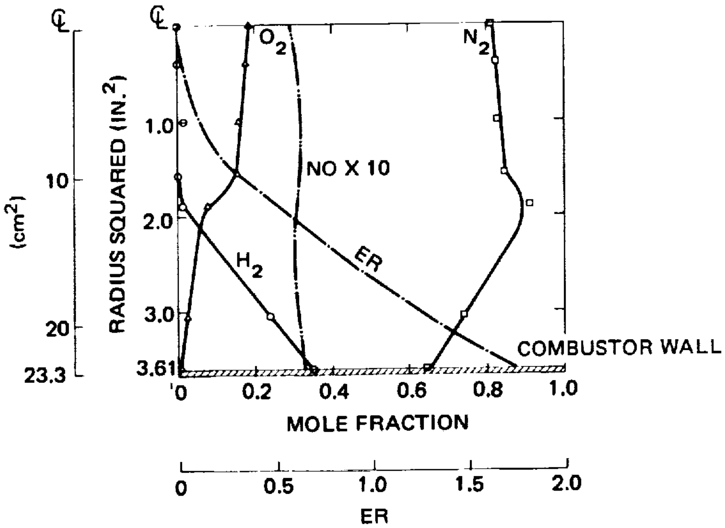

m) (C) RADIAL VARIATION OF SPECIE MOLE FRACTION AND DEDUCED ER IN COMBUSTOR EXIT PLANE. (U)

GAS SAMPLE DATA

RUN NO.	COMB.	INJ.	ER	η_c
108-29	D	a	0.80	0.72

OPEN SYMBOLS – ALIGNED WITH PORTS
SOLID SYMBOLS – BETWEEN PORTS

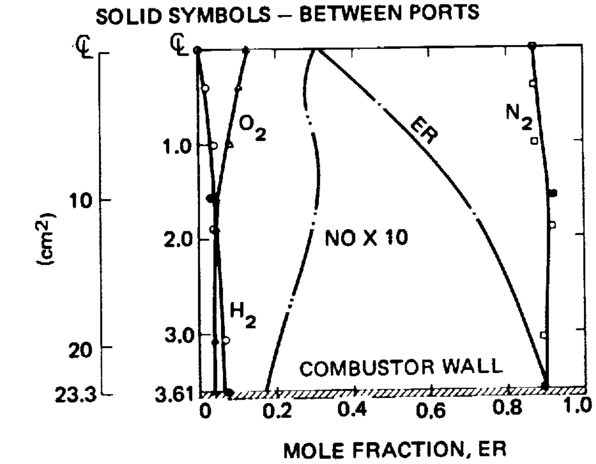

n) (C) RADIAL VARIATION OF SPECIE MOLE FRACTION AND DEDUCED ER IN COMBUSTOR EXIT PLANE. (U)

(C) Fig. A-3 (cont'd)

GAS SAMPLE DATA

RUN NO.	COMB.	INJ.	ER	η_c
110-28	D	a	0.83	0.74

OPEN SYMBOLS – ALIGNED WITH PORTS
SOLID SYMBOLS – BETWEEN PORTS

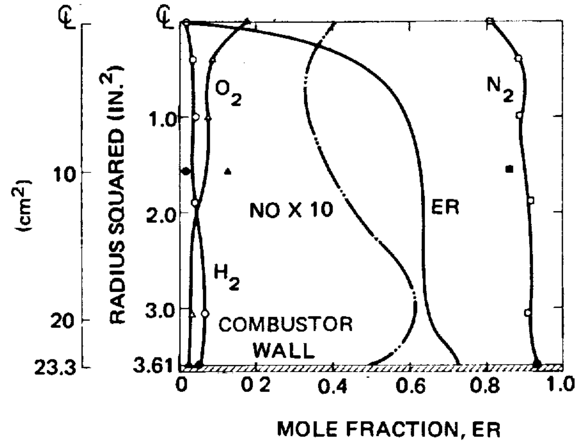

o) (C) RADIAL VARIATION OF SPECIE MOLE FRACTION AND DEDUCED ER IN COMBUSTOR EXIT PLANE. (U)

GAS SAMPLE DATA

RUN NO.	COMB.	INJ.	ER	η_c
110-33	D	a	0.52	0.84

OPEN SYMBOLS – ALIGNED WITH PORTS
SOLID SYMBOLS – BETWEEN PORTS

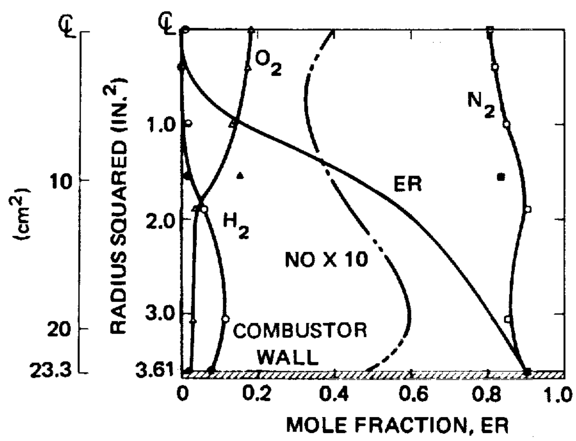

p) (C) RADIAL VARIATION OF SPECIE MOLE FRACTION AND DEDUCED ER IN COMBUSTOR EXIT PLANE. (U)
(C) Fig. A-3 (cont'd)

GAS SAMPLE DATA

RUN NO.	COMB.	INJ.	ER	η_c
112-26	E	d	0.79	0.61

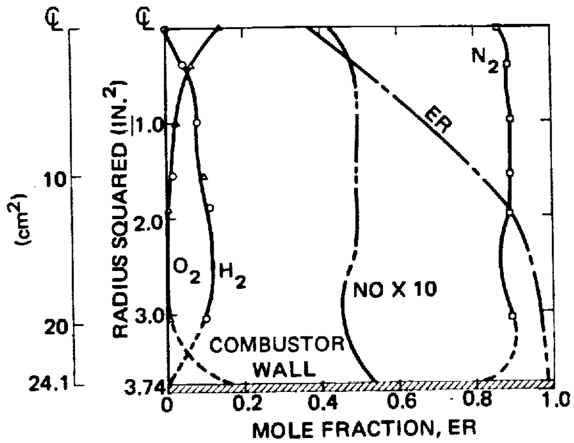

q) (C) RADIAL VARIATION OF SPECIE MOLE FRACTION AND DEDUCED ER IN COMBUSTOR EXIT PLANE. (U)

GAS SAMPLE DATA

RUN NO.	COMB.	INJ.	ER	η_c
112-31	E	d	0.50	0.75

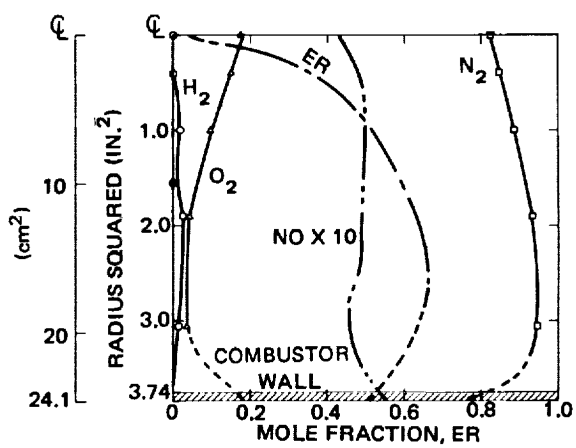

r) (C) RADIAL VARIATION OF SPECIE MOLE FRACTION AND DEDUCED ER IN COMBUSTOR EXIT PLANE. (U)

(C) Fig. A-3 (cont'd)

GAS SAMPLE DATA

RUN NO.	COMB.	INJ.	ER	η_c
114-15	E	a	0.78	0.85

OPEN SYMBOLS – ALIGNED WITH PORTS
SOLID SYMBOLS – BETWEEN PORTS

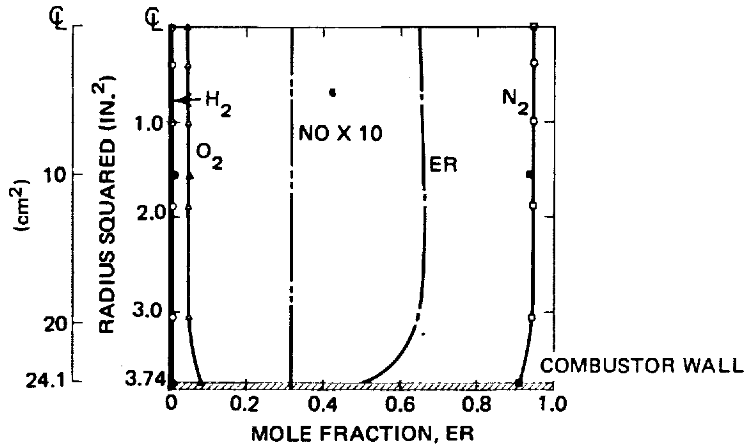

s) (C) RADIAL VARIATION OF SPECIE MOLE FRACTION AND DEDUCED ER IN COMBUSTOR EXIT PLANE. (U)

GAS SAMPLE DATA

RUN NO.	COMB.	INJ.	ER	η_c
114-20	E	a	0.50	0.94

OPEN SYMBOLS – ALIGNED WITH PORTS
SOLID SYMBOLS – BETWEEN PORTS

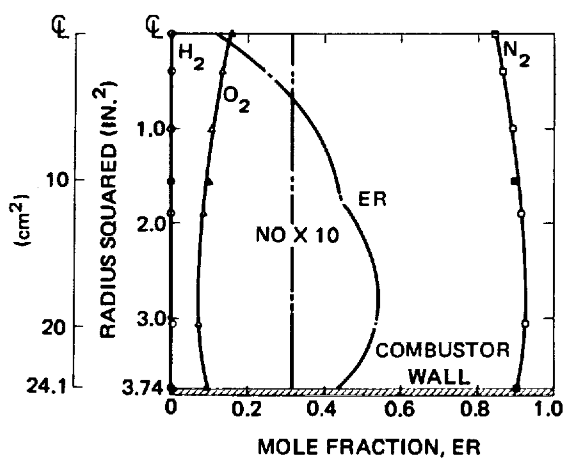

t) (C) RADIAL VARIATION OF SPECIE MOLE FRACTION AND DEDUCED ER IN COMBUSTOR EXIT PLANE. (U)

(C) Fig. A-3 (cont'd)

GAS SAMPLE DATA

RUN NO.	COMB.	INJ.	ER	η_c
116-16	F	a	0.78	0.81

OPEN SYMBOLS – ALIGNED WITH PORTS
SOLID SYMBOLS – BETWEEN PORTS

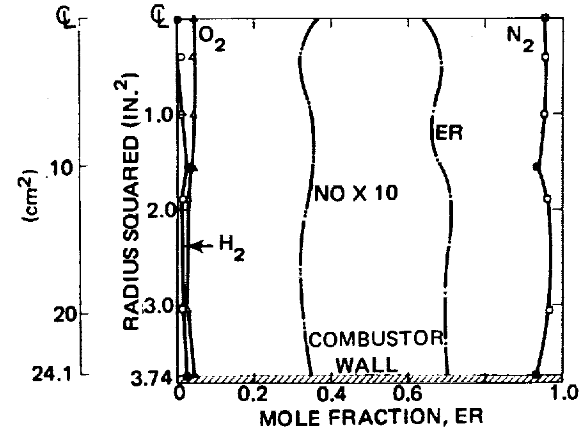

u) (C) RADIAL VARIATION OF SPECIE MOLE FRACTION AND DEDUCED ER IN COMBUSTOR EXIT PLANE. (U)

GAS SAMPLE DATA

RUN NO.	COMB.	INJ.	ER	η_c
116-21	F	a	0.49	0.92

OPEN SYMBOLS – ALIGNED WITH PORTS
SOLID SYMBOLS – BETWEEN PORTS

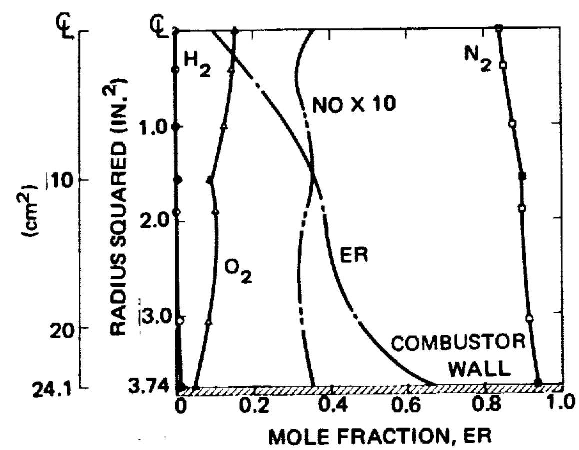

v) (C) RADIAL VARIATION OF SPECIE MOLE FRACTION AND DEDUCED ER IN COMBUSTOR EXIT PLANE. (U)

(C) Fig. A-3 (cont'd)

GAS SAMPLE DATA

RUN NO.	COMB.	INJ.	ER	η_c
119-58	F	b	0.80	0.70

OPEN SYMBOLS – BETWEEN PORTS
SOLID SYMBOLS – ALIGNED WITH PORTS

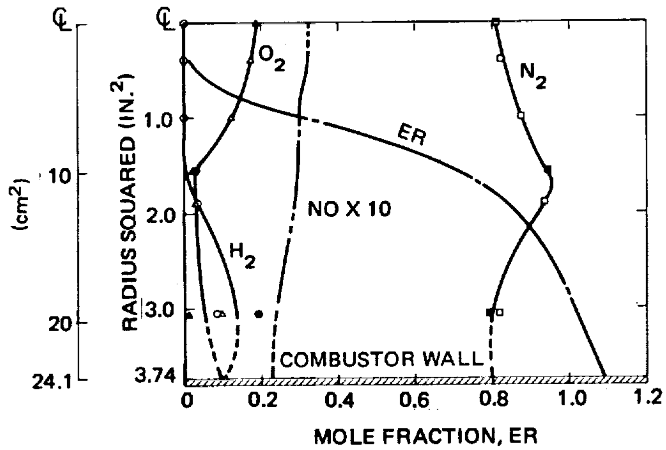

w) (C) RADIAL VARIATION OF SPECIE MOLE FRACTION AND DEDUCED ER IN COMBUSTOR EXIT PLANE. (U)

GAS SAMPLE DATA

RUN NO.	COMB.	INJ.	ER	η_c
119-62	F	b	0.51	0.89

OPEN SYMBOLS – BETWEEN PORTS
SOLID SYMBOLS – ALIGNED WITH PORTS

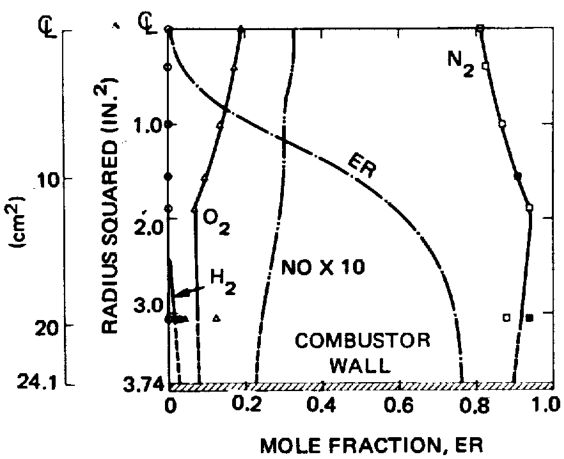

x) (C) RADIAL VARIATION OF SPECIE MOLE FRACTION AND DEDUCED ER IN COMBUSTOR EXIT PLANE. (U)

(C) Fig. A-3 (cont'd)

GAS SAMPLE DATA

RUN NO.	COMB.	INJ.	ER	η_c
121-55	G	b	0.93	0.68

OPEN SYMBOLS – BETWEEN PORTS

SOLID SYMBOLS – ALIGNED WITH PORTS

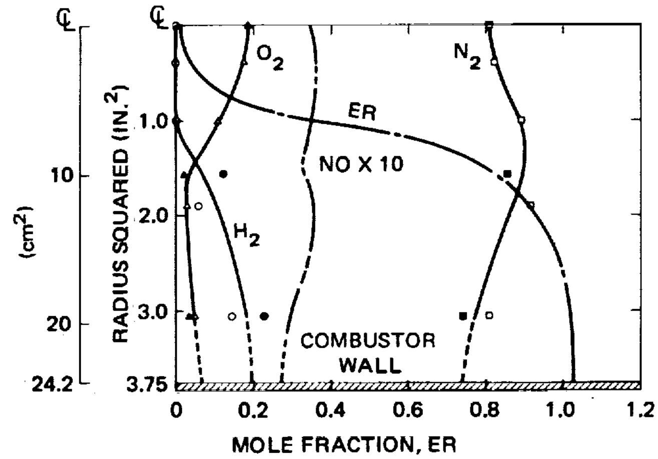

y) (C) RADIAL VARIATION OF SPECIE MOLE FRACTION AND DEDUCED ER IN COMBUSTOR EXIT PLANE. (U)

GAS SAMPLE DATA

RUN NO.	COMB.	INJ.	ER	η_c
121-58	G	b	0.76	0.77

OPEN SYMBOLS – BETWEEN PORTS

SOLID SYMBOLS – ALIGNED WITH PORTS

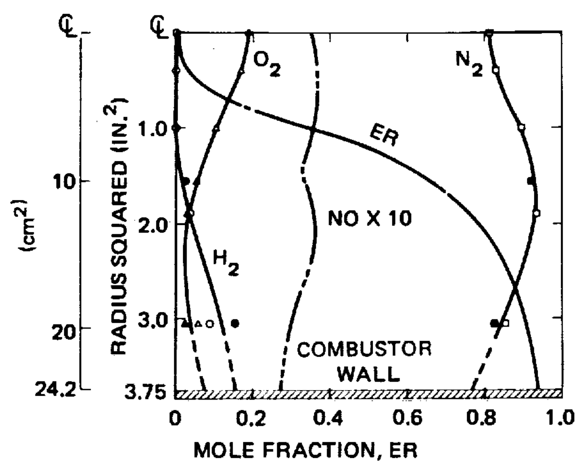

z) (C) RADIAL VARIATION OF SPECIE MOLE FRACTION AND DEDUCED ER IN COMBUSTOR EXIT PLANE. (U)

(C) Fig. A-3 (cont'd)

GAS SAMPLE DATA

RUN NO.	COMB.	INJ.	ER	η_c
123-3	H	b	0.70	0.70

OPEN SYMBOLS – BETWEEN PORTS
SOLID SYMBOLS – ALIGNED WITH PORTS

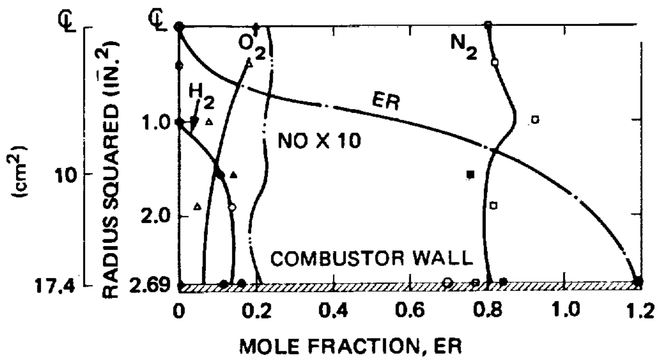

aa) (C) RADIAL VARIATION OF SPECIE MOLE FRACTION AND DEDUCED ER IN COMBUSTOR EXIT PLANE. (U)

GAS SAMPLE DATA

RUN NO.	COMB.	INJ.	ER	η_c
123-5	H	b	0.56	0.74

OPEN SYMBOLS – BETWEEN PORTS
SOLID SYMBOLS – ALIGNED WITH PORTS

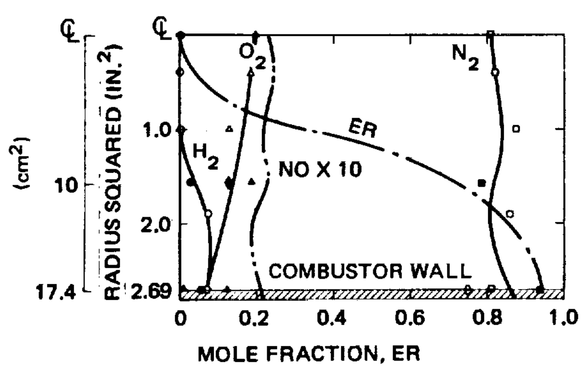

bb) (C) RADIAL VARIATION OF SPECIE MOLE FRACTION AND DEDUCED ER IN COMBUSTOR EXIT PLANE. (U)

(C) Fig. A-3 (cont'd)

GAS SAMPLE DATA

RUN NO.	COMB.	INJ.	ER	η_c
127-64	I	b	0.94	0.73

OPEN SYMBOLS – BETWEEN PORTS
SOLID SYMBOLS – ALIGNED WITH PORTS

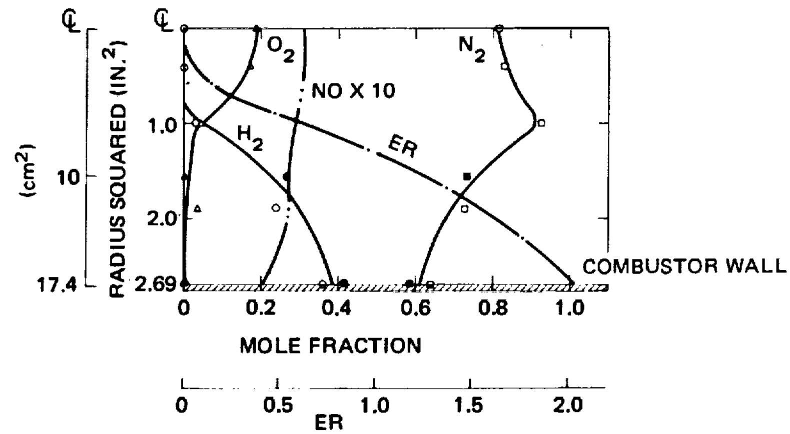

cc) (C) RADIAL VARIATION OF SPECIE MOLE FRACTION AND DEDUCED ER IN COMBUSTOR EXIT PLANE. (U)

GAS SAMPLE DATA

RUN NO.	COMB.	INJ.	ER	η_c
127-68	I	b	0.77	0.72

OPEN SYMBOLS – BETWEEN PORTS
SOLID SYMBOLS – ALIGNED WITH PORTS

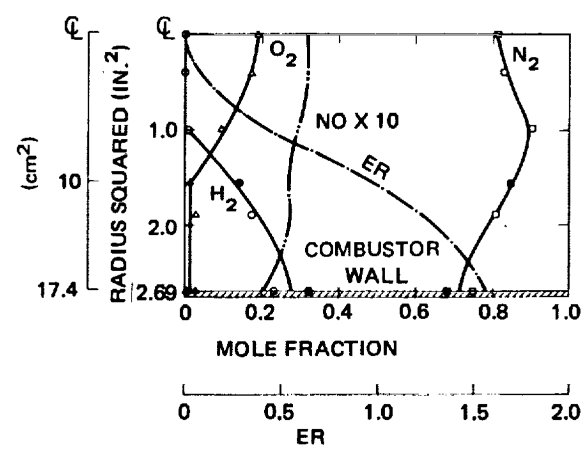

dd) (C) RADIAL VARIATION OF SPECIE MOLE FRACTION AND DEDUCED ER IN COMBUSTOR EXIT PLANE. (U)

(C) Fig. A-3 (cont'd)

GAS SAMPLE DATA

RUN NO.	COMB.	INJ.	ER	η_c
129- 121-334	I	b	0.81	0.65

OPEN SYMBOLS – BETWEEN PORTS
SOLID SYMBOLS – ALIGNED WITH PORTS

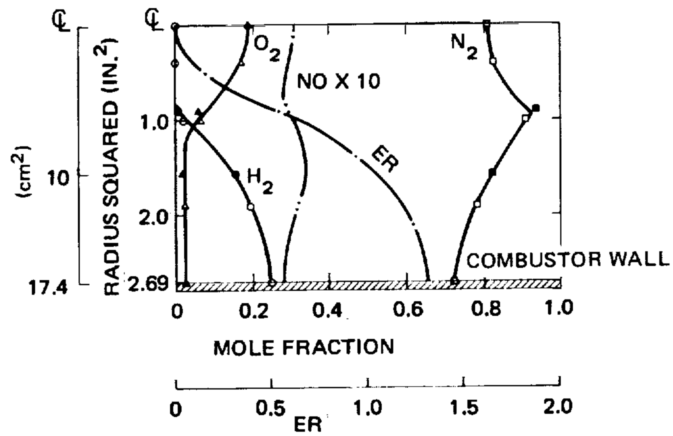

ee) (C) RADIAL VARIATION OF SPECIE MOLE FRACTION AND DEDUCED ER IN COMBUSTOR EXIT PLANE. (U)

GAS SAMPLE DATA

RUN NO.	COMB.	INJ.	ER	η_c
129- 350-593	I	b	0.64	0.67

OPEN SYMBOLS – BETWEEN PORTS
SOLID SYMBOLS – ALIGNED WITH PORTS

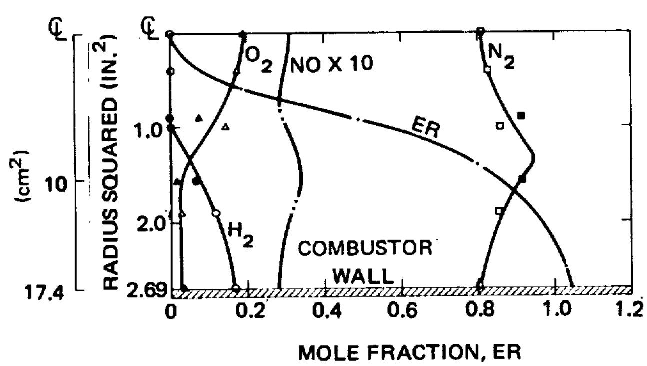

ff) (C) RADIAL VARIATION OF SPECIE MOLE FRACTION AND DEDUCED ER IN COMBUSTOR EXIT PLANE. (U)

(C) Fig. A-3 (concluded)